Neutron Veto Efficiency of the DarkSide-50 Detector

Hao Qian

A Dissertation
Presented to the Faculty
of Princeton University
in Candidacy for the Degree
of Doctor of Philosophy

Recommended for Acceptance
by the Department of
Physics
Adviser: Professor Cristiano Galbiati

September 2018

Abstract

DarkSide is a direct dark matter detection experiment searching for evidence of Weakly Interacting Massive Particles (WIMPs), a well-motivated candidate for dark matter. The DarkSide-50 Time Projection Chamber (TPC) has an active volume containing 50 kg of liquid argon and has been in operation at Laboratori Nazionali del Gran Sasso in Italy since late 2013. The DarkSide-50 TPC is surrounded by a 30 t boron-loaded liquid scintillator that acts as a Neutron Veto (NV). The NV is immersed in a 1 kt ultra-pure water Cherenkov detector that acts as a Muon Veto (MV) and passive shielding against external neutrons and γ-rays.

WIMP interactions are expected to be rare due to the low scattering cross section. A majority of the signals in our detector are from background particles. There are four primary sources of background: γ-rays and Cherenkov radiation from radioactive decays in the detector's construction materials, β's from ^{85}Kr and ^{39}Ar dissolved in the argon target, and neutrons from (α,n) and fission reactions from radioactive contaminants in the detector's materials.

The DarkSide-50 TPC is designed to efficiently reduce background from β's and γ-rays as well as from Cherenkov radiation by applying pulse shape discrimination and fiducial volume cuts. In this report, I will present detailed estimates of γ-ray activities of the detector components based on spectra and rates measured with the TPC and the NV.

The most important background in WIMP direct detection experiments are neutrons, which can produce elastic nuclear recoils that look exactly like WIMP interactions. In DarkSide-50, we both actively suppress and measure the rate of neutron-induced background events using the NV. The NV response was calibrated using two radioactive neutron sources, ^{241}Am^{13}C and ^{241}Am^{9}Be. I will present the neutron veto efficiency based on this calibration data.

Acknowledgements

First I want to thank my advisor, Prof. Cristiano Galbiati, for offering me this great opportunity to work on the DarkSide-50 experiment. I could not go this far without his consistent support and patience. He invited me to work at Laboratori Nazionali del Gran Sasso in Italy in the summer of 2012. I was impressed by the work they had done on the prototype experiment DarkSide-10. Cristiano encouraged me to work on the DarkSide-50 NV and to start collaborating with scientists from different institutes. Through the years, I gained a lot of knowledge and experience working on system operation, data acquisition, data processing, data analysis, and Monte Carlo simulation with the DarkSide-10 and DarkSide-50 experiments. This experience greatly enhanced my technical skills and scientific knowledge, and was very formative for my career development.

Next I am grateful to my co-advisor Prof. Peter Meyers for his insight into the data analysis. His guidance helped me a lot through my research. I would not have been able to write down this document without all he taught me. I appreciate his patience and encouragement as I progressed through this journey.

I also would like to thank Dr. Masayuki Wada. His dedication in walking me through the physics and analysis projects has greatly improved my knowledge and skills. I learned a lot from his lessons on C++, ROOT, and the DarkArt framework.

When I started graduate school at Princeton University, Dr. Shawn Westerdale (now at Carleton University) introduced me to the subject of the NV. He trained me to use advanced Monte Carlo techniques by implementing detectors geometries in the Geant4-based G4DS package. This experience greatly improved my knowledge and enabled me to carry out subsequent work independently. Shawn and I worked together on analyzing the neutron calibration simulation data. Shawn's seminal effort on studying the NV spectrum is a strong foundation for the study presented in this dissertation. In addition to our joint research, Shawn was also one of my roommates.

We enjoyed watching movies together. I also want to thank my other roommates over the last few years, Guangyong Koh, Katie Spaulding, and Nana Aboagye. The diversity of our apartment represented a great life experience for me.

Next, I would like to acknowledge the rest of people whose great efforts contributed to the DarkSide-50 Experiment. Specifically, I want to thank Xiang Xin, Chengliang Zhu, Chris Standford, and XinRan Li of the Princeton DarkSide group. Besides, my special thanks go to Dr. JingKe Xu (now at Lawrence Livermore National Laboratory) and Dr. Charles HuaJie Cao (now at Goldman Sachs) both for their help in my research and for the many life experiences we shared during my first years in Princeton. I also appreciate our group assistant Helen Ju for her help in arranging trips, events, and even my visa applications: research life was simple thanks to her tireless efforts in organizing the group.

I also want to thank my friends JunFeng Li and LianKun Zhou. We carried our friendship a long way from college in China to different places in Canada and America. JunFeng drove me to Niagara Falls and Chinatown in Canada. We enjoyed the gorgeous views in Toronto. LianKun Zhou hosted my visit to Los Angeles. We visited the Santa Monica Beach, Universal Studio and Hollywood. We shared our thoughts and happiness. I appreciate the special moments we had.

Last, but not least, I would like to thank my parents for their unconditional love and support all the time. I am so sorry for not spending enough time with you during these years. I am grateful to my sister and brother in law for taking care of the family during my absence. My love also goes to cousin, the new baby in our family. I feel sorry for the absence of the memorial service of my dear grandfather and aunt. I miss you so much.

To my family.

Contents

List of Tables

List of Figures

Chapter 1

Introduction

According to recent astronomical observations, most of the energy budget of the Universe is unknown: $\sim$27 % is dark matter and $\sim$69 % are inferred from its gravitational effects such as the motions of visible matter, gravitational lensing, its influence on the universe's large-scale structure, and its effects on the Cosmic Microwave Background (CMB). The dark matter hypothesis plays a central role in current modeling of cosmic structure formation, galaxy formation and evolution, and explanations of the anisotropies observed in the CMB. All these pieces of evidence suggest that galaxies, clusters of galaxies, and the universe as a whole contain far more matter than that observable via the electromagnetic spectrum.

Theoretical physicists have proposed several models and candidates for dark matter. One popular dark matter candidate is the weakly interacting massive particles [1]. Due to the extremely low interaction cross sections, dark matter experiments require high sensitivity and very low background. In order to detect dark matter, experiments must reduce background while maintaining sensitivity to a potential dark matter signal. This dissertation will focus on the study of the backgrounds of DarkSide-50 and of the rejection efficiency of the NV.

1.1 Evidence for Dark Matter

1.1.1 Galaxy Rotation Curves

In 1993, Swiss astrophysicist Fritz Zwicky applied the virial theorem to the Coma galaxy cluster and obtained evidence of unseen mass that he called "dunkle materie". The mass of the cluster was estimated to be 400 times heavier than the visually observable mass. Based on these observations, Zwicky suggested that some invisible matter may provide the gravitational force required to hold the cluster together. Although his estimate of dark matter density was off by more than an order of magnitude, his discovery was the first formal inference of the existence of dark matter [2].

The first robust indication of the existence of dark matter came from the measurement of the galaxy rotation curves, which describe the rotational velocity of the stars in a galaxy as a function of the object's distance from the center. Near the center of the galaxy, the rotation curve should rapidly increase due to the high matter density. Further from the center, the rotation curve is expected to drop off as $1/\sqrt{R}$ near the edge of the galaxy [3]. This expectation does not match observations as shown for the galaxy NGC 2974 in Figure 1.1: the data agree with the prediction based on the gravitational contribution of stars and gas up to a radius of 12 kpc; at larger radii, there is a large discrepancy, which can be explained by the existence of non-luminous matter throughout the galaxy in form of a dark matter halo [4].

1.1.2 Galaxy Clusters and Gravitational Lensing

In the general theory of relativity, massive objects warp the local space-time structure, meaning the path of light can be significantly deflected in strong gravitational fields. This is the gravitational lensing effect, which can measure cluster masses without relying on observations of dynamics. There are two types of lensing: strong lensing produces multiple images or giant arcs near the cluster core, while weak lens-

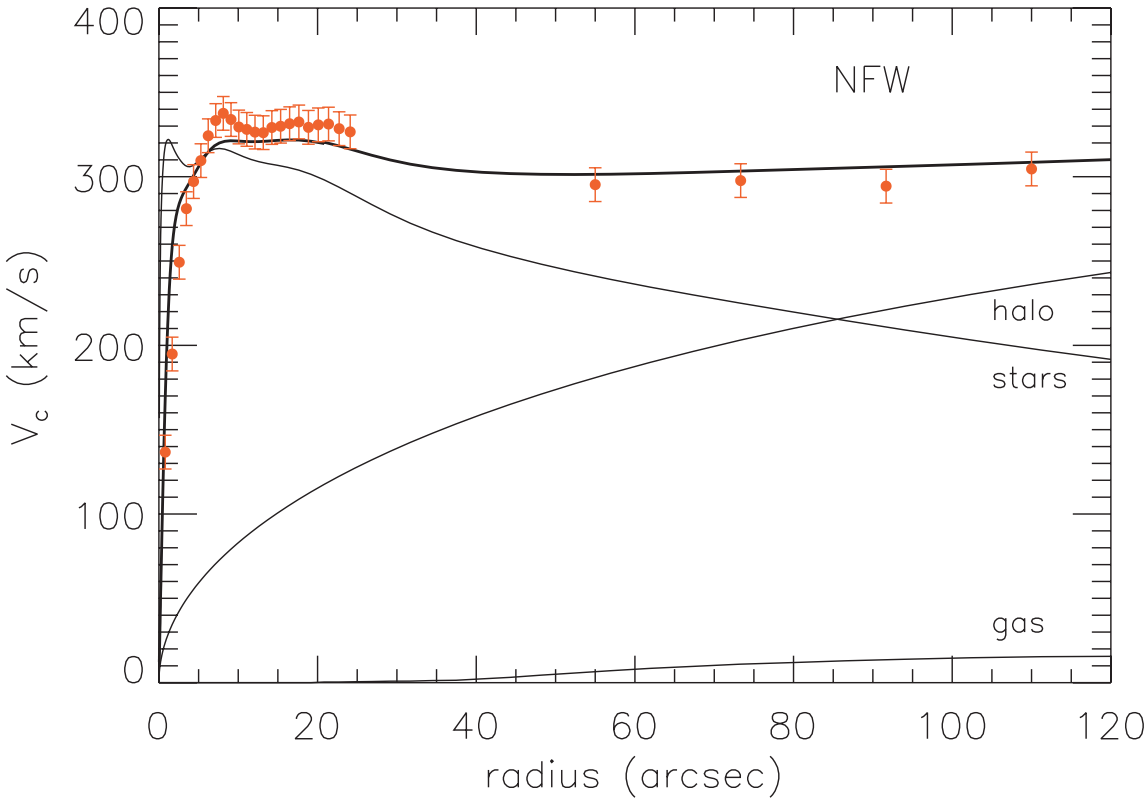

Figure 1.1: Observed rotational velocities of stars (red dots) in the galaxy NGC 2974 compared with prediction (black curves) accounting for gravitational contributions from stars, gas, and dark matter halo (Figure from Ref. [4]).

ing is observed as small shape distortions around the outer regions. By measuring the geometry of the distortion, one can reconstruct the mass of the intervening non-luminous matter [5].

Additional observation evidence for dark matter comes from the Bullet Cluster as shown in Figure 1.2. The image is a composite of optical data, X-ray data and a reconstructed mass map of two galaxy clusters that have recently collided. The X-ray emission from the intergalactic gas within each cluster is shown in red. It is concentrated near the point of impact due to the electromagnetic interactions that slowed down the gas. The mass density, reconstructed using lensing, is shown in blue and appears alongside the galaxies not within the intra-cluster matter, suggesting the existence of non-luminous matter with a very low self-interaction cross section.

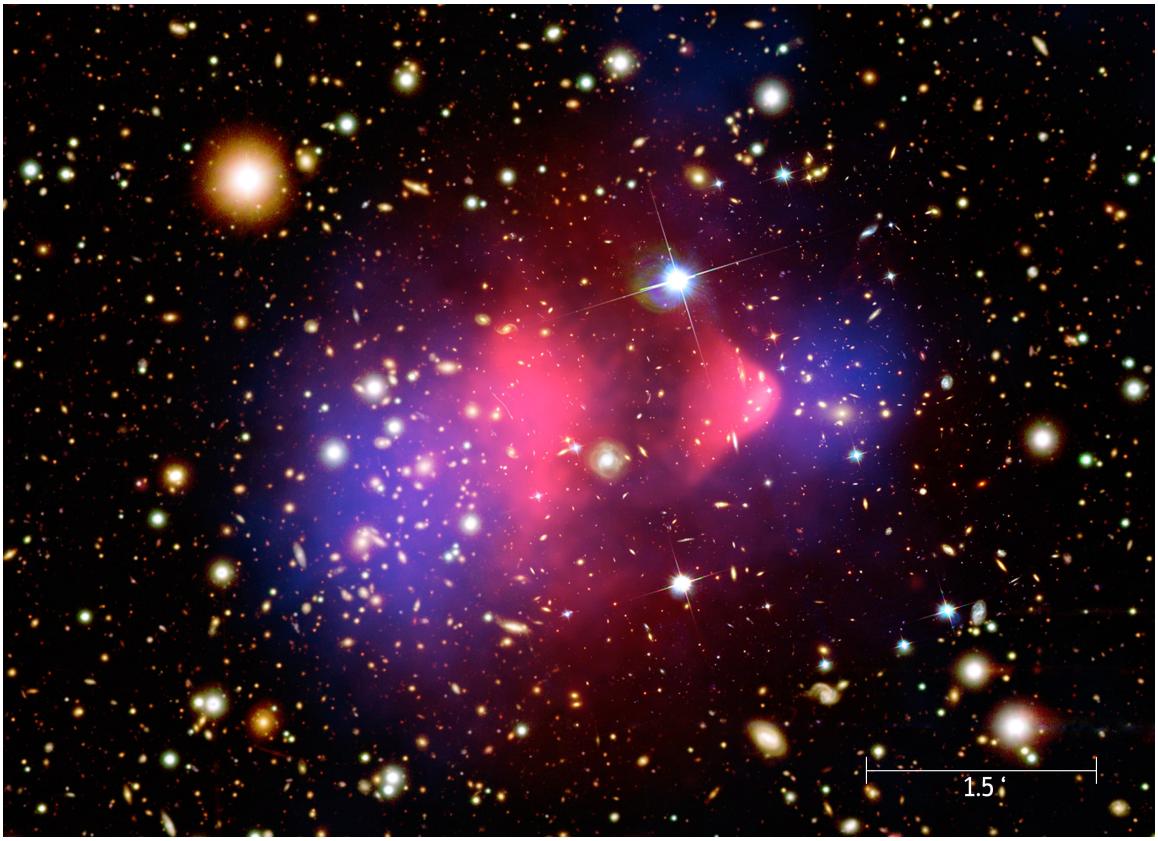

Figure 1.2: Optical, X-rays, and gravitational lensing images of cluster 1E 0657-558, the "Bullet Cluster". In red is shown the X-ray image; in blue the gravitational lensing image; and in bright colors the optical image (Figure from Ref. [6]). See for discussion and interpretation.

1.1.3 Cosmic Microwave Background

The Cosmic Microwave Background is thermal radiation leftover from the separation of matter and radiation following the Big Bang. In 1964, a mysterious microwave background was found when Arno Penzias and Robert Wilson, scientists from Bell Lab, studied the noise in a radio-wave antenna receiver [7]. This background persisted day and night and was isotropic in the sky. Penzias and Wilson determined the background was not from human activities, such as radio broadcasting or radar, nor the Earth, the sun or the Milky Way. Later on, it was attributed to be the thermal radiation of the big bang, usually referred as the CMB. The two scientists, along with Pyotr Leonidovich Kapitsa, were awarded The Nobel Prize in Physics in 1978 for the

discovery of the CMB. This work is also recognized as one of the greatest scientific discoveries in the twentieth century [8].

The CMB is well explained as radiation leftover from an early stage in the development of the universe, and its discovery is considered a landmark test of the Big Bang model of the universe. When the universe was young, before the formation of stars and planets, it was in an extremely hot and dense state as it was confined in a small region. As the universe expanded, the temperature and energies of the particles decreased. When the temperature of the universe dropped to the magnitude of 1 eV to 10 eV, protons and electrons combined to form neutral hydrogen atoms. These atoms could no longer absorb the thermal radiation, and so the universe became transparent. This period is referred to as the recombination epoch. This led to the decoupling of photon from matter, as photons started to travel freely through space rather than constantly being scattered by electrons and protons in plasma. The photons grew fainter and less energetic, since the expansion of space caused their wavelength to increase over time. This is the origin of the CMB, which we observe nowadays as the background radiation in the microwave region with a temperature equivalent to $\sim$2.7 K [9]. Figure. 1.3 shows the temperature map of CMB as determined by the Planck mission [9].

As the energy density of the Universe continued to decreased, other forms of matter came progressively out of thermal equilibrium with the rest of the universe.

Although the CMB is mostly isotropic, there are small anisotropies in its distribution, originating from the temperature fluctuations in the early universe that were in turn caused by under- and over-densities. An over-dense region can grow by attracting more mass, but pressure from photons tends to resist the infall as the radiation increases. Therefore, the anisotropy of CMB provides a direct view of the early Universe at the time of decoupling and today many cosmological parameters,

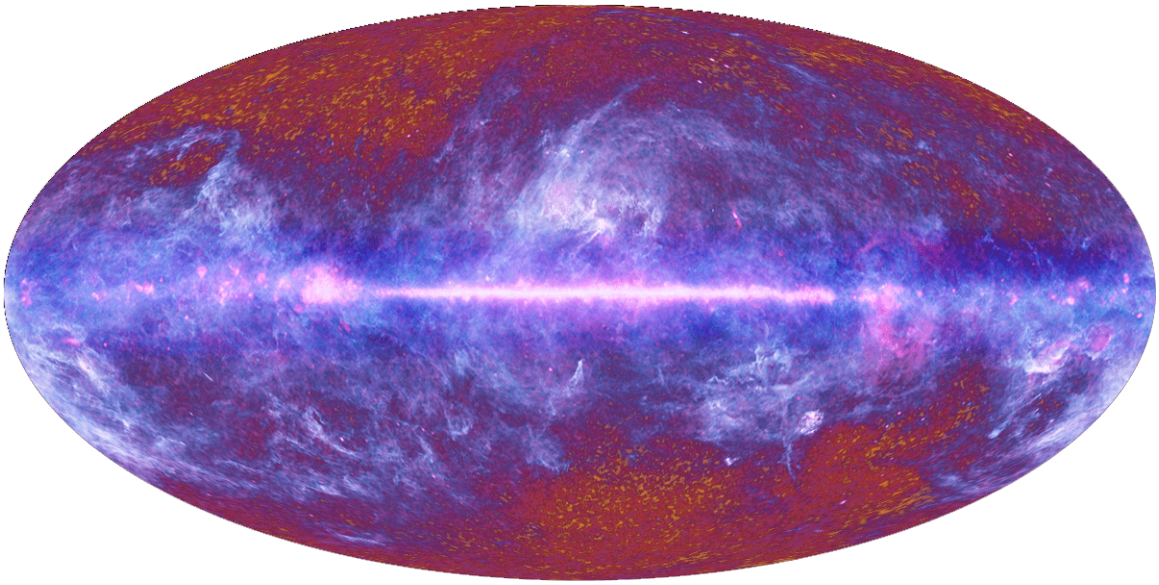

Figure 1.3: Temperature map of the CMB as measured by the Planck mission (Figure from Ref. [9]. The bright horizontal strip across the center is due the distortions from the Doppler shift caused by Earth's motion.

including the universe expansion rate and the baryonic and matter densities, can be reconstructed from the measurement of the CMB anisotropy.

The variations in temperature shown in Figure 1.3 is be characterized by the angular power spectrum of the CMB. This spectrum contains information about the formation of the Universe and its content. The amplitude of the angular power spectrum as a function of the multipole momenta l offers the best quantitative representation of the anisotropies in the CMB [10]. Recent measurements of the CMB power spectrum from the WMAP group are shown in Figure 1.4.

The angular power spectrum of CMB can be used to estimate many cosmological parameters. Specifically, it allows us to determine the fraction of baryonic matter in the universe. Some of the fit results of the ΛCDM cosmological model to the WMAP data are listed in Table 1.1. Based on the 9-year results from WMAP, the baryonic matter is estimated to be only $\sim$5 % of the total mass of the universe while cold dark matter accounts for $\sim$27 % [10]. The rest is dominated by dark energy, which is still not well understood. Recent from the Planck mission and other experiments are con-

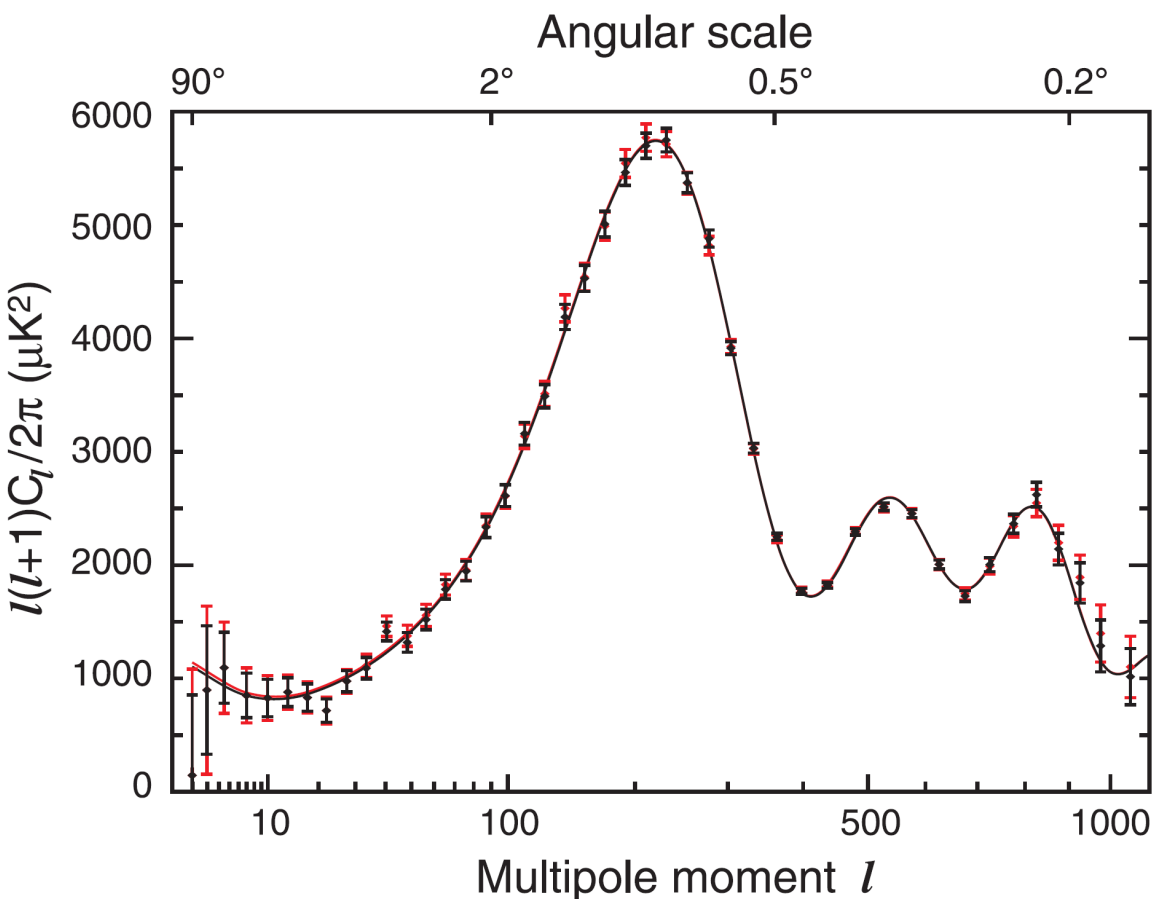

Figure 1.4: Angular power spectrum of CMB from the WMAP data (Figure from Ref. [11]).

sistent with the WMAP measurements. The consistency between CMB measurement campaigns is one of the most compelling piece of evidence for the existence of dark matter in the Universe.

Table 1.1: A list of parameter values of the ΛCDM cosmological model fit to the WMAP nine-year data [11].

Parameter	**Symbol**	**Value**	**Unit**
Baryon density	Ω_b	0.0463 ± 0.0024	-
Cold dark matter density	Ω_c	0.233 ± 0.023	-
Dark energy density	Ω_Λ	0.721 ± 0.025	-
Hubble constant	H_0	70.0 ± 2.2	$\mathrm{km\,s^{-1}\,Mpc^{-1}}$
Age of the universe	t_0	13.74 ± 0.11	Gyr

1.2 Dark Matter Candidates

The existence of dark matter plays a central role in current models of cosmic structure formation, galaxy formation, and evolution, even though the composition of dark matter remains unknown. There are several potential dark matter candidates with different energy ranges and modes of interaction with the Standard Model, which provide methods to detect dark matter particles experimentally.

Possible dark matter candidates include dense baryonic matter and non-baryonic matter. The main baryonic candidate is the Massive Compact Halo Objects (Machos), which include brown dwarf stars, jupyters, and black holes. Candidates for nonbaryonic dark matter are hypothetical particles such as axions or supersymmetric particles [12].

Dark matter can be classified as cold, warm or hot based on its velocity. In particular, Cold Dark Matter (CDM) particles are more easily trapped in the gravitational potentials, and, as a result, they form more well-defined large scale structures. Warm dark matter candidates, such as right-handed or sterile neutrinos, reduce the formation of too many small galaxies, which is the missing satellite problem in cold dark matter theory [13]. Hot dark matter does not seem to be capable of supporting galaxy or galaxy cluster formation [14]. In this dissertation, I will discuss some of the most promising dark matter candidates.

1.2.1 Axions

The axion is a hypothetical elementary particle postulated by Peccei and Quinn in 1977 to resolve the strong CP problem in Quantum ChromoDynamics (QCD). According to QCD, there could be a violation of CP-symmetry in the strong interactions [15]. In theory, a generic CP violation in the strongly interacting sector would give the neutron an electric dipole moment on the order of 10^{18} while the experimen-

tal upper bound is roughly one trillionth that size. This problem can be explained by an effective Standard Model Lagrangian describing QCD interactions [16]:

$$\mathcal{L}_{QCD} = -\frac{1}{4}G^a_{\mu\nu}G^{a\mu\nu} + \sum_r \bar{q}^a_r(i\not{D}^b_a - m_r\delta^b_a)q_{rb} + \frac{\bar{\theta}}{32\pi^2}G^a_{\mu\nu}\tilde{G}^{a\mu\nu}, \tag{1.1}$$

where $G^a_{\mu\nu}$ is the gluon gauge tensor field, q^a_r is a quark of charge r, flavor a, mass m_r, and $\not{D}$ is the gauge-invariant differential operator.

The first term in Equation. 1.1 describes the interactions between gluons, while the second term represents the interactions of quarks with gluons. Both terms conserve CP flavor, which has been confirmed in highly precise particle physics experiments [17]. Although the third term obeys the symmetries expected from QCD, it indicates CP violation in QCD interactions. So far, the terms related with electromagnetic and weak interactions have been observed in nature, no experiment has confirmed any CP violation in the strong interaction.

Peccei and Quinn came up with a P-Q symmetry that is spontaneously broken and leads to CP conservation. The axion is the pseudo Goldstone boson associated with this symmetry [17].

The interactions of an axion field with others can be described as:

$$\mathcal{L}_{axion} = -\frac{1}{4}(g_{a\gamma\gamma}aF_{\mu\nu}\tilde{F}^{\mu\nu} + g_{agg}aG^i_{\mu\nu}\tilde{G}^{i\mu\nu}), \tag{1.2}$$

where $F_{\mu\nu}$ is the electromagnetic field strength tensor, $g_{a\gamma\gamma}$ is the coupling of the axion to a pair of photons, and g_{agg} is the axion coupling to a pair of gluons. Equation 1.2 allows three primary axion-photon interactions: axion decay ($a \to 2\gamma$), photon-to-axion coalescence ($2\gamma \to a$), and Primakoff conversion ($a \leftrightarrow \gamma$) [18]. Since it is possible for the axion to couple with photons in a strong electromagnetic field, axion becomes a potential dark matter candidate.

The mass of the axion (m_a) is predicted to depend on a single parameter f:

$$m_a \sim \frac{10^6\,\mathrm{GeV}}{f}\mathrm{eV}, \tag{1.3}$$

The value of f, as well as the mass of the axion, is mainly constrained by cosmological parameters. The observed white-dwarf density of the galaxy and limits on its cooling time set the limit: $f > 10^9\,\mathrm{GeV}$, which gives an upper limit for the mass of the axion as $m_a < 3 \times 10^{-2}\,\mathrm{eV}$. A lower bound on the axion mass comes from cosmological density, $\Omega_a \sim \mathrm{f}/10^{12}\,\mathrm{GeV}$. The requirement that $\Omega_a < 1$ then gives: $m_a > 10^{-5}\,\mathrm{eV}$. As as result, the mass of the axion is on the μeV-meV scale [19].

1.2.2 Sterile Neutrino

There are three known flavors of neutrino in Standard Model: electron neutrino (ν_e), muon neutrino (ν_μ) and tau neutrino (ν_τ). Neutrino does not carry any charge, thus it is not affected by the electromagnetic force. Neutrino interacts via the weak force and is therefore difficult to detect. Although neutrino is predicted to be massless in the Standard Model, measurements of the neutrino oscillation demonstrate that neutrino has a very light mass, with an upper limit of 0.5 eV. Experimental results show that all produced and observed neutrinos have left-handed helicities (spins antiparallel to momenta), while all antineutrinos have right-handed helicities. A sterile neutrino could be either a fourth flavor of neutrino that does not couple with any other known leptons, or a right-handed neutrino [15].

The existence of the right-handed neutrino can potentially lead to the Dirac-type neutrino mass term. Besides this mechanism, it is possible to have Majorana mass term since the neutrino does not carry charge [13]. The right-handed neutrino is not influenced by the strong, electromagnetic, or weak interactions, which indicates its existence in the early epoch of the Universe. When the right-handed neutrino

decouples at relatively high temperature (T), their number density as a function of T^3 is ten times smaller than that of the standard neutrino. Therefore, the mass of the right-handed neutrino is on the order of $900h^2$ eV, which is in the range of warm dark matter candidate [20]. Here $h = H_0/(100\,\mathrm{km\,s^{-1}\,Mpc^{-1}})$ where H_0 is the Hubble constant.

1.2.3 Weakly Interacting Massive Particles

Weakly Interacting Massive Particles (WIMPs) arise from the idea that obtaining the correct abundance of dark matter today via thermal production requires a self-annihilation cross section of $< \sigma_A \nu > \simeq 3 \times 10^{-26}\,\mathrm{cm^3\,s^{-1}}$ [21], which is expected for a new particle at the level of GeV to TeV mass range that interacts via the electroweak force. Supersymmetry, an extension to the Standard Model, also predicts a new particle with these properties [21].

Supersymmetry was introduced to solve a number of independent problems in particle physics, for instance the hierarchy problem, the fine tuning problem and unification of the fundamental forces [22]. It proposed a type of spacetime symmetry that relates two basic classes of elementary particles: bosons, which have an integer-valued spin, and fermions, which have a half-integer spin. Each particle from one group is associated with a particle from the other, known as its superpartner, the spin of which differs by a half-integer. Besides this, supersymmetry adds an additional discrete symmetry, R-parity, to the Standard Model. The interactions among particles conserve this value. Due to energy conservation, particles can only decay into other particles with equal or smaller mass. Therefore the Lightest Supersymmetric Particle (LSP) predicted by supersymmetry must be stable. Since LSP only interacts with the Standard Model particles via gravitational and weak interactions, it is a WIMP as a potential candidate for dark matter [23].

The time evolution of the number density (n_χ) of WIMPs (denoted χ), can be characterized as:

$$\frac{dn_\chi}{dt} + 3Hn_\chi = - < \sigma_A \nu > [(n_\chi)^2 - (n_\chi^{\mathrm{eq}})^2], \tag{1.4}$$

where $H{=}\dot{a}/a$ is the Hubble expansion rate, a is the scale factor of the Universe, and the dot denotes derivative with respect to time. n_χ^{eq} is the number density of WIMPs at equilibrium state. The second term on the left side represents the expansion of the universe. The first term in the brackets on the right side accounts for the depletion of WIMPs due to annihilation, and the second term arises from the creation of WIMPs from the inverse reaction [24].

Equation 1.4 can be approximately solved based on the assumptions of entropy conservation across the evolution of the Universe. At early Universe ($T \gg m_\chi$, where m_χ is the mass of χ), $H \propto T^2$, while $n_\chi \propto T^3$, so the number density of χ's drops more drastically than the expansion rate. Therefore, $3Hn_\chi$ from Equation. 1.4 is negligible and the number density tracks its equilibrium abundance. At that time, χ's are rapidly converting to lighter particles and vice versa. While at late times (T $\ll m_\chi$), the expansion rate dominates and the term on the right size of Equation 1.4 becomes negligible, which indicates that the abundance of χ's remains unchanged [24].

The current dark matter density (Ω_χ) can be calculated using the present entropy density ($\sim$4000 cm^{-3}) and the critical density today ($\rho_{\mathrm{crit}}{\sim}10^{-5}h^2$ GeV cm^{-3}, where $h = H_0/(100\,\mathrm{km\,s^{-1}\,Mpc^{-1}})$ [25]. The relation is denoted as:

$$\Omega_\chi h^2 = \frac{m_\chi n_\chi}{\rho_{\mathrm{crit}}} \simeq 3 \times 10^{-27}\,\mathrm{cm^3\,s^{-1}} / < \sigma_A \nu > . \tag{1.5}$$

The result is independent of the mass of the WIMP and is inversely proportional to its annihilation cross section. Figure. 1.5 shows the annihilation cross section $< \sigma_A \nu >$ to produce the present dark matter density is estimated to be $2.2 \times 10^{-26}\,\mathrm{cm^3\,s^{-1}}$

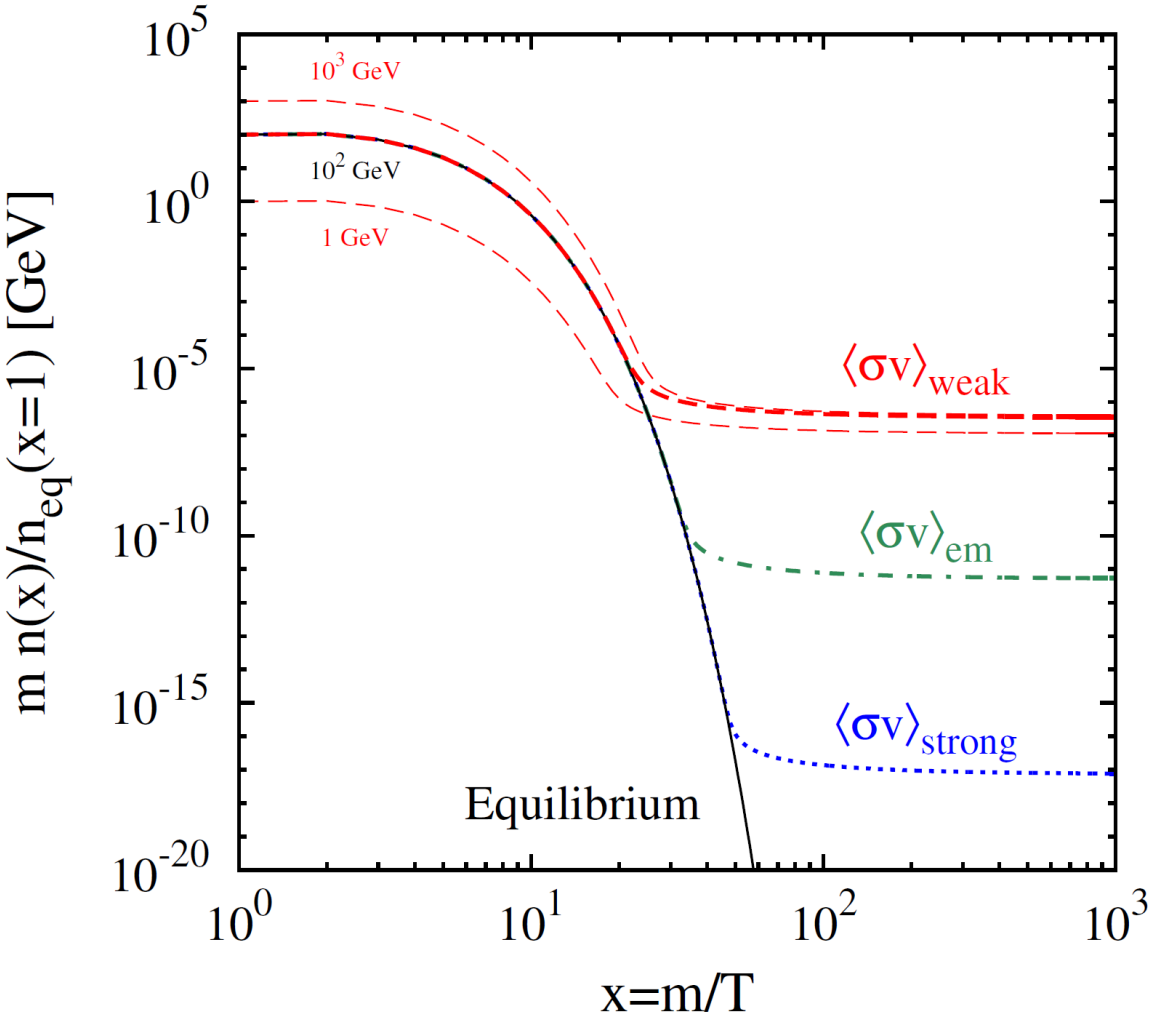

Figure 1.5: Cosmological WIMP abundance as a function of $x = m/T$. The evolution of the equilibrium abundance (solid black) is calculated based on the WIMP mass (m) of 100 GeV c^{-2}. With that WIMP mass, the WIMP annihilation cross section $< \sigma\nu >$ here includes weak interaction (dashed red), electromagnetic interaction (dot-dashed green), and strong interaction (dotted blue). For the weak interaction, the WIMP mass dependence for m =10^3 GeV c^{-2} (upper dashed red) and m =10^3 GeV c^{-2} (lower dashed red) are plotted here (Figure from Ref. [24]).

for WIMP mass from 10 GeV c^{-2} up to 10 TeV c^{-2}, and the value is approximately 5×10^{-26} cm^3 s^{-1} for WIMP mass below 1 GeV c^{-2}. The QCD transition in the Universe when the temperature was at the QCD scale (0.1-1 GeV c^{-2}) results in the drop between 1 GeV c^{-2} and 10 GeV c^{-2} WIMP mass [26].

1.3 WIMP Dark Matter Detection

So far, I have gone through some of the potential dark matter candidates. WIMPs are particularly well motivated due to the WIMP miracle. Since WIMPs have a low interaction cross section, they are extremely difficult to detect. However, WIMPs are predicted to have a non-zero coupling to baryons and could be detected with existing or developing technologies. There are many experiments underway to detect WIMPs both directly and indirectly.

1.3.1 WIMP Event Rate

Dark matter particles may interact with the atoms of the target in the detectors. The characteristics of WIMP interaction can be represented by the WIMP-nucleus differential cross section, which is derived from the Lagrangian that describes the interaction of WIMP with the Standard Model. The differential rate for the scattering can be expressed as:

$$\frac{dR}{dE_R} = N_T \frac{\rho_{\rm dm}}{m_\chi} \int_{\nu_{min}}^{\infty} d\vec{\nu} f(\vec{\nu}) \nu \frac{d\sigma}{dE_R}, \tag{1.6}$$

where N_T is the number of target nuclei, $\rho_{\rm dm}$ is the local dark matter density in the galactic halo, m_χ is the WIMP mass, $\vec{\nu}$ and $f(\vec{\nu})$ are the WIMP velocity and velocity distribution function in the Earth frame and $d\sigma/dE_R$ is the WIMP-nucleus differential cross section. The nuclear recoil energy (E_R) is equal to $\mu_N^2 \nu^2 (1-cos\theta)/m_N$, where θ is the scattering angle in the center-of-mass frame, m_N is the mass of target nucleus and μ_N is the WIMP-nucleus reduced mass. The minimum velocity ν_{min} is $\sqrt{m_N E_{\rm th}/2\mu_N^2}$, where $E_{\rm th}$ is the energy threshold of the detector [1].

The integral of the differential event rate over all possible recoil energies gives the total event rate with a unit of per kilogram per day is:

$$R = \int_{E_{th}}^{\infty} dE_R N_T \frac{\rho_{\rm dm}}{m_\chi} \int_{\nu_{min}}^{\infty} d\vec{\nu} f(\vec{\nu}) \nu \frac{d\sigma}{dE_R}, \tag{1.7}$$

In general, the differential cross section is the combination of a Spin-Independent (SI) and a Spin-Dependent (SD) component:

$$\frac{d\sigma}{dE_R} = \left(\frac{d\sigma}{dE_R}\right)_{\mathrm{SI}} + \left(\frac{d\sigma}{dE_R}\right)_{\mathrm{SD}}, \tag{1.8}$$

$$= \frac{m_N}{2\mu_N^2\nu^2}(\sigma_0^{\mathrm{SI}} F_{\mathrm{SI}}^2(E_R) + \sigma_0^{\mathrm{SD}} F_{\mathrm{SD}}^2(E_R)), \tag{1.9}$$

where $\sigma_0^{\mathrm{SI,SD}}$ are cross sections with zero momentum transfer [26]. The form factor, $F(E_R)$ dependent on the momentum transfer ($q = \sqrt{2m_N E_R}$), accounts for the coherence loss, which decreases the event rate for heavy WIMPs or nuclei.

The cross section from SD part is contributed by the interactions of WIMP with the quark axial current. The SI cross section originates from the coupling of the WIMP with particles in the Standard Model. The SI component is proportional to the square of the mass of nucleus (A^2). Although both the SI and SD components are important, the SI cross section usually dominates for heavy targets (A>20). This leads to the dark matter experiments based on targets such as silicon, germanium, xenon, or iodine. For a heavier target nuclei, the WIMP differential event rate decreases more rapidly as the nuclear recoil energy increase [26].

In the standard halo model, the expression for the WIMP differential event rate can be simplified as:

$$\frac{dR}{dE_R} \approx \left(\frac{dR}{dE_R}\right)_0 F^2(E_R) e^{-\frac{E_R}{E_c}}, \tag{1.10}$$

where $\left(\frac{dR}{dE_R}\right)_0$ is the event rate in the $E \to 0$ limit. The characteristic energy scale is given by $E_c = (c_1 2\mu_N^2\nu_c^2)/m_N$ where c_1 is a parameter of order unity that depends on the target nuclei. If the WIMP mass is much smaller than the target nuclei, $m_\chi \ll m_N$, then $E_c \propto m_\chi^2/m_N$. If the WIMP mass is much larger than the target nuclei, then $E_c \propto m_N$. The total nuclear recoil rate is proportional to the WIMP number density, which varies as $1/m_\chi$ [27].

The dependence of the differential event rate on the WIMP and target mass leads to some considerations for the experiments. As the cross section fixed, in order to detect heavy WIMPs, a larger target mass is necessary since the total event rate relies on it. For very light WIMPs, the event rate above the detector threshold energy, E_{th}, may be small due to the rapid decrease of the energy spectrum with increasing recoil energy. If the WIMP is light, $< \mathcal{O}(10\,\mathrm{GeV\,c^{-2}})$, a detector with a low, $< \mathcal{O}(\mathrm{keV})$, threshold energy will be required [26].

1.3.2 Direct WIMP Search

The expected WIMP interaction rate varies for different target materials. As shown in Figure 1.6, the total WIMP interaction rate for Xe and Ar varies in different energy regions. Heavy WIMPs are more likely to produce high energy nuclear recoils, but the total interaction rate is suppressed by the low WIMP flux. On the contrary, light WIMPs may produce very high nuclear recoil rates but they are concentrated in the low energy regions; as a result, an argon-based detector with a typical nuclear recoil energy threshold above $\sim$20 keV would essentially have no sensitivity to $\leq$10 GeV c^{-2} light WIMPs [26].

Compared with the extremely low WIMP interaction rate, the cosmic ray background and environmental radioactivity background are enormous. It is necessary to effectively suppress the background sources in order to make the dark matter experiment feasible. In direct WIMP detection experiment, the main challenge is to suppress and measure the background. The main background sources are γ-rays and Cherenkov radiation from radioactive decays in the detector's construction materials, neutrons from (α,n) and fission reactions from radioactive contaminants of the detector materials, and radioactive isotopes residual in the target medium.

Current detectors commonly deploy large water shields, which effectively reduce cosmic rays, radioactive sources from the surrounding environment, and

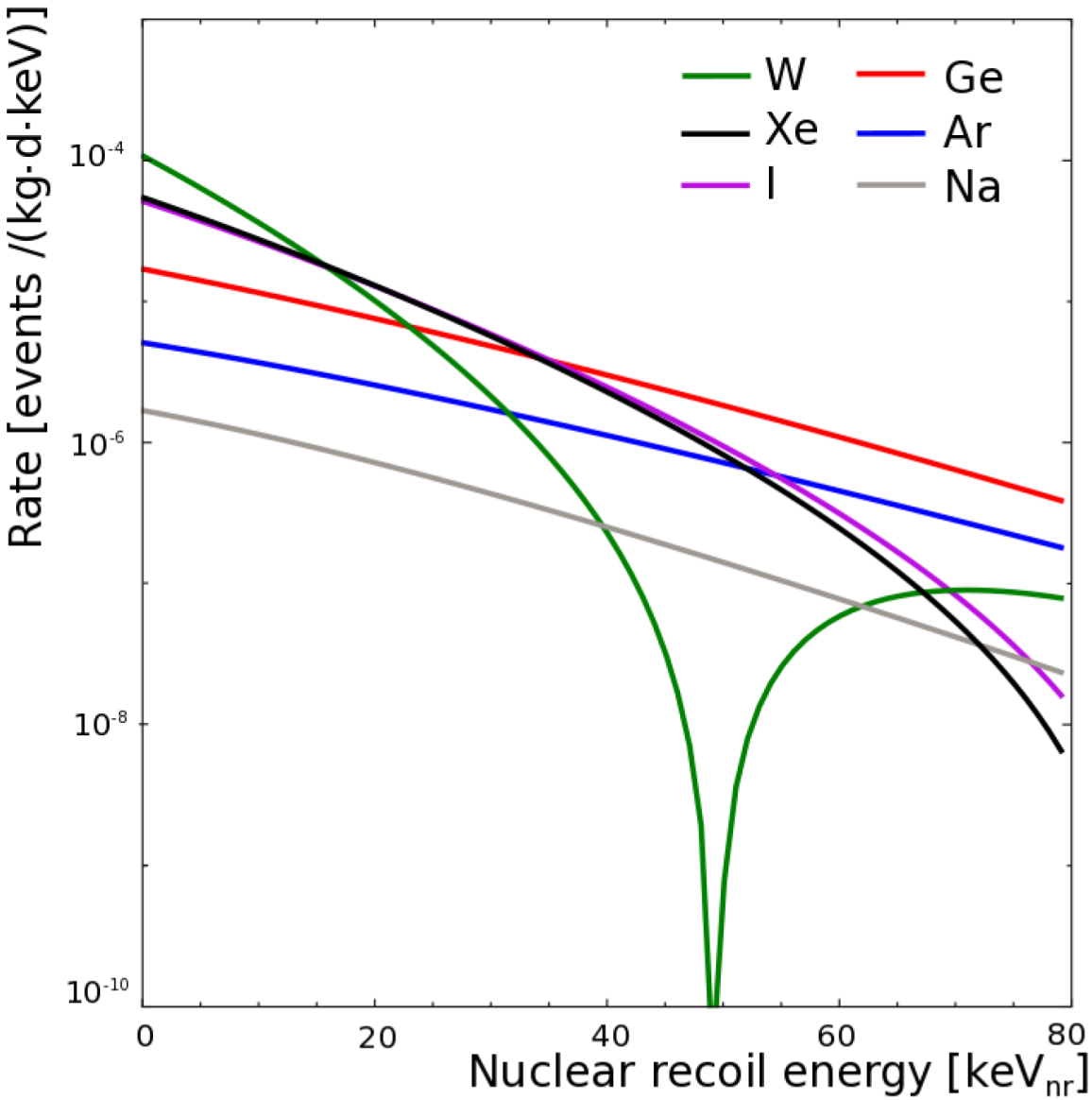

Figure 1.6: Differential event rate of a 100 GeV c^{-2} WIMP with a cross section of 10^{-45} cm^2 in target elements, tungsten (green), xenon (black), iodine (magenta), germanium (red), argon (blue), and sodium (grey) (Figure from Ref. [27]).

muon-induced neutrons by acting as a MV detector. With the water shield, the underground γ-rays and radiogenic neutron flux can be reduced by a factor of 10^6 [28]. The (α,n) and fission neutrons generated via ^{238}U, ^{235}U, and ^{232}Th decays in the detector materials, which are close to the target, dominate the sources of background. The neutron energy spectra and yields are calculated using the source

activity of ^{238}U, ^{235}U, and ^{232}Th in each material and the exact composition of these materials. The neutrons that are difficult to distinguish from a potential WIMP signal are evaluated by simulating them in the detector materials and scaling by the corresponding rate.

In liquid noble gas detectors, some residual radioactive noble isotopes, such as ^{136}Xe, ^{39}Ar, ^{85}Kr, and ^{222}Rn, in the WIMP target medium, can potentially increase the background for dark matter detectors. For example, ton-scale experiments, like XENON1t, trying to reach the WIMP-nucleon cross section down to $10^{-47}\,\mathrm{cm}^2$ level, require purity levels of $\sim 1\,\mathrm{ppt}$ in natural krypton and $\sim 1\,\mu\mathrm{Bq\,kg}^{-1}$ radon. On that level, the background rates from external sources must drop below 1 event per tonne of target material per year in XENON1t [1].

The dark matter experiments based on liquid noble elements, such as xenon and argon, have proven the capability of operating at low background while maintaining high detection efficiency. Since Liquid Xenon (LXe) and Liquid Argon (LAr) are excellent scintillators, the scintillation and ionization signals provide the separation of the incident particles in the detector. In particle, the ratio of the ionization to scintillation signals can effectively distinguish Nuclear Recoil (NR) from Electron Recoil (ER) events. Besides that, the position of an interaction can be reconstructed with precisions up to sub-mm in the z direction and mm in the x-y direction. These features of LXe and LAr along with the capability of scale up to large detectors make them ideal and powerful target medium for the WIMP search. Table 1.2 summarizes some basic properties of xenon and argon. Since xenon is a heavier element, its high liquid density is useful to design a compact detector with efficient self-shielding. It is relatively more expensive to obtain xenon than argon since the fraction of xenon is very low in the atmosphere [29]. In the contrary, the activity of the ^{39}Ar, a β decay emitter, in the atmospheric argon is estimated to be $1\,\mathrm{Bq\,kg}^{-1}$. Therefore the depletion of ^{39}Ar by distillation or extracting from underground argon is necessary.

So far, a depletion factor of $(1.4 \pm 0.2) \times 10^3$ has been achieved by DarkSide-50 using argon extracted from underground mine [30].

Table 1.2: Physical properties of the noble elements Xe and Ar (Table from Ref. [1]).

Property [unit]	**Xe**	**Ar**
Atomic number	54	18
Mean atomic weight	131.3	40.0
Boiling point T_b at 1 atm [K]	165.0	87.3
Melting point T_m at 1 atm [K]	161.4	83.8
Gas density at 1 atm and 298 K [$\mathrm{g\,l^{-1}}$]	5.40	1.63
Gas density at 1 atm and T_b [$\mathrm{g\,l^{-1}}$]	9.99	5.77
Liquid density at T_b [$\mathrm{g\,cm^{-3}}$]	2.94	1.40
Dielectric constant of liquid	1.95	1.51
Volume fraction in Earth's atmosphere [ppm]	0.09	9340
Radioactive isotopes	^{136}Xe	^{39}Ar

So far, the most stringent limits for spin-independent WIMP-nucleon couplings come from the dual-phase LXe experiments XENON [31] and LUX [32]. XENON1T is a dual-phase xenon TPC with total (active) mass of 3.3 t ($\sim$ 2 t) operating at LNGS in Italy. The active LXe volume is viewed by 248 Hamamatsu R11410-21 3" Photo-Multiplier Tubes (PMTs), arranged in two arrays. The PMTs simultaneously detect the Xe scintillation light (S1) at the few keV$_{ee}$ level (keV electron equivalent) at the bottom and top array and ionization (S2) at the single electron level at the top array, induced by particles interacting in the xenon volume. The additional $\sim$1200 kg of the same high-purity LXe, optically separated from the target volume, is instrumented as a veto shield against background events. The ratio of S2 to S1 produced by a WIMP (or neutron) interaction is different from that produced by an electromagnetic interaction, allowing a rejection of the majority of the β/γ background with an efficiency around 99.6 % at 50 % nuclear recoil acceptance. In order to remove the intrinsic contaminants from the xenon, a careful screening and selection campaign for all the detector construction materials, especially those in close proximity to the xenon target, was deployed along with powerful purification techniques. The external γ-rays

and neutrons from the muon and laboratory environment are reduced to negligible level by operating the experiment deep underground at LNGS and also by placing the detector inside a 4 m thick water shield, contained in a stainless steel tank [31].

From November 22, 2016 to January 18, 2017, the XENON1T took 34.2 live-days of blind dark matter search data. The ^{nat}Kr concentration in LXe was reduced to 0.36 ± 0.06 ppt by the end of the run with the help of cryogenic distillation. Some other radioactive isotopes like ^{214}Pb and ^{222}Rn were at the level of (0.8-1.9)$\times 10^{-4}$ events/(kg$\times$day$\times$keV$_{ee}$) (^{214}Pb) and reduced by $\sim$20% (^{222}Rn) respectively. In summary, the electronic recoil background was $(1.93 \pm 0.25)\times 10^{-4}$ events/(kg$\times$day$\times$keV$_{ee}$), the lowest ever achieved background level, in the 5-40 keV$_{nr}$ WIMP dark matter energy range. The nuclear recoils backgrounds includes (0.05 ± 0.01) events from radiogenic neutrons, $\sim$0.02 coherent neutrino-nucleus scattering events while the cosmogenic neutrons at the negligible level. XENON1T also set the most stringent exclusion limits on the spin-independent WIMP-nucleon interaction cross section for WIMP masses above 10 GeV c^{-2}, with a minimum of 7.7×10^{-47} cm^2 for 35 GeV c^{-2} WIMPs at 90% confidence level [33].

The large Underground Xenon (LUX) experiment is a 370 kg (250 kg) total (active) mass LXe TPC in a water Cherenkov shield operated 4850 feet below ground at the Stanford Underground Research Facility (SURF) in Lead, South Dakota, USA. The TPC is 47 cm in diameter and 48 cm in height, viewed by two arrays of 61 PMTs that one array is in the liquid and the other one is in the gas region. The resolution of (x,y) position for small S2 signals (such as those in the WIMP search region in terms of both energy and fiducial volume) is 4 mm to 6 mm, and even better at higher energies. Recent results from LUX includes 332.0 live-days dark matter search data taken from September 11, 2014 to May 2, 2016. The ER background includes compton scattering of γ-rays from radioactive materials in the detector and β decays from ^{85}Kr and ^{222}Rn residual in LXe. The NR background comes from neutrons generated by

detector components and cosmic muons, and coherent elastic nuclear scattering of ^{8}B solar neutrinos. The multiple scatter neutron event rates are much higher than the single scatter events, which have been estimated through radioactivity screening data and simulations. The calibration data taken with dedicated ^{83m}Kr and d-d neutron gun were used to understand and develop analysis algorithm during the initial analysis of the first low-background operation of the instrument. At a WIMP mass of 50 GeV c^{-2}, the WIMP-nucleon spin-independent cross sections above 2.2×10^{-46} cm^2 are excluded at the 90% confidence level [32].

Besides the dark matter detection experiments based on xenon, there are some collaborations using argon as a target of dark matter experiment. DarkSide-50 is a dual-phase argon detector with 46.4 kg (33 kg) active (fiducial) mass, viewed by 38 Hamamatsu R11065 3" PMTs. The TPC is surrounded by a 30 t boron loaded liquid scintillator NV and both detectors are deployed in the Borexino Counting Test Facility (CTF), a 1 kt MV at LNGS. The collaboration has published blind analysis results with 532.4 live-days of dark matter search data taken from August 2, 2015 to October 4, 2017, indicating no evidence of dark matter in the selection region. The Single-PhotoElectron (SPE) response of PMTs in the detector are measured by the insertion of laser pulses via optical fibers. The S1 light yield is measured with $^{83\mathrm{m}}$Kr injected into the argon circulation system. The null-field Underground Argon (UAr) photoelectron yield at the TPC center, at the $^{83\mathrm{m}}$Kr peak energy of 41.5 keV is 8.0 ± 0.2 PE keV^{-1} (PE means PhotoElectron) and this value was stable within $\sim$0.4% during the data taking period [34].

Another experiment using argon as the detection medium is Dark matter Experiment using Argon Pulse-shape discrimination (DEAP-3600), which has collected and published results from 4.4 live-days dark matter search data. It is located 2 km underground at SNOLAB in Sudbury, Ontario, Canada. The spherical acrylic vessel cryostat is viewed by 255 Hamamatsu R5912-HQE PMTs operated near room tem-

perature [35]. Differing from other dark matter experiments, DEAP-3600 uses 2" thick ultraclean acrylic vessel with inner radius of 85 cm as the primary containment for the 3.6 t of liquid argon. The background in DEAP-3600 comes from α activity, neutrons, ^{39}Ar decay and other ER interactions. The sources of α decays are ^{222}Rn, ^{218}Po and ^{214}Po, which are identified with an activity of 1.8×10^{-1} µBq kg^{-1}. The radiogenic neutrons are mainly generated from the radioactive sources, ^{232}Th and ^{238}U, in PMTs. As expected, there is no existence of those neutrons seen in the 4.4 live-days data. DEAP-3600 also has achieved stable light yield of 7.36 PE keV^{-1} and demonstrated better PSD that has leakage probability less than 1.2×10^{-7} at 90% NR acceptance in the energy region [16,33] KeV$_{ee}$. DEAP-3600 set the spin-independent WIMP-nucleon cross section limit in LAr of 1.2×10^{-44} cm^2 for a 100 GeV c^{-2} WIMP (90% C.L.) [36].

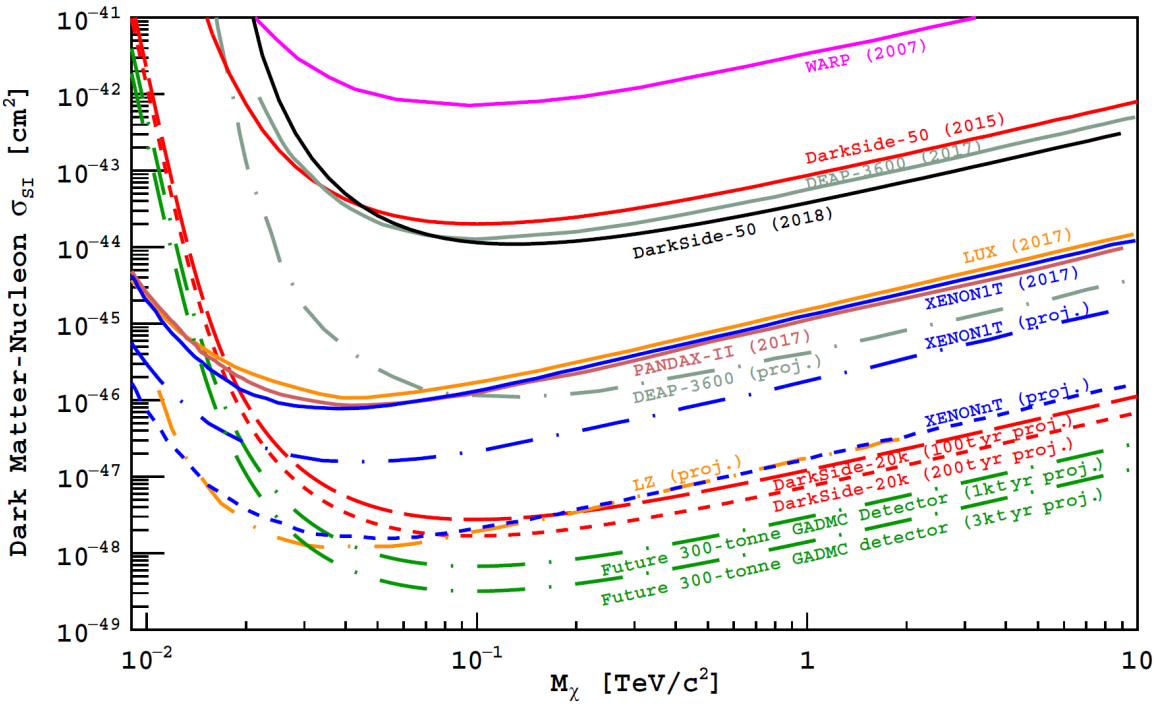

Figure 1.7: Spin-independent WIMP-nucleon cross section 90% C.L. exclusion plot based on results from DarkSide-50, LUX, XENON1T, DEAP-3600 and projected sensitivities of future experiments (Plot from Ref. [34]).

Chapter 2

The DarkSide-50 Experiment

DarkSide-50, a direct search for dark matter, is operating at the underground Laboratori Nazionali del Gran Sasso (LNGS) and searching for rare nuclear recoils possibly induced by WIMPs. The DarkSide-50 detector, as shown in Figure 2.1, is a dual-phase LAr TPC with a 46.4 ± 0.7 kg active target mass. The TPC is viewed by two arrays of low-radioactivity PMTs to detect photons induced by particle interactions in the argon. The TPC is placed inside a 4 m diameter stainless steel sphere that is filled with 30 t boron-loaded organic liquid scintillator acting as a NV. The NV is installed at the center of a steel cylinder, which is 11 m in diameter and 10 m in height. This vessel is filled with 1000 t of highly purified water, referred as MV. This detector can detect Cherenkov light produced by cosmic rays, especially muons.

2.1 TPC Detector

The DarkSide-50 TPC in Figure 2.2 is contained in a cylindrical cryostat that is supported at the center of the NV on a set of leveling rods. The TPC is filled with a total (active) mass of 150 kg (46.4 kg) LAr as the target material. The active volume of LAr is surrounded by Teflon reflector around the sides along with fused silica windows on the top and bottom. The cylindrical wall is a 2.54 cm thick teflon

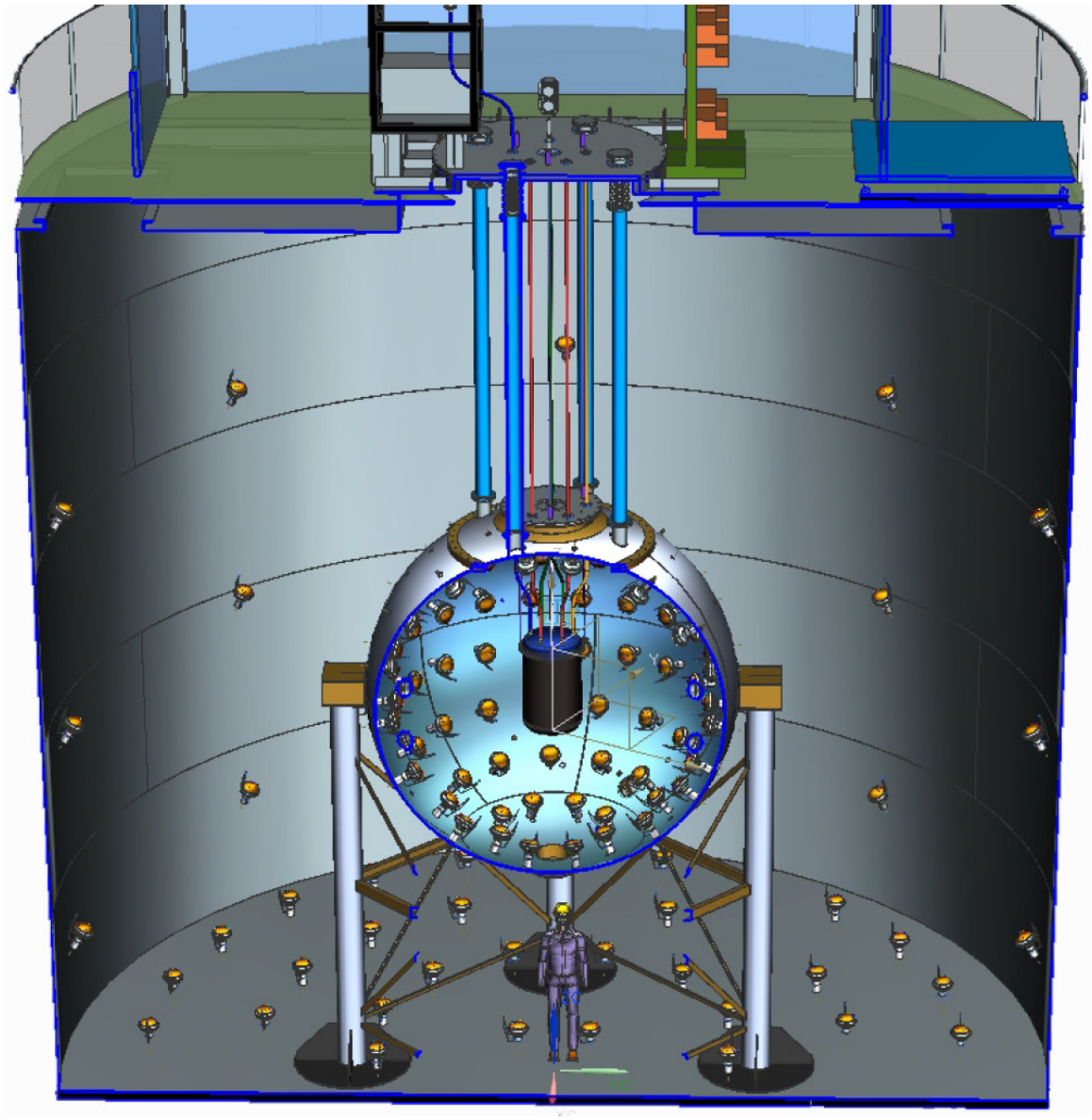

Figure 2.1: Artist rendering of the DarkSide-50 detector.

reflector, as shown in Figure 2.3. Both the teflon reflector and fused silica windows are coated with a wavelength shifter, TetraPhenyl Butadiene (TPB), that absorbs the 128 nm scintillation photons emitted by LAr and re-emits visible photons with a peak wavelength of 420 nm that are reflected, transmitted and detected with high efficiency. The fused silica anode window has a cylindrical rim extending downward to form the "diving bell" that holds a 1 cm thick gas layer of the TPC, produced by

boiling argon within the cryostat (outside the TPC active volume) and delivering the gas to the diving bell. The gas then leaves the bell via a bubbler that maintains the LAr/gas interface at the desired height [37].

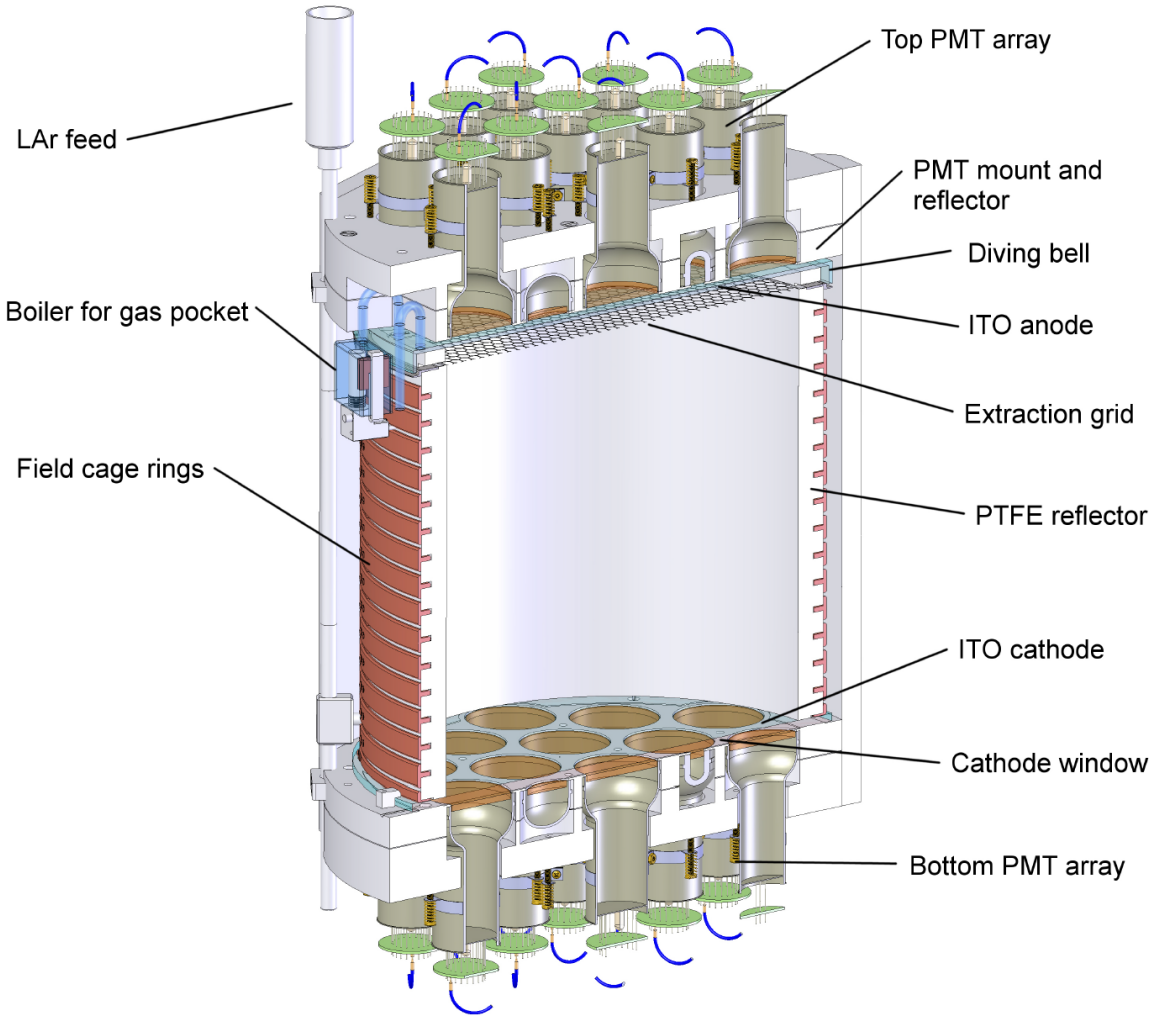

Figure 2.2: DarkSide-50 LAr TPC.

The active LAr is viewed by a total of 38 low-background, high quantum efficiency Hamamatsu R11065 3" PMTs, 19 on the top and 19 at the bottom. The average quantum efficiency of the PMTs at room temperature is 34 % at 420 nm. These PMTs are submerged in LAr and view the active LAr through fused silica windows. The windows are coated with 15 nm thick Indium Tin Oxide (ITO), a transparent conductor that allows the inner window faces to serve as the grounded anode (top)

and cathode (bottom) set at High Voltage (HV) of the TPC while maintaining their outer faces at the average PMT photocathode potential. When the PMTs are hit by an incident photon, an electron can be generated via the photoelectric interactions. The electron is accelerated under electric field applied between the photocathode and the dynode. Once the fast moving electron strikes the dynode, it generates multiple electrons. This process is repeated multiple times on the dynodes inside the TPC. This cascade process produces electrons exponentially, until finally the resulting current is collected through the readout cable. This collected signal is digitized and processed by dedicated electronic circuits. The total charge is the integral of the current collected in the electronic systems over the duration of the pulse. In order to get the number of photons that hit the photocathode of the PMTs, the total collected charge is normalized by the charge of the SPE. A loss of photons is due to the limited collection efficiency of the PMTs, which is reported by Hamamatsu to be $\sim$85 %. Besides that, residual gases inside the PMTs can result in the production of other ionizations moving towards the dynode and amplified by the dynodes. This signal ranges from 1 to a few PE's with a characteristic time delay after the initial signal. These delayed signals, referred as afterpulses, generally happen on a time scale of 10 ns to 20 µs.

The electron drift system consists of the ITO cathode and anode planes, a field cage, and a grid, as shown in Figure 2.4, that separates the drift and electron extraction regions. The grid, 5 mm below the liquid surface, is a hexagonal mesh etched from a 50 µm-thick stainless steel foil and has an optical transparency of 95% at normal incidence. Electric field is applied between the cathode and grid to vertically drift the ionization electrons upwards. In order to keep the drift field uniform throughout the entire active volume, copper rings as shown in Figure 2.3 are installed at graded potentials outside the cylindrical teflon wall. An independently adjustable potential between the grid and anode creates the field that extracts the electrons

Figure 2.3: Left: Teflon wall of DarkSide-50 TPC. Right: Copper rings along with the resistors outside teflon wall.

into the gaseous argon and accelerates them to create a secondary scintillation signal. Over the regular Underground Argon (UAr) data campaign, the electric field is set as $200\,\mathrm{V\,cm^{-1}}$, which results in a maximum drift time of $373\,\mu\mathrm{s}$ and drift speed of $(0.93 \pm 0.01)\ \mathrm{mm\,\mu s^{-1}}$.

Figure 2.4: Left: Bottom TPC PMT array after being coated with ITO. Right: Mesh grid to be installed between liquid and gaseous argon in TPC.

2.1.1 Scintillation and Ionization

The goal of the DarkSide-50 TPC is to detect the signal from possible WIMP-nucleon interactions. If WIMPs exist, they are expected to collide with nuclei and produce recoil atoms with kinetic energy up to a few tens of keV. The argon atoms may lose a fraction of their energy by scattering off other argon atoms through the detector. Some of these recoiling nuclei have too little energy to scintillate and dissipate the kinetic energy as heat. Meanwhile some percentages of these recoiling argon nuclei can slow down and potentially scintillate through the same process as the original recoil nuclei. The remaining fraction of initial energy from the recoiling argon nuclei can ionize and excite the nearby argon atoms, which become ionizations and excitons.

As the energy of the recoiling argon is larger enough, it is possible to excite an electron in the argon exciton to a higher energy state, which leaves a vacancy in the orbit of the exciton. The exciton can then combine with another ground state argon atom nearby to form a Ar_2^* dimer [38]. However, the dimer is not stable and decays to the ground state by emitting a photon with a wavelength of 128 nm. The whole process can be described as:

$$\mathrm{Ar}^* + \mathrm{Ar} \longrightarrow \mathrm{Ar}_2^*, \tag{2.1}$$

$$\mathrm{Ar}_2^* \longrightarrow 2\,\mathrm{Ar} + \gamma, \tag{2.2}$$

In addition, an argon ionization can also form a dimer with a nearby ground state argon atom by sharing one valence electron of the atom. The charged dimer can combine with a free electron that escapes from a nearby argon atom. As a result of this recombination process, the dimer then divides into a doubly excited atom and a ground state atom. The doubly excited atom eventually decay to the ground state

after going through a single excited state and exciton, as described:

$$\mathrm{Ar}^{+} + \mathrm{Ar} \rightarrow \mathrm{Ar}_2^{+}, \tag{2.3}$$

$$\mathrm{Ar}_2^{+} + \mathrm{e}^{-} \rightarrow \mathrm{Ar}^{**} + \mathrm{Ar}, \tag{2.4}$$

$$\mathrm{Ar}^{**} \rightarrow \mathrm{Ar}^{*} + \mathrm{heat}, \tag{2.5}$$

$$\mathrm{Ar}^{*} + \mathrm{Ar} \rightarrow \mathrm{Ar}_2^{*}, \tag{2.6}$$

$$\mathrm{Ar}_2^{*} \rightarrow 2\,\mathrm{Ar} + \gamma, \tag{2.7}$$

The recombination probability depends on the fraction of an electron absorbed by the Ar_2^{+} dimer and the density of ionizations in the LAr. The probability can drastically drop below 1 when the magnitude of the electric field increases, which can force the electrons to travel upwards before the recombination occurs [39].

As one of the products from the processes that the argon exciton and ionization form the dimer, the dimer can end up in the singly excited state with a bound electron orbiting around the Ar_2^{+} core. Both the Ar_2^{+} core and the bound electron have a spin of 1/2. There are four different possible spin combinations due to the variations of the spin directions.

$$\text{singlet} \left\{ \frac{1}{\sqrt{2}}(|\uparrow\downarrow\rangle - |\downarrow\uparrow\rangle) \right. \tag{2.8}$$

$$\text{triplet} \left\{ \begin{array}{l} |\uparrow\uparrow\rangle \\ \frac{1}{\sqrt{2}}(|\uparrow\downarrow\rangle + |\downarrow\uparrow\rangle) \\ |\downarrow\downarrow\rangle \end{array} \right. \tag{2.9}$$

The decay from the singlet state to the ground state occurs within a timescale of $\sim$6 ns [40] due to the same spin of 0. However, the decay of the triplet state, with a total spin of 1, lasts much longer ($\sim$1.5 µs [40]) because the transition is limited by

the conservation of angular momentum. Both decay processes are accompanied with the emission of 128-nm scintillation photons [40].

The different methods that argon exciton and ionization form dimers lead to different probabilities for both channels to form singlet and triplet states. In general, the ratio of exciton to ionization in LAr is $\sim$0.21 for ER and $\sim$1 for NR [37]. The relative population of the fast (singlet) and slow (triplet) components is strongly correlated with the ionization density and hence the nature of the primary ionization particle and the deposited energy. Specifically, the non-unitary recombination probability decreases with the number of ionizations that eventually produce photons, while it increases with the ionization density. The typical fraction of the scintillation light in the fast component is $\sim$0.7 for the heavily-ionizing nuclear recoil events, and $\sim$0.3 for β/γ events - this is the basis of Pulse Shape Discrimination (PSD) [41].

In a dual-phase TPC, ionizing events in the active volume of the TPC result in a prompt scintillation signal referred as "S1". The ionization electrons that escape recombination drift upwards in the LAr under the application of a uniform electric field. Once the electrons reach the surface of the LAr, a much larger electric field extracts the electrons fully into the gaseous argon phase between the LAr surface and the TPC anode. The electric field in the gas is large enough to accelerate the electrons so that they excite the argon, resulting in a secondary photons, "S2", that is proportional to the collected ionization. The S2 signals are detected by the top PMTs as a delayed coincidence relative to S1. The drift time of the electrons give the vertical position to sub-millimeter precision [42]. Since S2 production occurs very close to the top PMTs, the signal distribution will be strongly disuniform and can be used to locate the ionization event in the horizontal plane with precision to <1 cm. Therefore, the TPC provides the complete 3D-position information for the event. In this mechanism of a dual phase TPC, an event is detected by observing both the scintillation photons and the free electrons [43].

Besides the powerful discrimination of S2/S1 ratio, it is also possible to separate the ER and NR by the time profile of LAr scintillation pulses, which is the PSD technique as mentioned above. f_{90}, a common parameter as shown in Figure 2.5, identifies the fraction of the scintillation light that occurs in the first 90 ns of the scintillation pulse. The difference of the decay time of the singlet and triplet state dimers leads to the development of the f_{90} parameter. Within 90 ns, basically all of the singlet dimers have decayed while only few of the triplets have done so. The combination of the S2/S1 ratio and f_{90} has excellent discrimination power for ER and NR events, as shown in Figure 2.6.

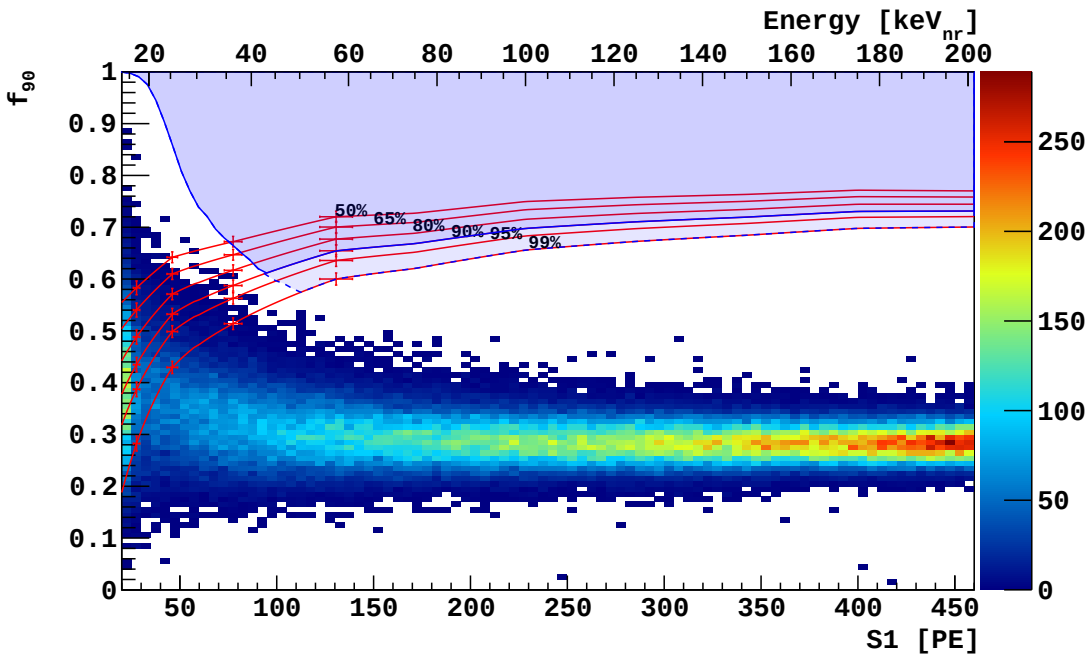

Figure 2.5: Distribution of events in the f_{90} vs S1 plane surviving all cuts in the energy region of interest. Shaded blue with solid blue outline is the WIMP search region. The red curves with red cross points are derived from the SCENE measurements of NR acceptance (Plot from Ref. [37]).

2.1.2 ^{39}Ar Background

Argon-based dark matter experiment must confront the presence of ^{39}Ar. In the atmosphere, ^{39}Ar is mostly produced when a cosmogenic neutron interacts with an

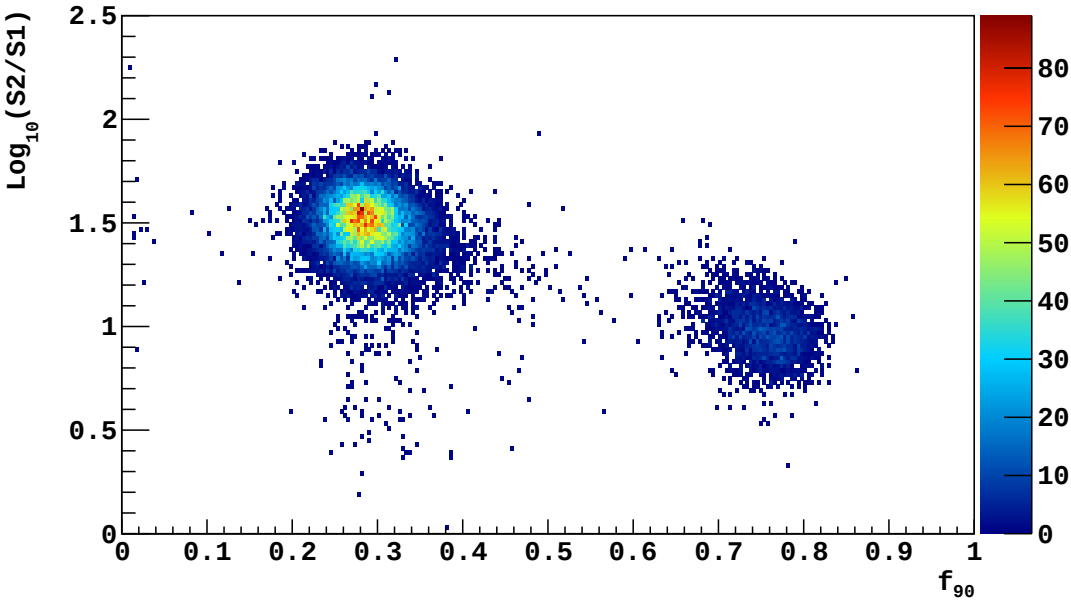

Figure 2.6: Combined discrimination power from S2/S1 and f_{90} to distinguish ER ($f_{90} \sim 0.3$) from NR ($f_{90} \sim 0.75$) (Plot from Ref. [37]).

^{40}Ar target and knocks out two neutrons as follows:

$$^{40}\mathrm{Ar} + n \longrightarrow {}^{39}\mathrm{Ar} + 2\,n. \tag{2.10}$$

The ^{39}Ar isotope is a β emitter with an endpoint energy of 565 keV and half-life of 268 yr [44]. ^{39}Ar can decay as follows:

$$^{39}\mathrm{Ar} \longrightarrow {}^{39}\mathrm{K} + e^- + \bar{\nu}_e. \tag{2.11}$$

^{39}Ar is present with an activity of (1.01 ± 0.02) Bq kg^{-1} in commercial argon extracted from the atmosphere [44]. The corresponding isotope abundance ratio of ^{39}Ar to ^{40}Ar is $(8.0 \pm 0.6) \times 10^{-16}$ [44].

Although the relative ^{39}Ar abundance is small, the background from ^{39}Ar decay in a large scale detector filled with Atmospheric Argon (AAr) can be enormous. In the first commissioning runs of DarkSide-50, AAr was used, which contained a large

fraction of background from ^{39}Ar decays, as indicated by the black curve shown in Figure 2.7. The ^{39}Ar decay rate in 1 t of atmospheric argon is approximately 3×10^{10} in one year. Compared with ^{39}Ar rate, the expected WIMP induced signal rate is at the level of $10\,\mathrm{t}^{-1}\,\mathrm{yr}^{-1}$ above a 20 keV energy threshold, assuming that the dark matter density of $\sim$0.3 GeV m^{-2} in the Earth's neighborhood can be attributed to 100 GeV c^{-2} mass WIMPs, and the estimation of the WIMP-nucleon elastic scattering cross section is 10^{-45} cm^2. It leads to the ratio of signal to background close to 10^{-10}, which is a big challenge for argon-based direct dark matter searches [45].

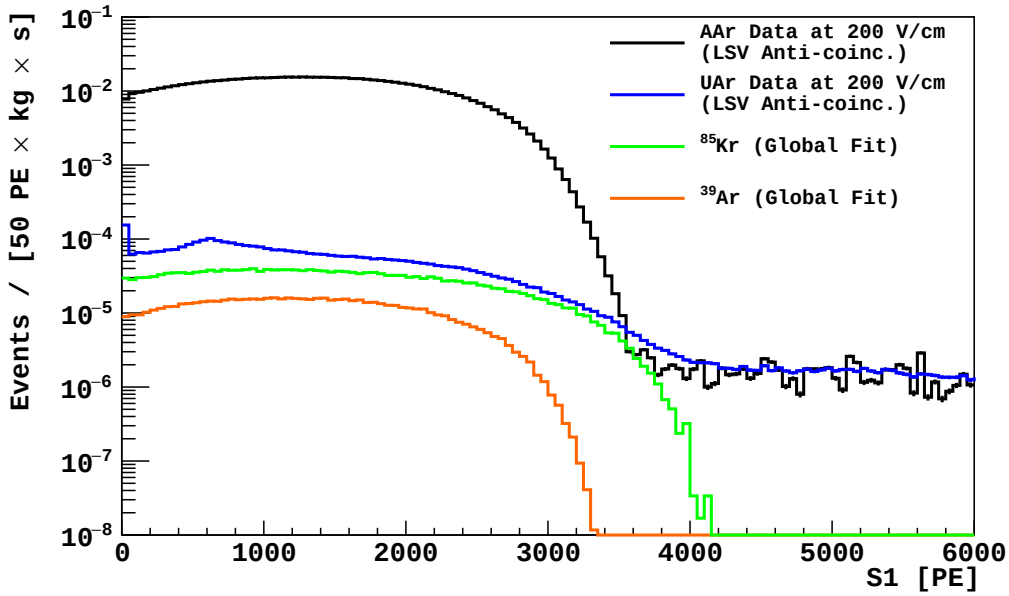

Figure 2.7: S1 spectra from single-scatter events in AAr (black) and UAr (blue) data taken with 200 V cm^{-1}. The ^{85}Kr (green) and ^{39}Ar (orange) levels come from a MC fit (Plot from Ref. [30]).

In addition, it is important for the argon-based detector to scale to large mass as required by modern dark matter search. However, the ^{39}Ar activity in the atmospheric argon restricts the size of the detector. An ionization electrons travel with the velocity of a few millimeters per microsecond. The drift time in a ton scale detector ($\sim$1 m dimension) is estimated to be $\sim$500 µs [46]. With an ^{39}Ar activity of $\sim$1 Bq kg^{-1}, the

expected ^{39}Ar rate would be $\sim$1000 Hz, which means one or more ^{39}Ar decay signals are present within $\sim$50 % of the $\sim$500 µs electron drift windows.

Besides the AAr, ^{40}Ar can be found underground as a result of ^{40}K decay, which exists along with ^{39}K. ^{39}K can produce ^{39}Ar via the ^{39}K(n,p)^{39}Ar interaction with neutrons emitted from uranium and thorium chains in the surrounding rocks underground. Although there is still trace of ^{39}Ar underground, the concentration is significantly lower than that in the atmosphere [47]. Therefore, the AAr was replaced with UAr in DarkSide-50. The ^{39}Ar activity of the UAr was first measured in 2011 using a small detector at the KURF underground laboratory, which set an upper limit of 6.6 mBq kg^{-1}, or factor 150 reduction compared to ^{39}Ar activity in atmospheric argon. After purification, the ^{39}Ar activity in UAr was reduced to 0.73 ± 0.11 mBq kg^{-1} as shown in the energy spectrum (the blue curve) in Figure 2.7. The ^{39}Ar activity in UAr corresponds to a reduction by a factor of $(1.4 \pm 0.2) \times 10^3$ relative to AAr [30].

2.2 Outer Detector

2.2.1 Liquid Scintillator Detector

The DarkSide-50 TPC is immersed inside the NV, as shown in Figure 2.8. The NV is a 4 m in diameter stainless steel sphere filled with 30 t of boron-loaded liquid scintillator. The NV is viewed by 110 Hamamatsu R5912 8" PMTs, which are mounted on the inner surface of the sphere. The sphere is covered with Lumirror, a reflecting foil used to increase the light collection efficiency. Since the TPC is fully surrounded by the NV, the γ-rays and neutrons that leave prompt signals in the NV after scattering in the TPC are highly likely to be vetoed, and that helps us understand the coincidence backgrounds in DarkSide-50.

The need for the NV is motivated by the difficulty of separating neutrons from WIMP-nucleon interactions, which are indistinguishable in the TPC even with the

Figure 2.8: Inside view of the NV with the TPC cryostat in the center, suspended by three adjustable support rods.

help of PSD and the S2/S1 ratio. The NV is composed of a volume of material with a high neutron interaction cross section so that neutrons can be captured in the liquid scintillator after scattering in the TPC. In addition to labeling the neutron backgrounds, the NV can also hep us understand the γ-rays from the detector materials.

The boron-loaded liquid scintillator has three components: 1,2,4-Trimethylbenzene also known as PseudoCumene (PC, $C_6H_3(CH_3)_3$) as the primary solvent, TriMethylBorate (TMB, $B(OCH_3)_3$) as the second solvent loaded with boron, and 2,5-Diphenyloxazole (PPO, $C_{15}H_{11}NO$) as wavelength shifter. The liquid scintillator is currently composed of 95 % PC by mass, $1.4\,\mathrm{g\,L^{-1}}$ PPO and 5 % TMB [48].

2.2.2 Scintillation and Neutron Capture Mechanism

The primary scintillator, PC, is an organic flammable colorless liquid with a strong odor. It occurs naturally $\sim$3 % in coal tar and petroleum. The same scintillator was first used in the Borexino experiment, which obtained high purity scintillator along with good scintillation efficiency [49].

Scintillation light production in liquid organic scintillator is mainly due to the hydrocarbon compounds that contain benzene ring structure in the molecules. An ionizing particle can lose a fraction of its energy when it passes through the organic material, which produces excitations with a time scale of 10^{-12} s to 10^{-11} s. The excitations are not stable and quickly relax into singlet and triplet states. The process includes de-excitation with light emission. The transition from the singlet state to the ground state takes a few nanoseconds and emits fluorescence (prompt light). That from the triplet state to the ground state lasts much longer (on the time scale of μs-ms) with the emission of phosphorescence (delayed light) [50].

The light emission, especially in the singlet excitations, may be suppressed by interactive processes including singlet ionization quenching. In this process, two singlet states interact, leaving one in the ground state while the other jumps to a super-excited singlet state. The super-excited state may emit only half the amount of light that could have been produced by the original two singlet excitations [50]. The fraction of prompt light becomes dramatically lower when the density of the singlet excitations are higher.

The effects of these interactive processes are observed in different interactions induced by neutron and γ-ray events. When neutron interacts in the material, the NR deposits energy with much higher dE/dx than the ER from γ-ray interactions. As the dE/dx gets larger, it leads to higher excitation density and more singlet ionization quenching. In turn, there is relatively more delayed light and less prompt light in neutron interaction events.

Birks' Law illustrates the effect of scintillation light suppression through ionization quenching. It is an empirical formula for the light yield per path length as a function of the energy loss per path length for a particle traversing a scintillator, which is not linear at high energy loss. The relation is described as:

$$\frac{dL}{dx} = S\frac{dE/dx}{1 + kB \cdot dE/dx}. \tag{2.12}$$

where L is the light yield, S is the scintillation efficiency, dE/dx is the energy loss of the incident particle per path length and kB is the Birks' constant that depends on the material.

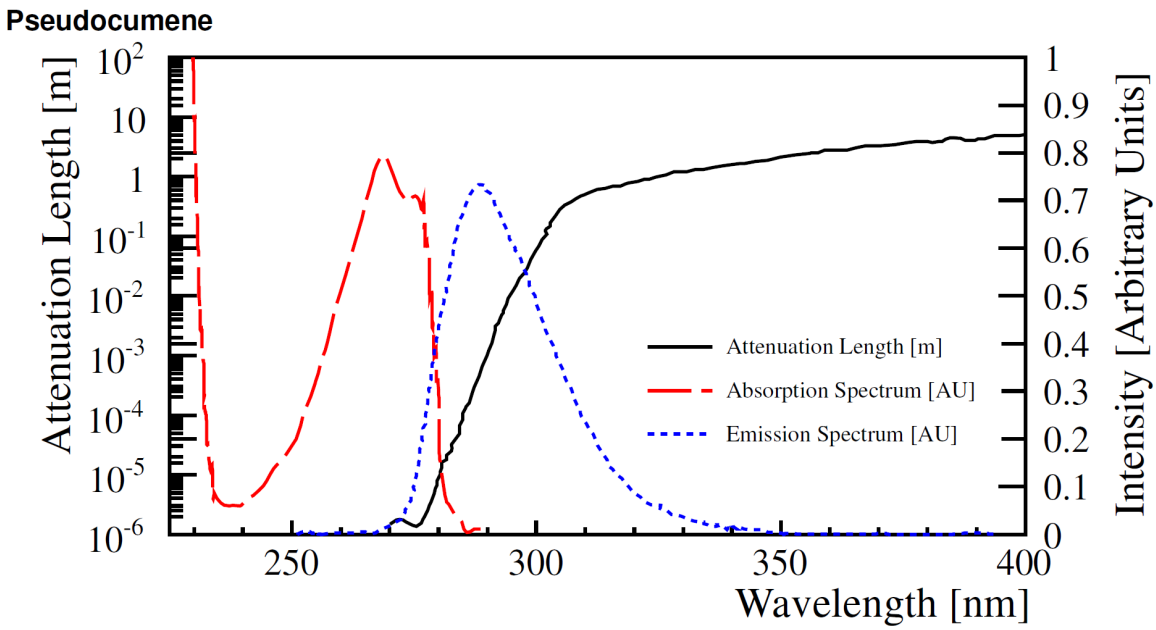

Figure 2.9: Attenuation length (black) , emission (dash blue) and absorption (red) spectrum of pure PC (Figure from Ref. [47]).

Figure 2.9 shows the characteristic pattern of the pure PC, which indicates the emission and absorption spectrum of photons in pure PC. Since the NV is a 4 m diameter sphere, there is a relatively long path for photons to travel before they are detected in the PMTs. It is possible for the photons to be absorbed by the scintillator because of the overlap of the emission and absorption spectrum as shown in Figure 2.9.

This attenuation can highly decrease the amount of light collected and compromise the sensitivity of the NV.

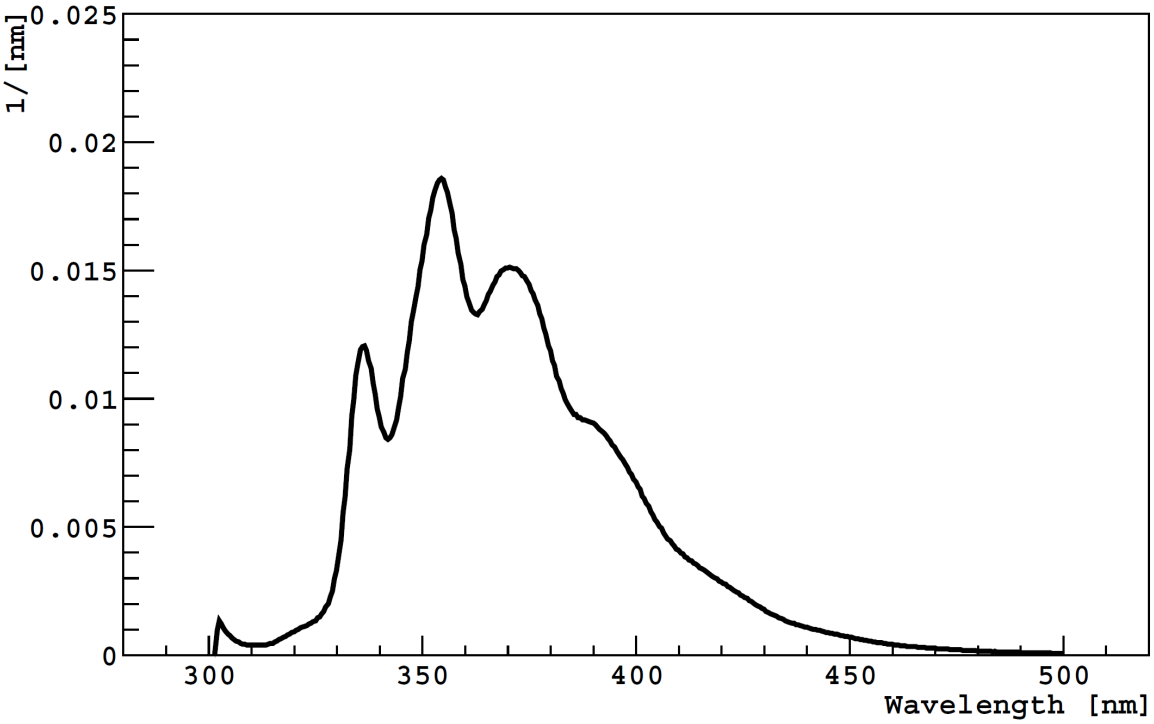

Figure 2.10: Photon emission spectrum of PPO (Figure from Ref. [51]).

The practical way to reduce light loss due to self-absorption is to add wavelength shifter, in this case PPO. It converts the shorter wavelength to an output spectrum that peaks at ∼360 nm, which is in the range of UV light, as shown in Figure 2.10. This effect, referred as Stokes shift, occurs when the PPO molecule absorbs photons of shorter wavelength. The electron in the molecule enters an excited state, which only remains for about 10^{-8} s [50]. During the lifetime of an excited state, a part of the excitation energy is dissipated through interactions, like vibrational relaxation, with the material. After losing a fraction of the excitation energy, the molecule returns to the ground state accompanying with the emission of photons that have a longer wavelength.

Besides the Stokes shift, PPO is also very efficient and has a short scintillation time mainly due to its benzenoid ring structure. Because of their similar structure,

the energy deposited in PC can be thermally, non-radiatively, transferred to PPO molecules in a very efficient way. As a result, adding only a small concentration of PPO to PC is generally necessary in order to increase the scintillation efficiency and the attenuation length of light in the scintillator. It also makes the light signal faster, allowing tighter prompt coincidence cuts since PPO scintillates much faster than PC. As for the increase of the wavelength, the 360 nm photons, far away from the absorption of PC, are more sensitive to PMTs, which increase the light collection efficiency. In Figure 2.10, the upper half of the PPO emission spectrum has a long attenuation length, which makes it possible for NV to reach a higher light yield [52].

Although NV with the mixture of PC and PPO is efficient at detecting scintillation light from incident particles, it may leave light coming from neutrons undetected. To avoid losing these signals, an extra component, TMB, is loaded to the scintillator. TMB is a white crystal power that forms a pale blue-green light in solution with ethylacetate. It degrades by sunlight and fluorescent lights and should be kept in the dark.

The main effective component in TMB is ^{10}B isotope, which has a natural abundance of ∼20% and a thermal neutron capture cross section of 3838 b. When a neutron captures on ^{10}B, there are two possible reactions:

$$^{10}\mathrm{B} + n \rightarrow {}^{7}\mathrm{Li}(1015\,\mathrm{keV}) + \alpha(1775\,\mathrm{keV}) \qquad (6.4\,\%), \tag{2.13}$$

$$^{10}\mathrm{B} + n \rightarrow {}^{7}\mathrm{Li}^{*} + \alpha(1471\,\mathrm{keV}) \qquad (93.6\,\%), \tag{2.14}$$

$$^{7}\mathrm{Li}^{*} \rightarrow {}^{7}\mathrm{Li}(839\,\mathrm{keV}) + \gamma(478\,\mathrm{keV}) \qquad . \tag{2.15}$$

The decay to the excited state of ^{7}Li produces a 478 keV γ-ray that deposits energy into the scintillator, generates scintillation light with very little quenching and eventually gets collected by the PMTs. On the other hand, the scintillation lights from α and ^{7}Li with relatively high energy are heavily suppressed, to 50-60 keV$_{ee}$, by

ionization quenching due to the high stopping power and consequently short track length [53].

Besides ^{10}B, ^{1}H and ^{12}C in the organic scintillator can also capture neutrons in the following reactions:

$$^{1}\mathrm{H} + \mathrm{n} \longrightarrow {}^{2}\mathrm{H} + \gamma \qquad \sigma = 0.33\,\mathrm{b}, \tag{2.16}$$

$$^{12}\mathrm{C} + \mathrm{n} \longrightarrow \begin{cases} {}^{13}\mathrm{C} + \gamma(3090\,\mathrm{keV}) \\ {}^{13}\mathrm{C} + \gamma(4945\,\mathrm{keV}) \\ {}^{13}\mathrm{C} + \gamma(1860\,\mathrm{keV}) \end{cases} \qquad \sigma = 0.0034\,\mathrm{b}. \tag{2.17}$$

where σ is the thermal neutron capture cross section.

The capture time and relative rate of neutron capturing on ^{10}B, ^{1}H, and ^{12}C can be calculated based on the cross section of each isotope and the chemical concentrations of different components. During the WIMP search compaign of DarkSide-50, scintillator with 95 % mass fraction of PC, 5 % TMB and 1.4 g L^{-1} PPO is used. The neutron capture time is ∼22 µs with ∼8 % of the neutrons capturing on ^{1}H.

With the concentration of the scintillator, there are two signals that can be detected when a neutron enters the NV after scattering in the TPC. The first signal is the prompt thermalization signal from the neutron slowing down in the NV. Neutron scatters off the nuclei mostly on hydrogen and carbon with most of its energy lost to the hydrogen. The efficiency of the NV response to the neutron thermalization signals will be further discussed in the Neutron Calibration section. The neutron thermalization happens within ∼100 ns in the NV. The second signal is the delayed signal from neutron capture. After thermalization, neutron can then be captured on isotopes like ^{10}B, ^{1}H, and ^{12}C on a time scale of 1-100 µs. An important feature of the neutron capture process is the independence of the incident neutron energy, which means a neutron that thermalizes in the NV or has too little energy to produce a

detectable prompt signal may still produce a detectable capture signal. Therefore, a detector with low threshold can achieve high neutron detector efficiency.

2.2.3 Water Cherenkov Detector

The outermost detector that surrounds the NV is the Water Cherenkov Detector (WCD) or MV, which is a stainless steel cylinder 11 m in diameter and 10 m in height. As shown in Figure 2.11, there are 80 20-cm diameter ETL 9351 8" PMTs installed inside the MV with 24 of them on the floor facing upwards and 56 PMTs on the side wall facing towards the center of the MV. The PMTs have a peak quantum efficiency of ∼25 % at 380 ns and a dark rate of ∼2500 Hz. The MV is filled with ∼1000 t of ultra-purified water. The inner surface of the MV and the outer surface of the NV are both covered with layers of Tyvek reflector. The reflectivity of this material is measured to be greater than 96 % in air and 99 % in water for light of 300-800 ns in wavelength.

Cosmogenic neutron has higher energy than radiogenic neutron, and can penetrate much further through matter. The feature of the MV is to veto signals produced by muons that may be in coincidence with a cosmogenic neutron by detecting the associated Cherenkov light generated by these particles. Locating DarkSide-50 underground reduces the flux of cosmogenic neutrons by reducing the rate of cosmic-ray muons. However, the rocks surrouding the underground laboratory are likely to have some natural radioactivity. In particular, the relatively high abundance of U and Th isotopes in the rocks increases the amount of ambient radiation. The second feature of the MV is to provide neutron shielding to the TPC and NV.

Cherenkov light from an electromagnetic radiation is emitted when charged particles pass through a dielectric medium with a speed greater than the phase velocity of light in the medium. The charged particles polarize the molecules of that medium, which turn back rapidly to their ground state, emitting radiation in this process.

Figure 2.11: View inside the MV with NV in the center. The inner surface of the MV and the outer surface of the NV are both covered with layers of Tyvek. A total of 80 PMTs are installed on the floor and the side wall of the MV.

In Figure 2.12, the particle (red arrow) travels in a medium with speed v_p such that $c/n < v_p < c$, where c is the speed of light in the vacuum, and n is the refractive index of the medium. The refractive index of water is 1.33. The ratio between the speed of the particle and the speed of light is defined as $\beta = v_p/c$. The emitted light (blue arrows) travels at speed $v_{\text{em}} = c/n$, therefore $\cos(\theta) = 1/n\beta$. So the threshold kinetic energy is:

$$E_k = E_0 \left(\frac{n}{\sqrt{n^2 - 1}} - 1 \right). \tag{2.18}$$

Here $E_0 = m_0 c^2$ is the static energy of the incident particle. For the electron, the threshold of the kinetic energy is 0.264 MeV. Based on the Frank-Tamm equation [55], the number of Cherenkov photons, N, produced per distance, x, is described by:

$$\frac{d^2N}{dxd\lambda} = \frac{2\pi\alpha Z^2}{\lambda^2} \left(1 - \frac{1}{n^2(\lambda)\beta^2} \right), \tag{2.19}$$

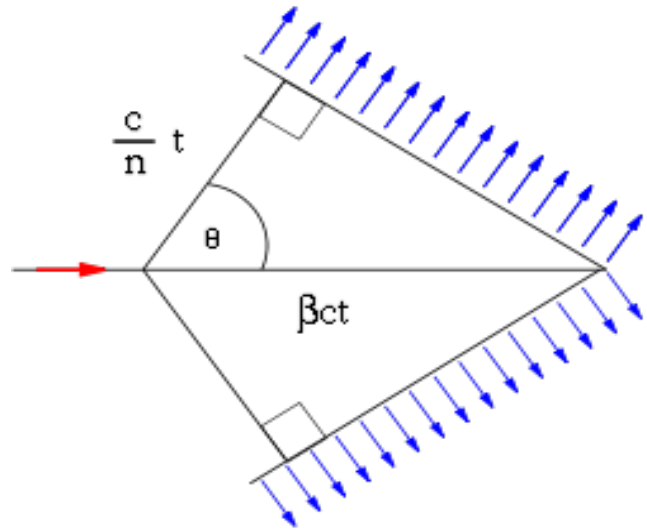

Figure 2.12: Principle of the Cherenkov effect. After time t, the incident particle, denoted by the red arrow, travels a distance of βct. Simultaneously, the emitted light represented by the blue arrow moves ct/n away in the angle of θ (Plot from Ref. [54]).

where α is the fine structure constant, Z is the charge of the moving particle, λ is the wavelength of the emitted photon, n is the refractive index, and β is defined as:

$$\beta^2 = 1 - \frac{m_0^2 c^4}{m_0 c^2 + K}, \tag{2.20}$$

where K is the kinetic energy of the electron. Therefore, as long as these photons are detected, the MV should be able to veto the cosmogenic events very efficiently.

2.3 Data Acquisition

The DarkSide-50 data are composed of basic units referred to as events. Each trigger of the TPC corresponds to one event. At the raw data level, each event consists of a collection of raw waveforms from each channel. There are 38 channels in the TPC while there are 110 and 80 channels in the NV and MV. In order to carry out the statistical analysis of events, it is important to translate raw waveforms into analysis variables.

Since the raw waveform data contain a big fraction of useless noise, two main steps are taken to reduce the space of data, which are DarkArt and SLAD (SLim Analysis Data). DarkArt is the first stage of analysis over the raw waveform data, which is normally called as event reconstruction. After that, SLAD performs a further reduction on the DarkArt output files and generates plain ROOT files.

2.3.1 DarkArt

Since the DAQ system are the same for the NV and MV, their analog signals are also treated identically. After the analog signal is dissociated from the HV, it is amplified by a factor of ten with a front-end module. In the normal data taking mode, the veto trigger is initiated by the TPC. After receiving a trigger from the TPC, the veto data are recorded by the veto digital electronics within an data acquisition time window, which is several neutron capture times wide. During the first phase, the neutron capture time was $\sim$2.2 µs. At that time, the data acquisition window was set to 70 µs allowing the NV to detect neutron capture signals from TPC materials, such as ^{19}F or ^{56}Fe. After replacing the scintillator, the neutron capture time increased to $\sim$22 µs and the data acquisition window was set to 140 µs and then extended to 220 µs.

After the signals are recorded, a zero-suppression algorithm is applied to only store part of the digital waveform. The signals removed have an amplitude below a quarter of a single-photoelectron pulse or a timescale of 16 ns (corresponding to 20 samples) before and after the pulse. With this mechanism of storing data, disk space and the computation time are saved. The zero suppression algorithm, as shown in Figure 2.13, specifies a threshold, a minimum width, and a number of pre- and post-samples. When the waveform crosses the threshold and stays below threshold for the number of samples specified by the minimum width, the algorithm returns the entire waveform between both threshold crossings, starting with the specified

number of pre-samples before the first crossing and ending with the specified number of post-samples after the final crossing.

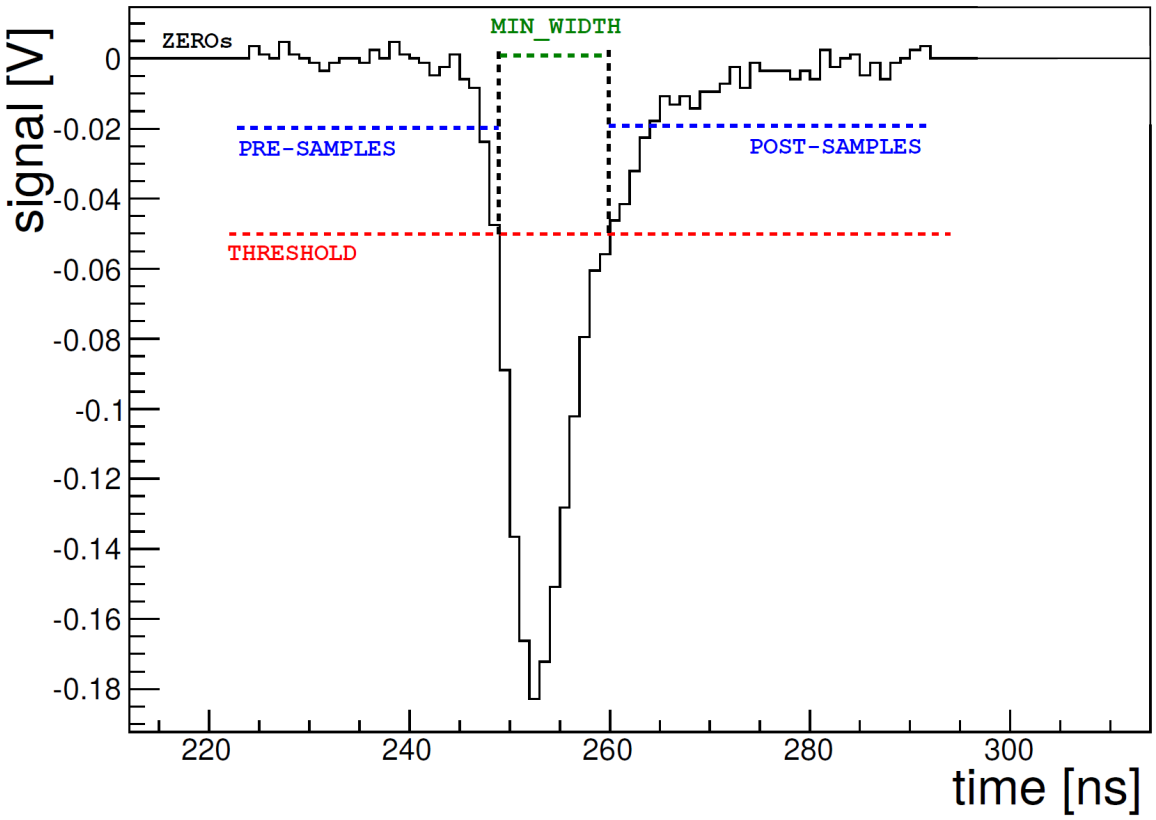

Figure 2.13: Example of zero suppressed waveform in the NV (Figure from Ref. [47]).

If the waveform goes below the threshold and then back above the threshold before the specified number of post-samples have passed, the algorithm waits for the waveform to drop back below threshold and then starts counting post-samples starting from scratch. Therefore, if two pulses appear on the same channel with overlapping zero-suppression windows, they are instead combined into one large zero-suppressed pulse. Data were taken with a zero suppression threshold of $\sim$0.25 PE, a minimum width of 4 samples, and the number of pre-samples and post-samples set to 20. The output of the zero suppression algorithm is the pulse [56].

In DarkSide-50, a pulse is defined as the segment of each waveform for each channel that survives zero-suppression. The pulse is later corrected to take the effects from

the electronics into consideration. They include the waveform pedestal affected by the residual DC offset, the pulse saturation from the finite vertical range of the digitizer, and variances of the PMT gain on each channel. A baseline, determined by the average of the first 15 samples of each pulse, is subtracted from the pulse so that each veto channel shares the same offset.

The maximum value of the waveform amplitude is close to that of 7 overlapping SPE pulses. However, the total amplitude may become larger than this maximum value due to the pile-up of too many photoelectrons, which leads to the pulse saturation around the maximum amplitude value. This may happen when a NV scintillation event occurs close to a PMT. The saturation event is determined by 3 consecutive samples that share the amplitude value in the upper 90 % of the amplitude range. The shape of a saturated pulse peak is estimated with a triangle, in which two vertices are the first and last saturated samples while the third vertex is the intersection of the two lines that extrapolate the rising and falling edge of the pulse. The integral of this saturated pulse also includes the area of this triangle [51].

After reconstruction and gain calibration, the pulse waveforms of each channel are added together to give a sum waveform. A typical scintillation event in the NV, which appears in multiple pulses, lasts a few hundred nanoseconds, which is similar to Cherenkov events in the MV. To identify and reconstruct the whole scintillation or Cherenkov event, a clustering algorithm was developed. It iteratively searches for the clusters based on the amplitude of the sum waveform. It identifies peaks of the sum waveform once its amplitude exceeds the threshold, which is about 2 times the amplitude of SPE. Once a peak is located, it scans the sum waveform before and after the peak time to determine the start and end of the cluster, which requires at least 20 ns gap between pulses. As shown in Figure 2.14, the clustering algorithm then moves to the next highest peak and repeats the search until the amplitude of peak

drops below a threshold of 2 PE. The total charge of a cluster is calculated based on the integral of the sum waveform from the start to the end time of a cluster [51].

Besides the cluster, additional variables independent of the cluster, such as Regions Of Interest (`ROI`) and `Slider`, are calculated to avoid missing a neutron event in coincidence with the TPC. The `ROI` is the total integral charge of pulses in a specified time window. Instead of integrating the sum waveform in the entire window, `Slider` looks for the greatest integral within the sub-window by scanning from the start to the end time. A specific start and end time of each `ROI` is defined with respect to the TPC trigger time. The integral of the sum waveform between the start and end of the `ROI` represents the total amount of scintillation light in the time window. In the next sections, I will discuss details on the efficiency and acceptance loss for those `ROIs`. Similarly, a start and end time is also specified in the `Slider`. It also requires a sub-window width (500 ns). In the case that the clustering algorithm misses a scintillation event, the `Slider` can efficiently identify it by the highest charge within the window [51]. In particular, it helps identify the delayed neutron capture events in the NV with a high efficiency, which is the main focus of my thesis.

2.3.2 SLAD

The DarkArt output, which requires additional libraries, is not immediately readable for the purpose of analysis. In order to make a more userful output file, the SLAD program is used. SLAD takes the DarkArt output file that is usually up to a size of 1 GB per run and reprocesses some variables, shrinking the size to tens of MB. Furthermore, SLAD provides more information associated with the pulse and event for the purpose of data analysis. For instance, SLAD identifies S1 and S2 pulses for each event and provides more analysis-friendly variables, including estimators for the S1 and S2 amplitude, corrections to those estimators, drift time and x-y position

reconstruction, etc. SLAD also selects widely used variables and leaves the extremely broad set of variables to the original DarkArt output file.

Since the DAQ system in the TPC and outer detectors are different, it's necessary to match the TPC events with the NV events. With this goal, SLAD takes both DarkArt TPC and DarkArt Outer Detector (OD) output files and matches them based on the timestamp from both detectors. In order to get that, the timestamps of both TPC and NV detectors are derived from `gps_fine` and `gps_pps` variables. The `gps_fine` is the GPS time counter that counts clock cycles (50 MHz) while the `gps_pps` counts the number of seconds from the start of the run. In addition to these two time variables, there is a fixed time difference, -6584 ns, between the TPC and NV. If the timestamp in the TPC and NV falls within 100 ns after both satisfying some basic conditions, the TPC and NV events are matched together, which is tagged with the `veto_present` variable in the SLAD file. So, SLAD provides a complete and lightweight data set, ready for analysis, from all the three detectors in DarkSide-50.

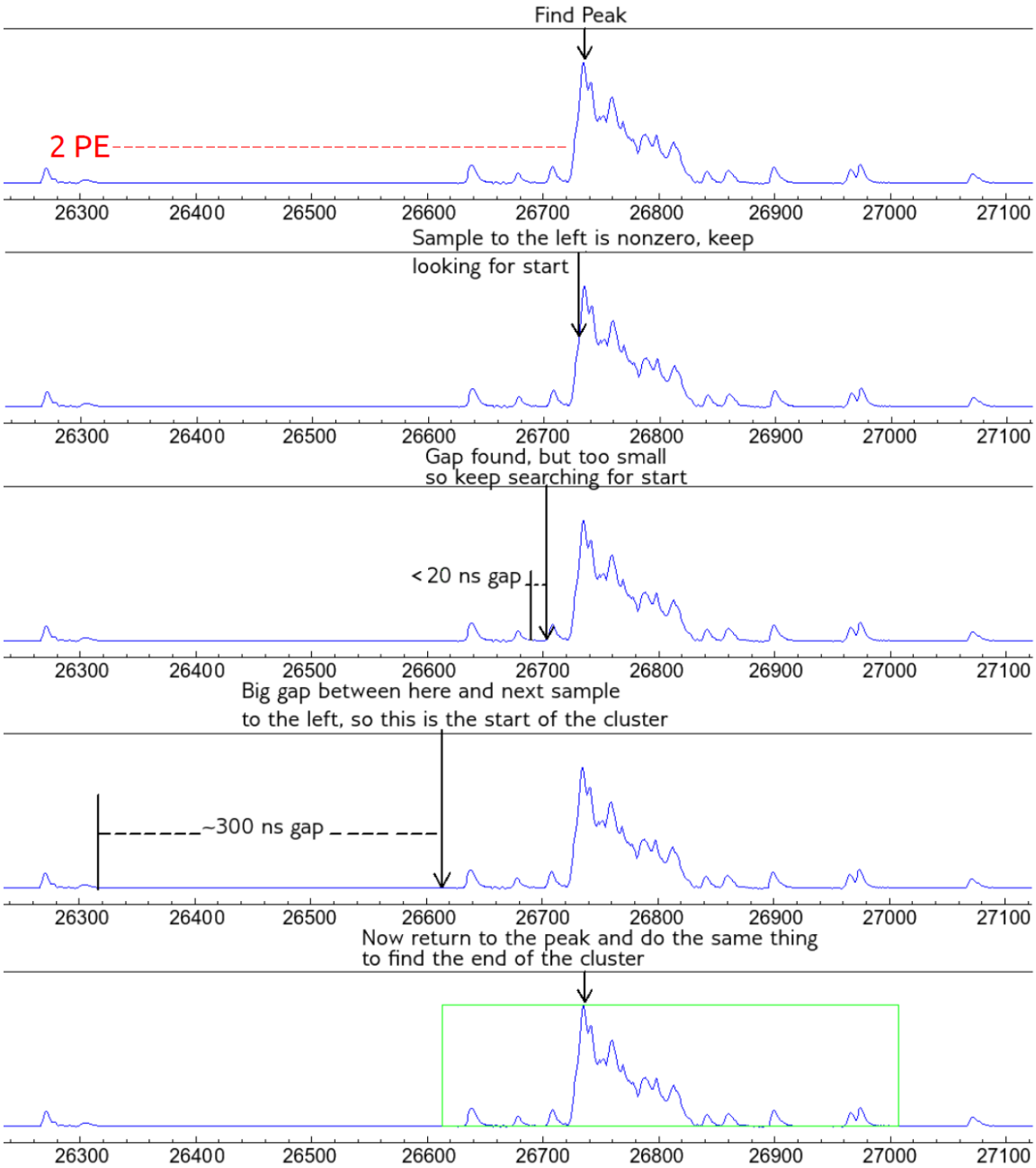

Figure 2.14: Example of a waveform in the NV with its corresponding cluster. The variable in the horizontal axis is the time in ns with respect to the trigger (Figure from Ref. [51]).

Chapter 3

Gamma Background

Although DarkSide-50 is designed to detect WIMP signals, there are still other sources of background that leave signals in the detector even after the dedicated effort taken to screen and select materials. One of the dominant backgrounds is from γ-rays, which interact with electrons. ER can be identified by PSD and well separated from WIMP signals. Some of the γ-rays with high energy can travel through both the TPC and outer detectors, which provides a good method to calibrate both detectors. For instance, γ-rays can be used to trigger the veto detector and test the long term stability of the detector. As γ-rays appear in the detector, it is useful to monitor the performance of the detector by keeping track of time, charge, and other parameters. We developed veto cuts to identify γ-rays, allowing us to understand the response to γ-ray sources, and extract useful physics parameters for future experiments.

3.1 Radioactive γ Sources

γ-rays usually come from the decays of excited atomic nuclei from a high energy state to a lower energy state, emitting photons with energies ranging from 100 keV to 10 MeV. A γ-ray can interact with other matter through three processes: the photoelectric effect, Compton scattering, and pair production. The photoelectric

effect occurs when a photon knocks an electron out of an atom. The energy of the incident photon must be large enough to overcome the electron binding energy of the atom. The rest of the energy is transferred as the kinetic energy of the resulting photoelectron. The cross section of the process is proportional to Z^n/E^3, where E is the energy of the incident photon, Z is the atomic number, and n is a number that varies between 4 and 5. Based on this relation, the photoelectric effect dominates for low energy photon and heavy atoms.

In Compton scattering, a γ-ray interacts with a free or weakly bound electron with parts of its energy transferred to the electron. The kinetic energy of the free electron, in Equation 3.1, is equal to the energy lost by the γ-ray,

$$E_e = E_\gamma - E', \tag{3.1}$$

where E_e is the energy of the scattered electron, E_γ is the energy of the incident γ-ray, and E' is the energy of the scattered γ-ray. The directions of the electron and scattered γ-ray depend on the amount of energy lost to the electron during the interaction, as in:

$$E' = \frac{m_o c^2}{1 - \cos\phi + m_o c^2/E}, \tag{3.2}$$

$$E'(\text{min}) = \frac{m_o c^2}{2 + m_o c^2/E}, \tag{3.3}$$

$$E_e(\text{max}) = \frac{E}{1 + m_o c^2/2E}. \tag{3.4}$$

where $m_o c^2$ (511 keV) is the energy of the rest electron and ϕ is the angle between the incident and scattered γ-ray. When ϕ is 180°, the scattered γ-ray moves backwards and the electron moves forward, in the direction of the incident γ-ray, therefore the energy of the electron reaches the maximum value which is known as the Compton edge. The Compton scattering produces a continuous spectrum from zero up to the

Compton edge. Since the process involves weakly bound electrons, the impact to the nucleus is relatively small. The cross section is proportional to Z/A, which only changes slightly with respect to the energy of the incident γ-ray.

As the energy of a γ-ray reaches 1.022 MeV, it is possible to produce an electron-positron pair with the presence of strong electromagnetic field in the vicinity of a nucleus. This process is called pair production. The energy of the incident γ-ray in excess of 1.022 MeV becomes the kinetic energy of the resulting electron and positron, which slow down rapidly in the medium. The positron combines with an electron in an annihilation process emitting two γ-rays with 511 keV energy each. The cross section of pair production is proportional to Z^2 [57]. Therefore, pair production is more important in high atomic number elements.

The γ-rays are present in the detector mainly due to the contamination of the detector components. Non-negligible radioactive components appear either in their material or on their surface as a result of exposure to air. Since most of these materials are close to the detector medium with little or even no shielding, they become a crucial background source in the experiment, even if the absolute contamination level is low. Based on the material counting results in DarkSide-50, there is a comprehensive list of potential radioactive γ-ray sources in different parts of the detector, which include the stainless steel of the cryostat, borosilicate glass of the TPC PMTs and some traces in the TPC and NV. Some of the γ-rays play a big role in measuring the parameters of the detector, such as light yield and acceptance loss of the veto cuts. In my dissertation, I will focus on the γ-rays from ^{60}Co and the β-decay from ^{14}C, which leave a big impact on the detector and its performance.

3.1.1 ^{60}Co

^{60}Co is a synthetic radioactive isotope of cobalt with a half-life of 5.2714 yr. It is produced artificially in nuclear reactors or industrial production by bombarding a

^{59}Co target with a slow neutron source. Due to the production process, ^{60}Co is present in the stainless steel. In DarkSide-50, the trace of ^{60}Co is found in the cryostat of the TPC and NV. ^{60}Co decays to ^{60}Ni by β-decay. The excited and unstable ^{60}Ni nucleus emits two γ-rays with energies of 1.17 MeV and 1.33 MeV as in the decay scheme detailed in Equation 3.5. The two high energy γ-rays are produced by de-excitations from two different angular momentum levels so that their momenta are totally uncorrelated, though they are produced almost simultaneously. Their time correlation plays a big role in DarkSide-50 because it is likely that one of the γ-rays goes into the TPC while the other scatters in the NV, as shown in Figure 3.1.

$$^{60}\mathrm{Co} \longrightarrow {}^{60}\mathrm{Ni} + e^{-} + \bar{\nu}_{\mathrm{e}} + 2\,\gamma. \tag{3.5}$$

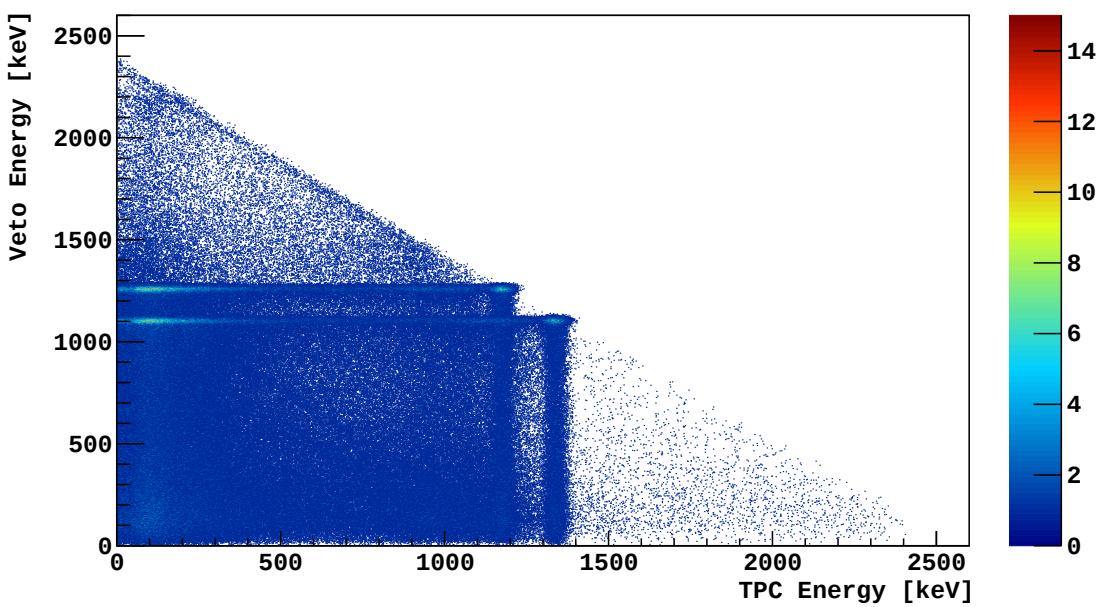

Figure 3.1: Two correlatedγ-rays from ^{60}Co decay detected in a 250 ns window in the TPC and NV of DarkSide-50.

Because it is a high intensity γ-ray emitter with a relatively long life time, ^{60}Co is more favorable than other γ-ray sources in industrial applications. ^{60}Co is widely

used in medical radiotherapy to treat cancer, food irradiation as well as many other fields. However, a large dose and long exposure to ^{60}Co source causes some safety issues. Since ^{60}Co can be taken up by tissue, like the liver, kidneys, and bones after entering the human body, a prolonged exposure can cause cancer. In manufacturing, uncontrolled disposal of ^{60}Co in scrap metal is responsible for the radioactivity found in several iron-based products [58].

3.1.2 ^{14}C

The isotope discussed above involves the emission of γ-rays during the decay process. In contrast, ^{14}C does not produce any γ-rays when it decays, but it emits a β particle, which generates an important signal because it resides in the organic liquid scintillator in the NV. Small traces of the ^{14}C decay can leave significant background signals in the NV. Carbon is the 15th most abundant element in the Earth's crust and the 4th most abundant element in the Universe by mass after hydrogen, helium and oxygen. The large abundance, its unique diversity of organic compounds as well as the ability to form polymers make carbon a common, essential element of all known life. ^{14}C makes up 1 atom per 10^{12} atoms of the carbon in the atmosphere with a half-life of 5700 yr [59].

Most of ^{14}C is produced in the upper layers of the troposphere and the stratosphere by thermal neutrons absorbed by nitrogen atoms in the following reaction:

$$n + {}^{14}\mathrm{N} \longrightarrow {}^{14}\mathrm{C} + p. \tag{3.6}$$

Besides this, ^{14}C can also be produced by other neutron reactions, in particular ^{13}C(n,γ)^{14}C and ^{17}O(n,α)^{14}C with thermal neutrons, as well as ^{15}N(n,d)^{14}C and ^{16}O(n,^{3}He)^{14}C with fast neutrons [59]. The most notable ways of ^{14}C production by thermal neutron irradiation of targets are summarized in the Table 3.1.

Table 3.1: Cross section for producing ^{14}C.

Parent Isotope	**Natural abundance** [%]	**Cross Section** [b]	**Reaction**
^{14}N	99.634	1.81	^{14}N$(n,p)^{14}$C
^{13}C	1.103	0.0009	^{13}C$(n,\gamma)^{14}$C
^{17}O	0.0383	0.235	^{17}O$(n,\alpha)^{14}$C

^{14}C goes through β decay to ^{14}N as follows:

$$^{14}\mathrm{C} \longrightarrow {}^{14}\mathrm{N} + e^- + \bar{\nu}_\mathrm{e}. \tag{3.7}$$

The emitted electron has a maximum energy of 156.475 keV with a mean energy of 49.47 keV. ^{14}C is used in radiocarbon dating to determine the age of carbonaceous materials up to about 60000 years old. One of the widely known applications of the technique is to date organic residuals from archaeological sites. Plants fix atmospheric carbon during photosynthesis, so the level of ^{14}C in plants and animals when they die approximately equals the level of ^{14}C in the atmosphere at that time. However, it decreases thereafter due to radioactive decay, allowing the date of death or fixation to be estimated [49].

In DarkSide-50, the NV is filled with organic liquid scintillator. Since the energy of the β decay from ^{14}C is relatively low, the decay events reside in the lower part of the charge spectrum. This signal was dominant in the first stage of the experiment when the NV was filled with 50 % mass fraction of PC, 50 % TMB and 2.5 g L^{-1} PPO. The plant in the Netherlands used biogenic methanol instead of methanol from petroleum to produce the TMB used in DarkSide-50. Since the carbon in biogenic methanol is mostly from the atmosphere, there is a very high ^{14}C concentration in the TMB. A high rate (160.6 ± 1.3 kBq) of ^{14}C decay signal was found by fitting the charge spectrum. Once this problem was fully diagnosed, the scintillator was extracted from the detector. The TMB was then produced with methanol from petroleum, which was

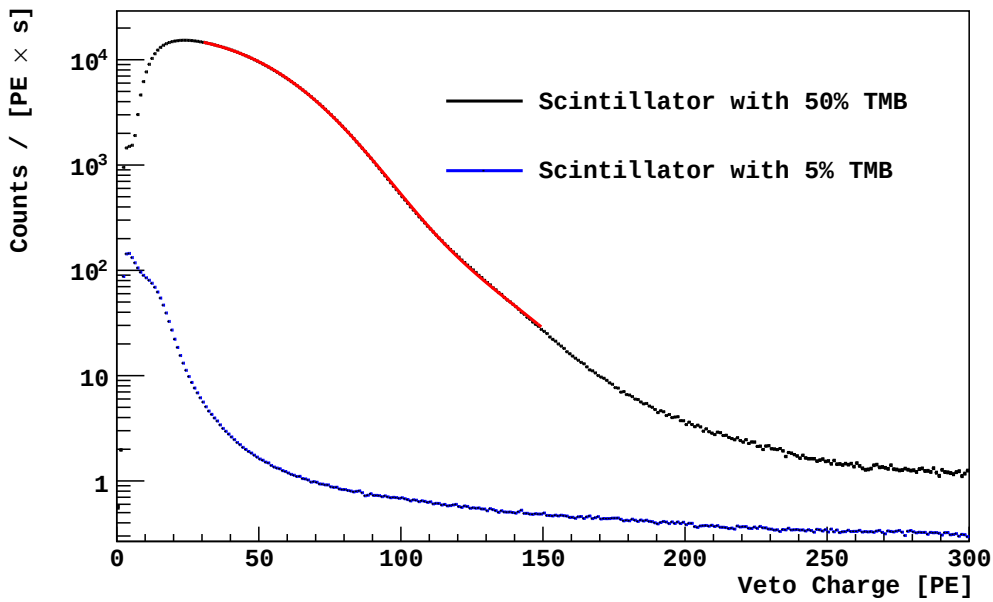

Figure 3.2: Comparison of cluster charge in the NV. The scintillator with 50% TMB (black) contains ^{14}C with a rate of (160.6 ± 1.3) kBq calculated by a MC fit (red). After replacement, the ^{14}C rate is highly reduced to be (0.25 ± 0.03) kBq in the scintillator with 5% TMB (blue).

shielded from cosmic rays for millions of years underground. The ratio of ^{14}C to ^{12}C in petroleum was measured to be $\sim 2 \times 10^{-18}$. After the replacement, the scintillator in the NV became 95 % mass fraction of PC, 5 % TMB and 1.4 g L^{-1} PPO, which highly reduced the background from ^{14}C decay to the level of 0.25 ± 0.03 kBq, as seen in Figure 3.2.

3.2 Stability of NV Detector

The γ-rays in the UAr data can be used to check the performance of the detector. In a long-term program, the status of the detector needs to be stable. To check that, it is important to track information for each run and compare the results from different runs. For the validation in the NV, the veto cluster charge, time, channel rate, and the number of veto clusters per trigger for each single run are monitored.

When studying stability for a long-term system, it is important to conduct a time series analysis. Figure 3.3 clearly shows that the event rate is not a flat curve due to different operations and configurations. At run 13420, the event rate dropped to 1.4 Hz when the high voltage turned off and data were taken in a null field configuration. Occasionally, the event rate increased significantly for one or two runs due to the instability of TPC PMT 18. When this situation occurred, all the PMTs in the detector were shut down for one or two days so that the rate of fake events induced by TPC PMT 18 dropped. From run 16300 to 16487, the event rate (mainly the rate of bipolar event) decreased again because the radon abatement system was turned off for replacement. The bipolar event is caused by the discharge in the High High Voltage power supply. Without radon abatement system, more humid air flows into the clean room of DarkSide-50 detector, in which the High High Voltage power supply is located. The humid air keeps the charge from accumulating and then leads to less discharge process, which decreases the rate of the bipolar event. In some regions of the plot, there are gaps due to calibration campaigns, like Kr or a neutron source calibration. Despite these extra features in the event rate plot, the detector system is stable overall.

In the NV, the data acquisition window is divided into three sub-regions with respect to the TPC trigger time. A well defined and stable TPC trigger time is very important for the analysis of the cuts associated with time windows. The TPC trigger time is monitored by the time distribution of the cluster time in the NV. Figure 3.4 shows the TPC trigger time is stable at -6584 ns all the time. In the SLAD program discussed in Section 2.3.2, the TPC trigger time is used to match the TPC and NV events. The time in the SLAD output file that is ready for data analysis is shifted by the TPC trigger time, which makes the TPC trigger time as time 0. Then the veto prompt window is in the time region [-50 ns, 250 ns]. The veto pre-prompt window

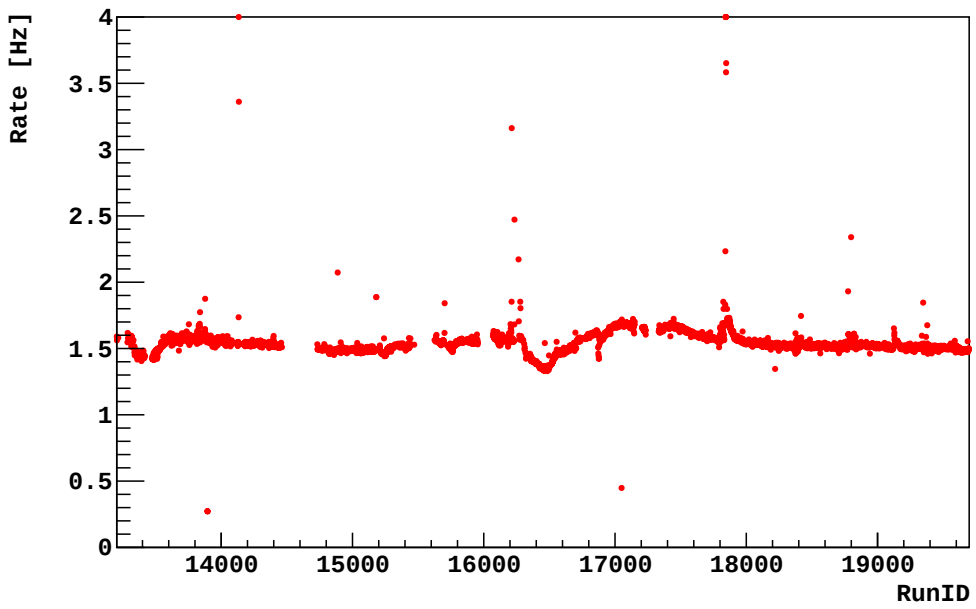

Figure 3.3: Event rate of DarkSide-50 in 500-days UAr data with x-axis as the `runID`.

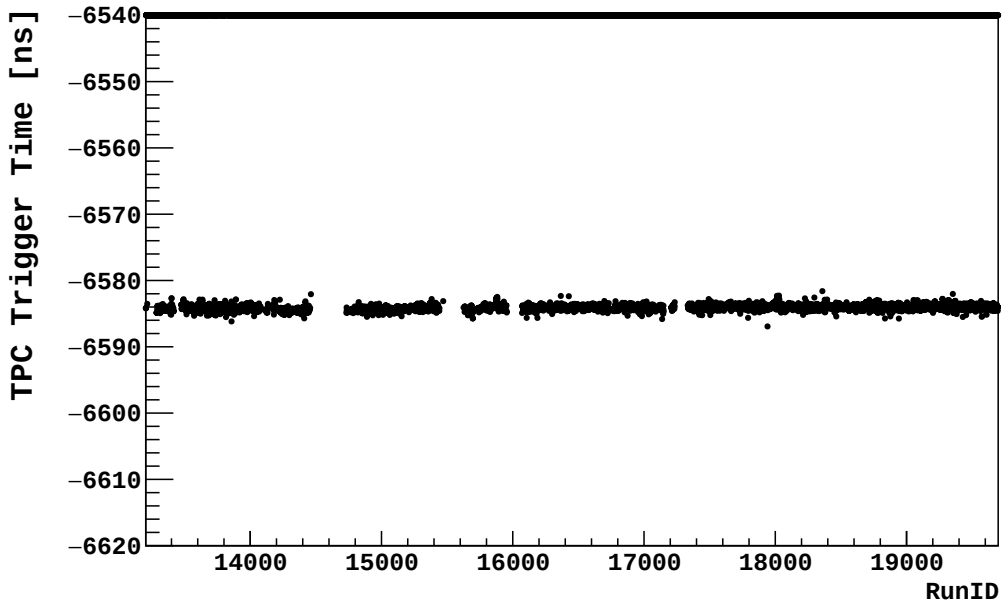

Figure 3.4: Distribution of TPC trigger time.

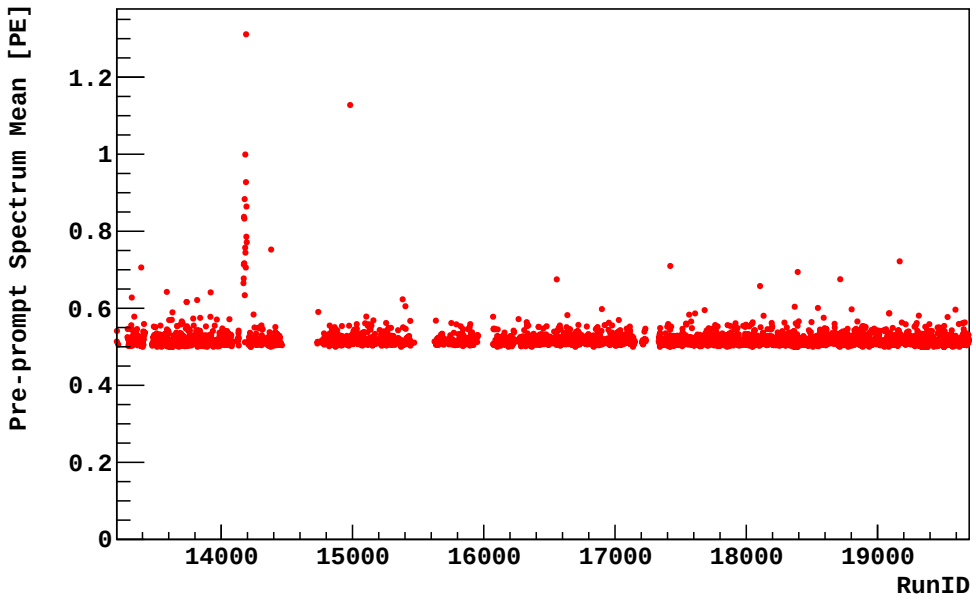

Figure 3.5: Mean of the `Slider` charge in the pre-prompt window of NV.

is from the beginning of the data acquisition window ($-10\,\mu s$) to 0. The delayed window starts from time 0 to the end of the data acquisition window ($210\,\mu s$).

In general, the pre-prompt window should be empty. However, due to cosmic rays or other high energy events triggering the TPC, there are events in the pre-prompt window. The plots of the charge spectrum in the pre-prompt window can help us check if there are these backgrounds. Figure 3.5 shows the distribution of the mean of the `Slider` charge in the pre-prompt window across each run. Overall, the mean is stabilized at 0.5 PE, which indicates no strong background sources in the NV or that most of the particles lost their energy in the MV. However, there are some present in some regions. For instance, from run 14171 to 14194, the mean spiked. During that time, the voltage supply at TPC PMT 18 dropped from 1145 V to 1125 V. However, it is unknown if the TPC PMT 18 actually causes the change of `Slider` charge in the pre-prompt window.

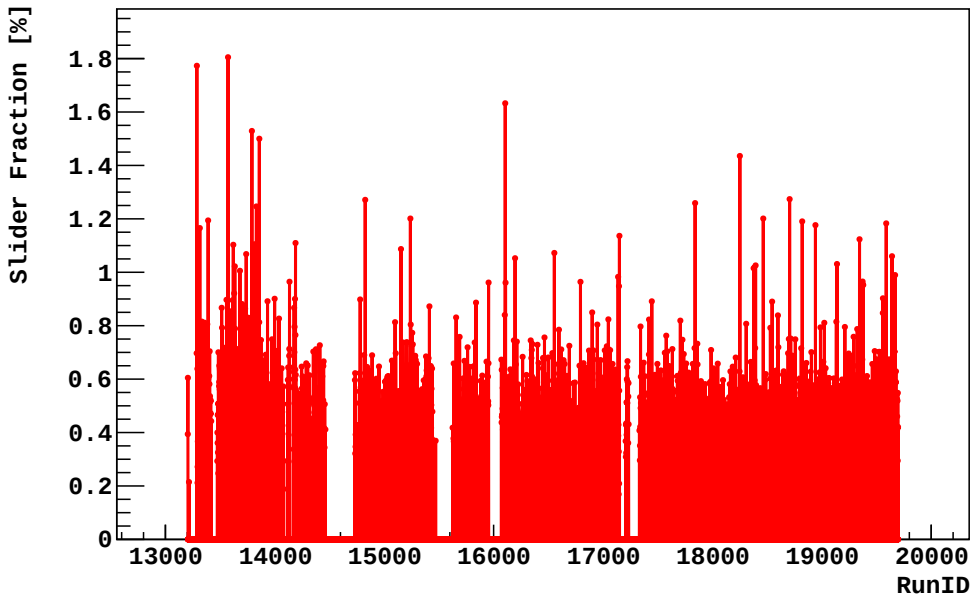

Figure 3.6: The fraction of the `Slider` charge, larger than 1 PE, in the pre-prompt window of NV.

In the pre-prompt window, a veto cut is set with the pre-prompt `Slider` charge less than 3 PE, which is discussed in more details in Section 3.3. As shown in Figure 3.5, the mean of the `Slider` charge is around 0.5 PE, much lower than the threshold of the veto pre-prompt cut, so the expected fraction of events with pre-prompt `Slider` charge larger than 3 PE should be very small. That is consistent with the results shown in Figure 3.6, in which the fraction of those events is less than 1 % overall. This further demonstrates the stability of the detector in the pre-prompt window.

The prompt window is used to check for the TPC coincident events possibility induced by neutron thermalization and γ-rays. In the prompt window, a veto cut is set with prompt `ROI` charge less than 1 PE, which is explained in Section 3.3. As shown in Figure 3.7, the cluster charge in the prompt window appears in a broad range. However, the fraction of the events with prompt `ROI` charge larger than 1 PE due to γ-rays generated within the detector materials is not very large ($\sim$25 %), as

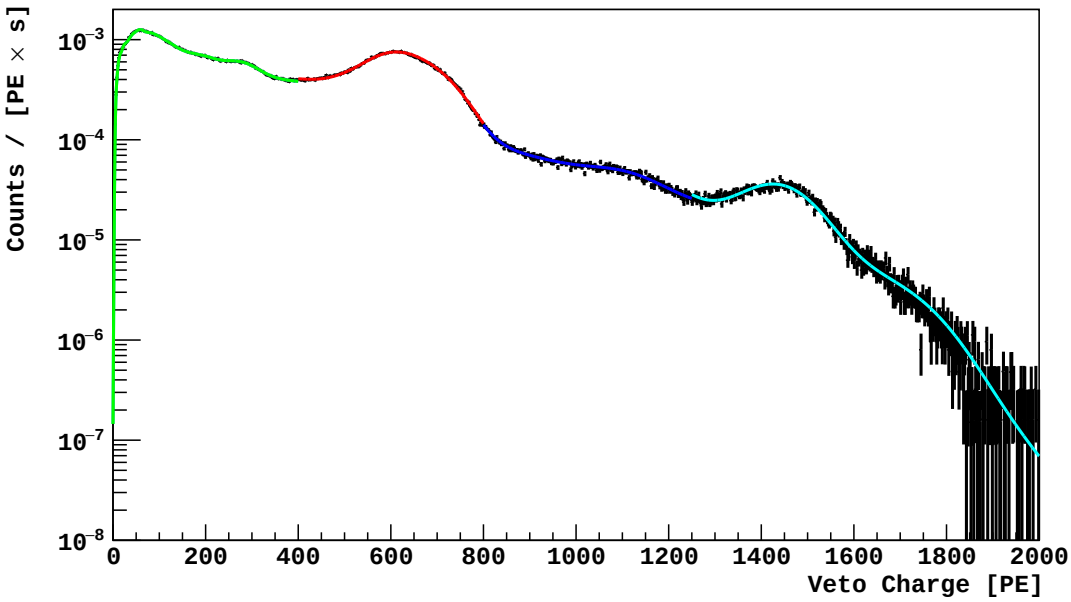

Figure 3.7: Cluster charge spectrum from 500-days UAr data fitted by different radioactive sources in the prompt window of the NV. The green and blue part is contributed by multiple low intensity radioactive sources. The red part is dominated by γ-rays from ^{60}Co decay. The teal part is from γ-rays generated by ^{232}Th decay.

shown in Figure 3.9. This fraction is very stable across runs, which indicates the stability of the detector in the prompt window.

One of the most important features of the NV is the neutron veto efficiency, which requires stable performance of the PMTs installed in the NV. In addition, the light yield of the NV must be stable. This parameter can be monitored by measuring γ-rays peaks in the prompt window from ^{60}Co that resides in the cryostat of the TPC and NV, which is one of the main radioactive backgrounds in the NV. Figure 3.8 is a 2D distribution of veto cluster charge vs `runID`, which is expected to have similar structures for each run. For the cluster charge from 600 PE to 800 PE, it is dominated by the two γ-rays from ^{60}Co decay that are indistinguishable due to the limited energy resolution in the NV. In Figure 3.8, a red dot is drawn for each run representing the mean of this peak calculated by fitting a gaussian distribution function to that energy range for every run. The horizontal, linear distribution of the mean value indicates

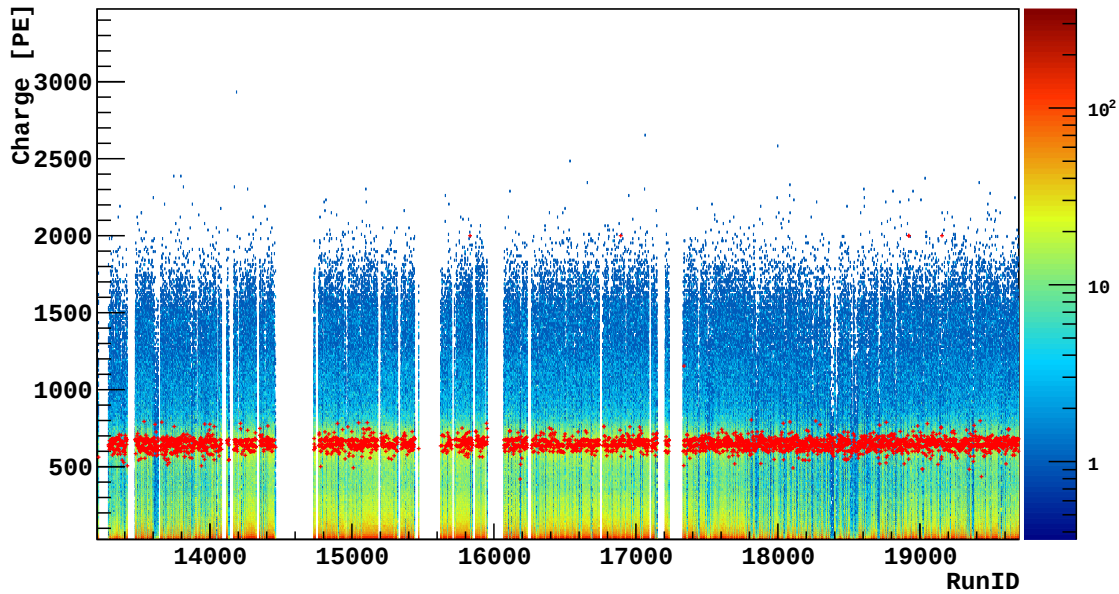

Figure 3.8: Cluster charge over `RunID` from 500-days UAr data in the prompt window of the NV. The charge distribution from each `RunID` has the same spectrum as the plot in Figure 3.7. The veto charges below 600 PE and from 800 PE to 1200 PE are contributed by multiple low intensity radioactive sources. The red dot, calculated by fitting a gaussian distribution function in each run, is the mean of the peak of γ-rays from ^{60}Co that dominates the cluster charge distribution from 600 PE to 800 PE. The high veto charge part ($>$ 1200 PE) is contributed by γ-rays generated from ^{232}Th decay. The color in logscale indicates different population of events. The red and yellow means more events while blue indicates less events.

the stability of the light yield. In addition to ^{60}Co, there are other sources of γ-rays, like ^{40}K, ^{235}U, ^{238}U, and ^{232}Th. They contribute to different energy regions in the charge spectrum in Figure 3.7. For instance, the ^{232}Th decay emits 2.614 MeV γ-ray that contributes to the peak around 1400 PE.

However, there are some extra components that contribute to the higher energy range (>2000 PE) in a fraction of runs. This abnormal behavior in the NV results from the noise of three channels in the NV that have extremely high frequency. The noise triggers the data acquisition system of the NV and, in most cases, lasts an entire run. In a small fraction of the affected runs, the noise appears in the middle of the run. Since the amplitude of this noise is much larger than the threshold in the

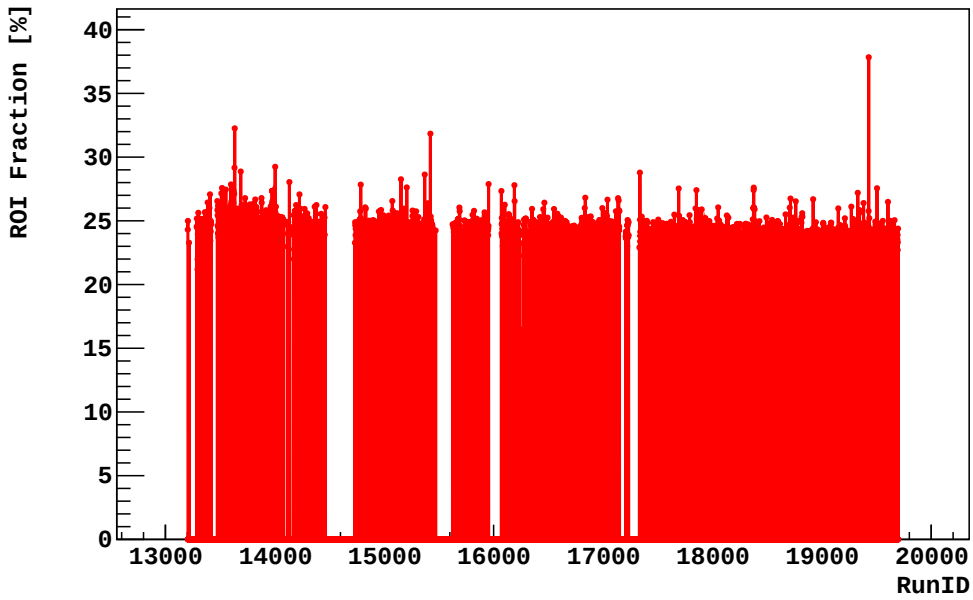

Figure 3.9: Fraction of the ROI charge, larger than 1 PE, in the prompt window of the NV.

electronics system, they are not removed by the zero-suppression algorithm. With all the noise recorded, the Data AcQuisition (DAQ) system of the NV crashed frequently during those runs due to the high memory usage. The pulse-finder algorithm in the NV takes them as one cluster in each event because the noise starts very early in time and lasts the whole data acquisition window. The length of a single cluster increases to 220 µs, which is the entire data acquisition window in the NV. Because the algorithm integrates all the pulses in each cluster, the cluster charge increases dramatically, as shown in some runs from 15000 to 16000 in Figure 3.10.

The sine-like waveforms from three noisy NV channels overlap over time, as shown in Figure 3.11. The noise also affects, but not as severely as those three, four other channels by periodically generating noise. According to the generated waveforms, the rest of the NV channels still work as normal. A probe into the DAQ system in the NV at LNGS lab shows that these affected channels are all connected into the same Front-End-Board (FEB). It is likely that the noise occurs in one channel and others

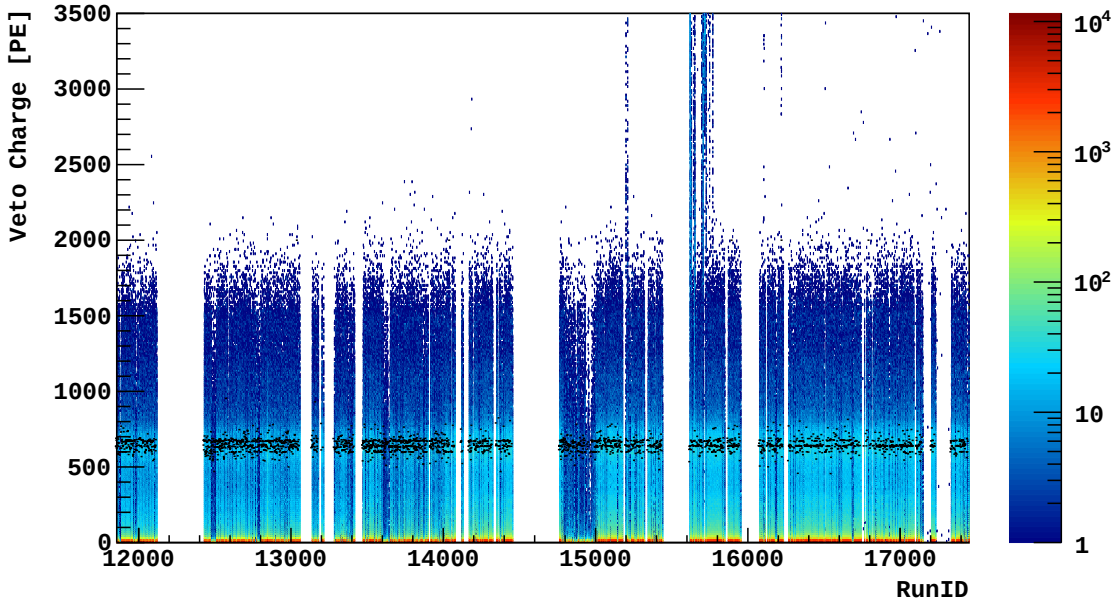

Figure 3.10: Cluster charge over `RunID` including runs affected by noise in the NV. The veto charges below 600 PE and from 800 PE to 1200 PE are contributed by multiple low intensity radioactive sources. The black dot, calculated by fitting a gaussian distribution function in each run, is the mean of the peak of γ-rays from ^{60}Co that dominates the cluster charge distribution from 600 PE to 800 PE. The region with veto charge from 1200 PE to 2000 PE is due to γ-rays generated by ^{232}Th decay. The veto noise leads to the veto charge larger than 2000 PE. The color in logscale indicates different population of events. The red and yellow means more events while blue indicates less events.

are affected through the FEB. After a deep look at the channels connected to the same FEB, the waveforms turn out to be distorted even if the main structure looks good, as shown in Figure 3.12. However, the waveforms in the noisy channels are completely immersed in the noise.

This noise started around March 11, 2016, without any clear reason. When this problem happened, only a few events in a single run were affected by this noise while most of the events were fine. Later on, the noise appeared in the middle of a run then gradually occupied the whole data acquisition window. The same pattern appeared in the following runs. In some cases, the noise could also disappear in a single run. For those runs, the beginning and the end of the run were normal while the middle part

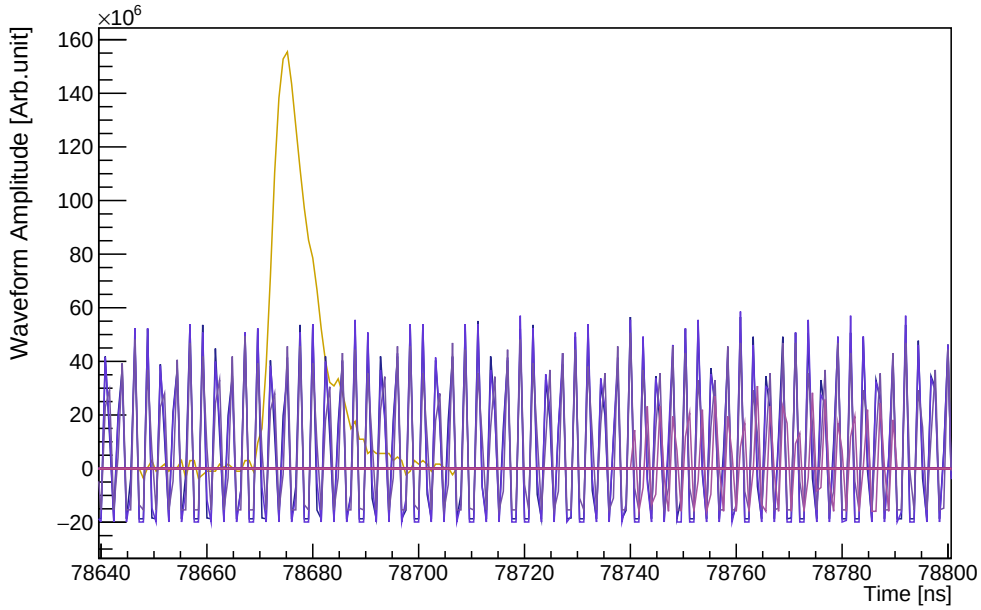

Figure 3.11: Example of the zoomed waveforms of the NV channels. The noise was from 3 channels while the rest channels were working fine.

was noisy. This behavior was seen in most of the noisy runs. As the problem became worse, the noise usually appeared in the entire run and lasted a few days before it disappeared. Unfortunately, before we realized this problem, the situation became much worse. The noise affected a big fraction of the data taken in September and October of 2016, which in total lead to a loss of life-time of ∼32.6 d. Since the problem came from the FEB that connected three noisy NV channels, we disconnected one of three channels. After that, the waveforms of the NV channels went back to normal. The NV has been stable and normal since then.

3.3 Cuts in the NV

As there are signals from all kinds of background sources, it is important to figure out an effective method to label and reject those signals. In some cases, the signals are important for studying the response of the detector to external radioactive sources, for

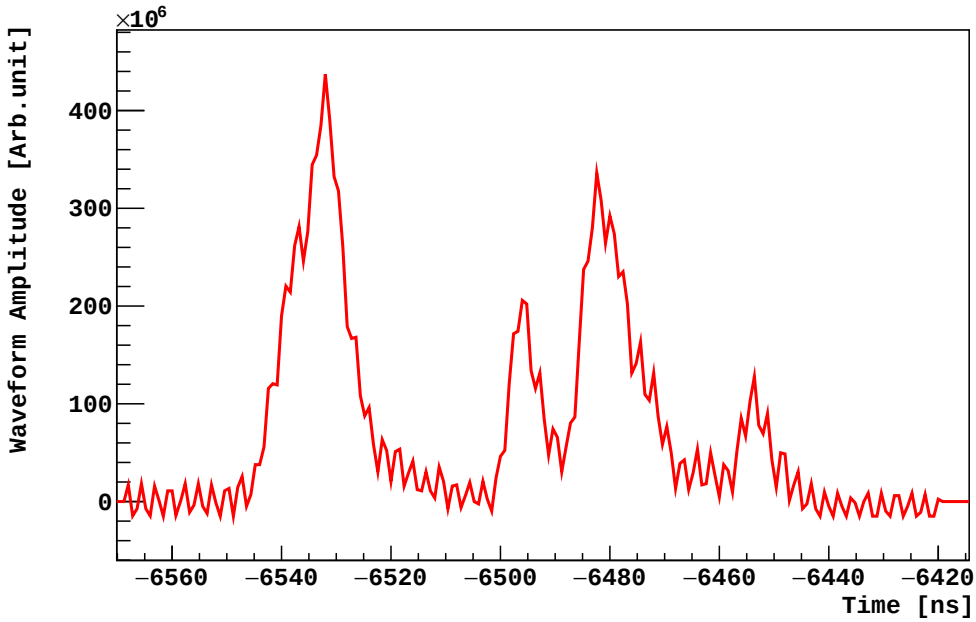

Figure 3.12: Example of distorted zoomed waveform from channel 103.

instance the neutron source calibration data can produce similar signals to WIMPs. So the criteria for the event selection should not be so weak that the background signals are still left and mixed with interesting signals. It should also not be so strong that it rejects the interesting signals even if the backgrounds are completely rejected. In order to effectively reject the background, a moderate acceptance loss of the event cuts is one of the main concerns.

For each window in the NV, there is one specific veto cut designed to reject the background signals. In addition, the muon cut is designed to remove muon and cosmogenic background by checking the total cluster charge in the NV and MV. The cosmogenic cut aims at the cosmogenic neutrons that have a long delay time. This cut requires a full FLUKA MC simulation to fully understand the efficiency.

First, the veto prompt cut is developed to remove events that have prompt coincidence, which mostly come from neutron thermalization and γ rays. It uses an `ROI` variable with a window between -50 ns and 250 ns relative to the TPC trigger time.

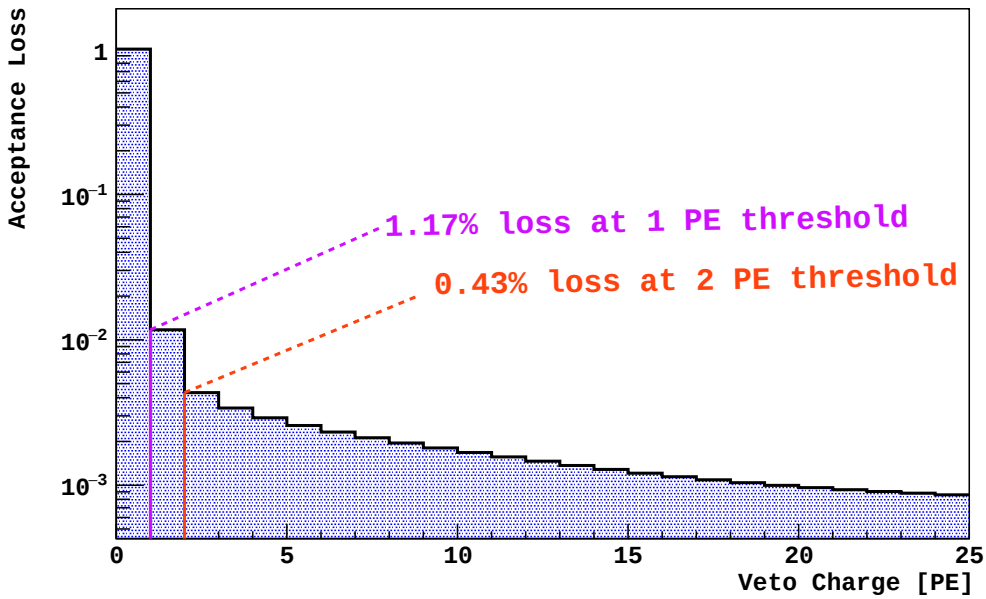

Figure 3.13: Acceptance loss of the veto prompt cut calculated using UAr data.

If the charge in this `ROI` exceeds 1 PE, the event is seen by the NV as a neutron background event so it will be vetoed. The acceptance loss of this cut is the probability that a random background in the veto accidentally vetoes a TPC event without any real prompt signal. In order to get the acceptance loss of this cut, another `ROI` with a 300 ns window is defined 2 µs before the TPC trigger time. The rate of vetoing a TPC coincident event can be calculated by assuming every signal is from background. As seen in Figure 3.13, the acceptance loss of the veto prompt cut at 1 PE threshold is 1.17 %.

Second, the veto delayed cut tags neutron background by checking whether the neutron gets captured in the liquid scintillator. It defines a `Slider` window, with a `Slider` length of 500 ns, starting from the TPC trigger time to the end of the acquisition window. As the data acquisition window extended from 140 µs to 220 µs, the threshold of the veto delayed cut was increased from 3 PE to 6 PE to keep the same acceptance loss. Once the `Slider` charge of an event is larger than the threshold, it

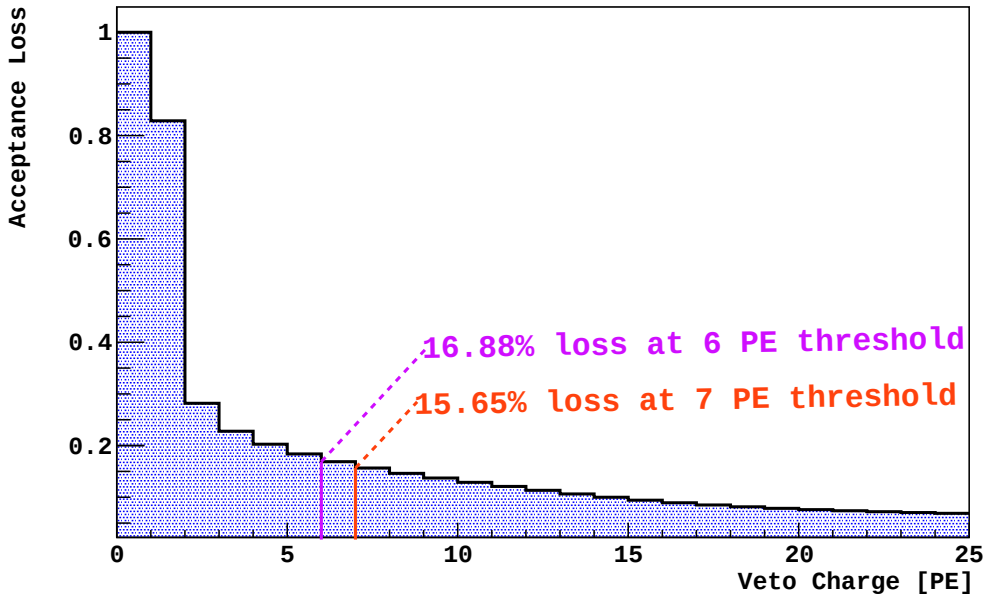

Figure 3.14: Acceptance loss of the veto delayed cut calculated using UAr data.

is believed to be a neutron capture signal and therefore rejected by the veto delayed cut. The acceptance loss of this cut is the probability that a random background creates a signal that looks like a delayed signal above a threshold. In order to get the acceptance loss of this cut, all the events that pass the veto prompt cut are assumed to only have random background. As shown in Figure 3.14, the acceptance loss of the veto delayed cut is 16.88 % at a threshold of 6 PE when the data acquisition is 140 µs. As the data acquisition increases to 220 µs, the acceptance loss of the veto delayed cut is 15.6 % at a threshold of 3 PE.

Third, the veto pre-prompt cut is designed to reject events induced by external neutrons and γ-rays that happen before the TPC Trigger time. It uses another `Slider` variable, with a length of 500 ns, scanning all the time before the TPC trigger time. It vetoes the events if the corresponding `Slider` charge exceeds 3 PE. The acceptance loss of this cut is the probability that a random background creates a signal above 3 PE before the TPC trigger time. In order to get the acceptance loss

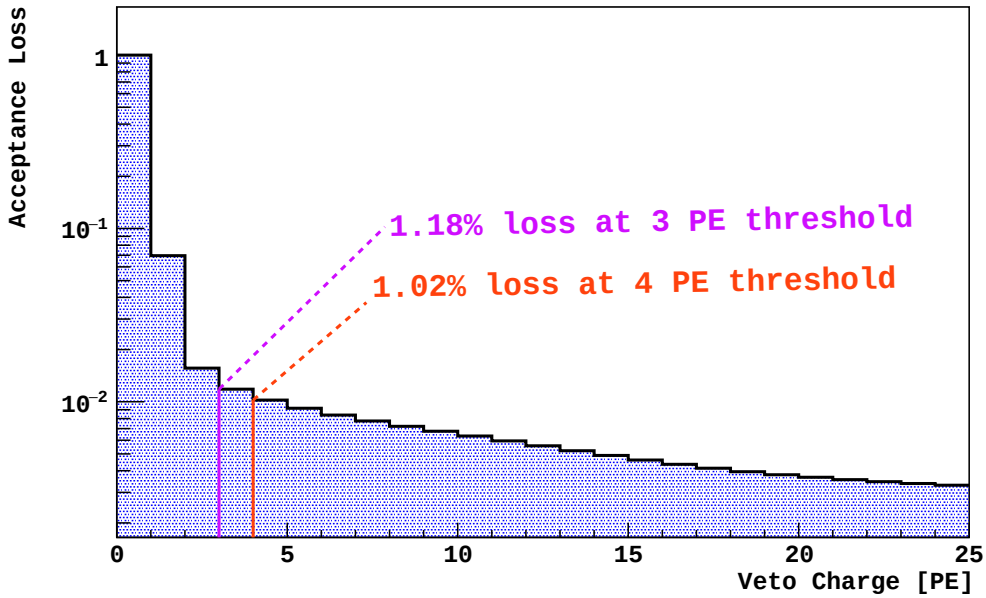

Figure 3.15: Acceptance loss of the veto pre-prompt cut calculated using UAr data.

of this cut, all the events that pass the veto prompt cut are assumed to only have random background. The acceptance loss of the veto pre-prompt cut is 1.18 % at a threshold of 3 PE as shown in Figure 3.15.

The muon cut is designed to remove signals associated with a muon passing through the NV or MV. When either the total NV charge exceeds 2000 PE or the total MV charge is larger than 400 PE, the event is rejected. By calculating the fraction of events that the detector loses when applying this cut, it is easy to set an upper limit on the acceptance loss. In Figure 3.16, the acceptance loss from the NV total charge is 0.53 % at a threshold of 2000 PE while that from the MV total charge is 0.03 % at a threshold of 400 PE.

With the well tuned cuts in the NV, it is easy to reject the background events without compromising the efficiency. All the veto cuts have been tested and used through the DarkSide-50 data analysis. In the next section, the efficiency of the veto

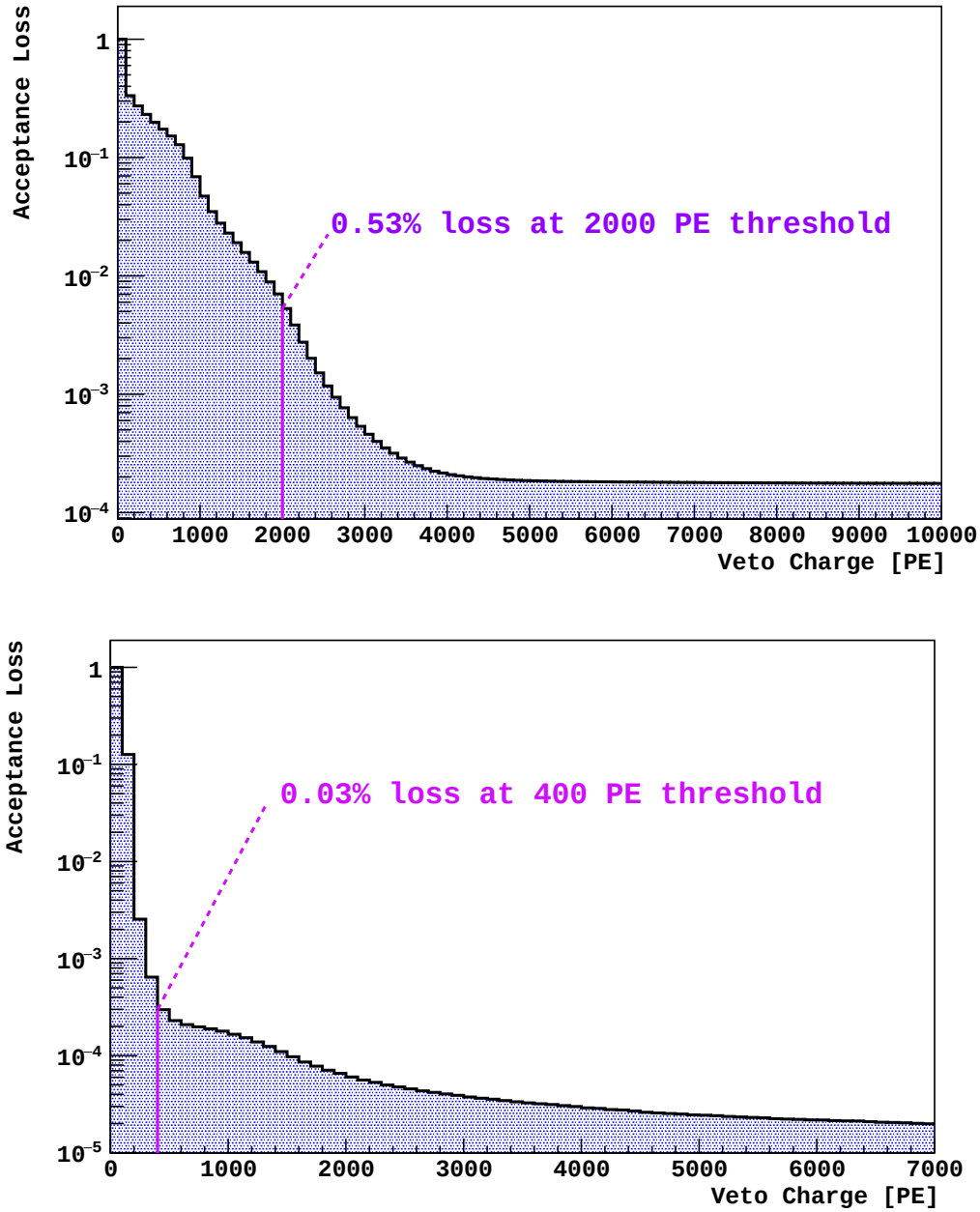

Figure 3.16: Top: Acceptance loss of the muon cut based on the total cluster charge in the NV. Bottom: Acceptance loss of the muon cut based on the total cluster charge in the MV.

cuts will be calculated based on the neutron calibration data and radiogenic neutron background simulation.

Chapter 4

Neutron Calibration

The main goal of the DarkSide-50 NV is to veto neutron events registered in coincidence between the TPC and NV. The boron-loaded organic liquid scintillator in the NV can detect the prompt coincidence signals coming from neutron thermalization after a neutron leaves the TPC, as well as the delayed signal caused by neutron capture reaction with ^{10}B, ^{1}H, and ^{12}C. The capability of the NV to remove these neutron backgrounds requires a very high neutron veto efficiency.

In order to quantify the response of the NV to neutron signals, neutron source calibration campaigns were conducted. In one of the campaigns the collaboration deployed a Americium-Beryllium (^{241}Am^{9}Be) source and in the other one a Americium-Carbon (^{241}Am^{13}C) source. For each neutron calibration, there were different configurations, varying positions of the deployed source and changes of liquid scintillator components, to systematically measure the response of the NV. Based on the results from comprehensive data analysis, parameters and models were tuned in the Monte Carlo (MC). With the more accurate and reliable MC data, the neutron veto efficiency along with expected surviving neutron background events were calculated, as reported later in my dissertation.

4.1 ^{241}Am^{9}Be Source Calibration

^{241}Am^{9}Be (α,n) sources are mainly used for activation analysis and calibration sources. It's relatively cheap, compact, portable, and reasonably constant due to its long half-life. The source is a compressed mixture of americium power and beryllium powder. Safety caution is especially taken into consideration during the processing and assembling of the neutron source in order to avoid radioactive hazard.

4.1.1 ^{241}Am^{9}Be Neutron Energy

The emission of a neutron in the ^{241}Am^{9}Be source starts from the α decay of ^{241}Am. ^{241}Am is the most common isotope of americium with a half-life of 432.2 yr. It is commonly used in ionization type smoke detectors. ^{241}Am comes from plutonium which is synthesized from uranium according to the following nuclear process:

$$^{238}_{92}\mathrm{U} \xrightarrow{(n,\gamma)} {}^{239}_{92}\mathrm{U} \xrightarrow[23.5\,\mathrm{min}]{\beta^-} {}^{239}_{93}\mathrm{Np} \xrightarrow[2.3565\,\mathrm{d}]{\beta^-} {}^{239}_{94}\mathrm{Pu}, \tag{4.1}$$

Then the capture of two neutrons by ^{239}Pu followed by a β-decay results in ^{241}Am:

$$^{239}_{94}\mathrm{Pu} \xrightarrow{2(n,\gamma)} {}^{241}_{94}\mathrm{Pu} \xrightarrow[14.35\,\mathrm{yr}]{\beta^-} {}^{241}_{95}\mathrm{Am}, \tag{4.2}$$

then ^{241}Am decays to ^{237}Np with the emission of α particles accompanying with weak γ-rays [60].

$$^{241}\mathrm{Am} \longrightarrow {}^{237}\mathrm{Np} + {}^{4}\mathrm{He} + \gamma. \tag{4.3}$$

There are three main α-decay modes. 84.8 % of the time a 5.485 MeV α is produced. This dominant branch of α is accompanied by a 59.54 keV X-ray 94 % of the time. The second most important branch produces a 5.443 MeV α with a probability of 13.1 %. This α is accompanied with a set of X- and γ-rays between 27 keV and 103 keV. The least probable α-decay channel has a 1.66 % probability to generate

a 5.388 MeV α, which is followed by a wide range of γ-rays each with a very small intensity. Although there are lots of X- and γ-rays produced along with the emission of α, they are highly suppressed by the 2 mm thick lead shielding around the source since the attenuation length of 100 keV γ-ray is $\sim$170 µm [61].

The α generated by ^{241}Am interacts with the ^{9}Be that is well mixed with the americium powder. Since the α only travels a small distance, it captures on ^{9}Be nucleus with a high probability, which results in a compound, unstable ^{13}C* nucleus. The excitation energy of this carbon nucleus varies from 9.9 MeV to 15.5 MeV. The excited ^{13}C* quickly de-excites, as listed in Equation 4.4, to ^{12}C and emits neutron with energy from 0 MeV to 11.2 MeV as shown in Figure 4.1.

$$
{}^{9}\mathrm{Be} + {}^{4}\mathrm{He} \rightarrow {}^{13}\mathrm{C}^{*} \rightarrow \begin{cases} {}^{12}\mathrm{C} + n & & (\mathrm{Br} = 36\,\%), \\ {}^{12}\mathrm{C}^{*} + n, & {}^{12}\mathrm{C}^{*} \rightarrow {}^{12}\mathrm{C} + \gamma(4.439\,\mathrm{MeV}) & (\mathrm{Br} = 61\,\%), \\ {}^{12}\mathrm{C}^{**} + n, & {}^{12}\mathrm{C}^{**} \rightarrow {}^{12}\mathrm{C}^{*} + \gamma(3.215\,\mathrm{MeV}) & (\mathrm{Br}{=}3\,\%), \\ & {}^{12}\mathrm{C}^{*} \rightarrow {}^{12}\mathrm{C} + \gamma(4.439\,\mathrm{MeV}) & . \end{cases} \tag{4.4}
$$

When ^{13}C* de-excites, there are also three decay channels all with the emission of neutron. There is 36 % chance that only neutron is generated. The dominant channel produces a neutron along with a γ-ray with energy of 4.439 MeV. At the rest $\sim$3 % time, a neutron and two γ-rays with energy of 3.215 MeV and 4.429 MeV are produced. Since the high energy γ-rays are in coincidence with the neutrons, it is difficult to study the neutron thermalization and capture signals in NV. In the data analysis, dedicated effort was made to separate these two different categories of events.

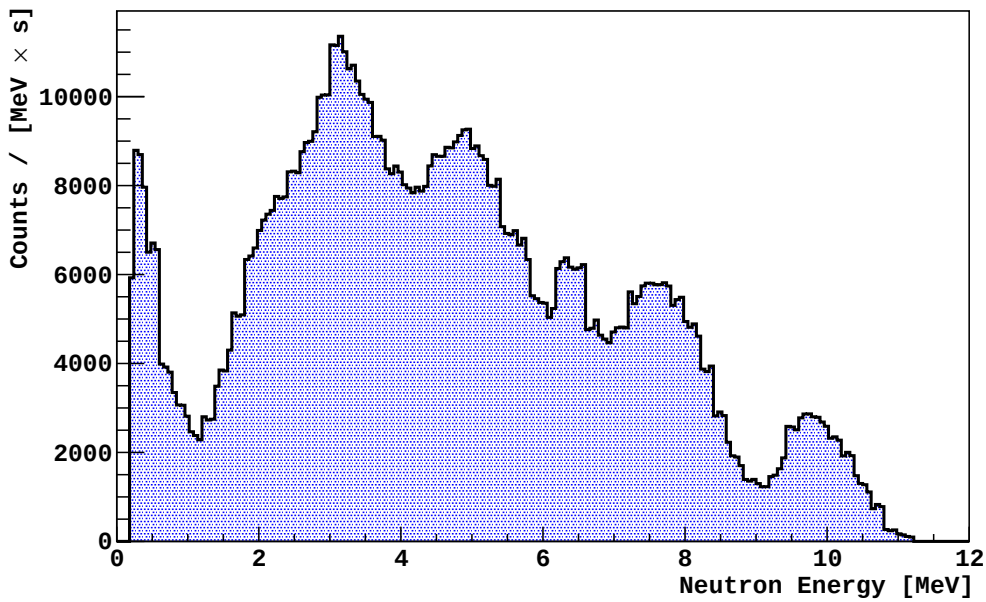

Figure 4.1: Neutron energy spectrum from ^{241}Am^{9}Be source.

4.1.2 Collimator

So far, there have been three ^{241}Am^{9}Be neutron calibration campaigns with different neutron activities in DarkSide-50. The first calibration campaign started with the ^{241}Am^{9}Be neutron activity of 2000 n s^{-1} on December 4, 2014. This campaign lasted a week with the goal to test the TPC x-y position algorithm developed for DarkSide-50. The neutron source was placed close to the TPC in a collimator inside the NV, as shown in Figure 4.3. In DarkSide-50, the collimator is a 40 cm long cylinder with an inner radius of 1 cm. The outer layer of the collimator is made of 1 mm thick stainless steel. The collimator is filled with air and sealed, as shown in Figure 4.2. It creates a tunnel for neutron to get into TPC. Without the collimator, the neutron is likely to lose most of its energy by interacting with the ^{1}H and ^{12}C isotopes in the organic liquid scintillator. The ^{241}Am^{9}Be source is attached near the end of the collimator, as shown in Figure 4.4.

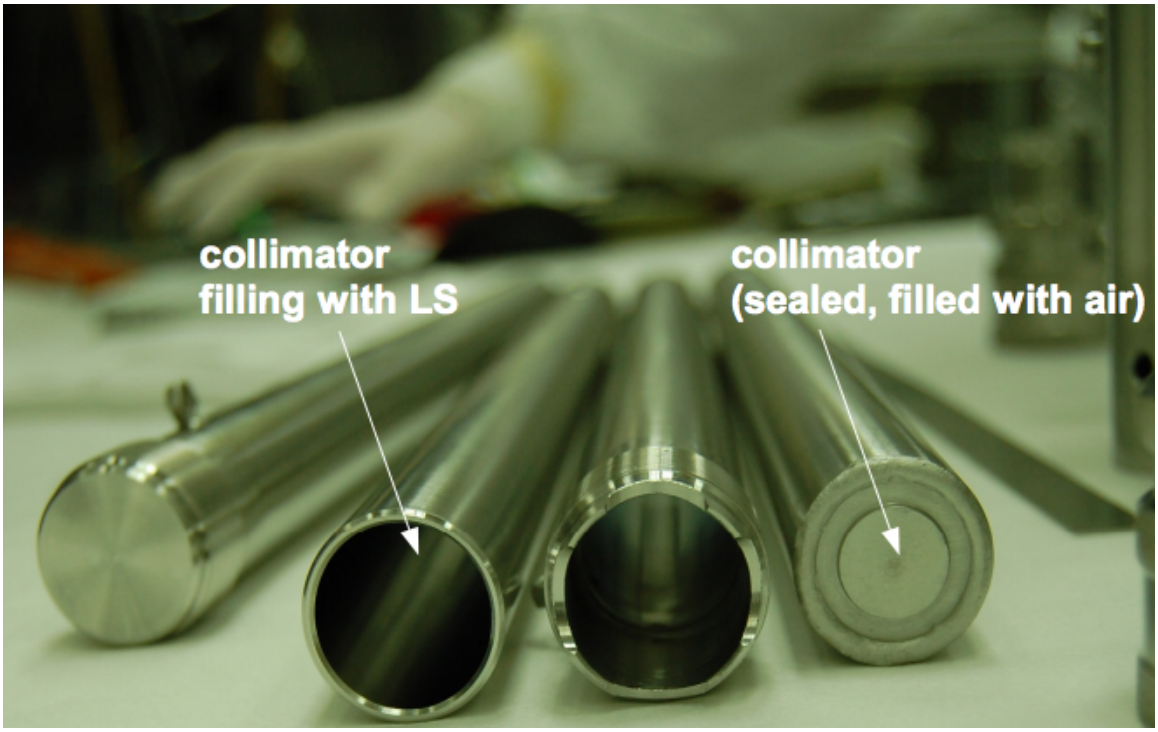

Figure 4.2: Actual collimator used in the campaign. The collimator sealed on both ends was used to take neutron calibration data. The collimator with holes on both ends is filled with Liquid Scintillator (LS) when deployed to take data for background purpose.

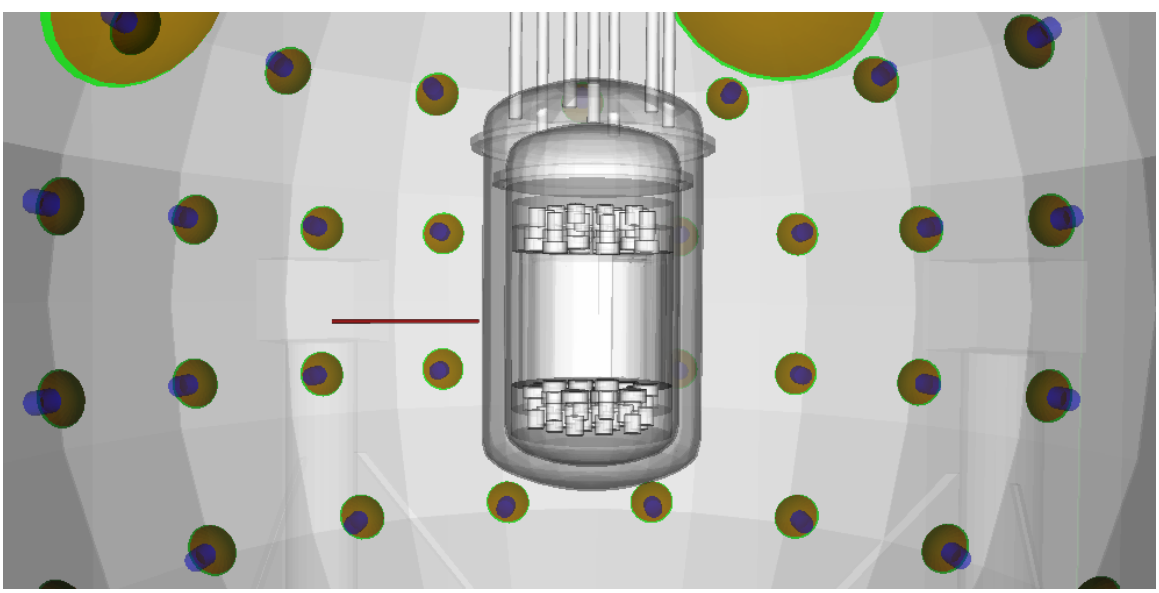

Figure 4.3: Horizontal Collimator (red tube) close to the TPC.

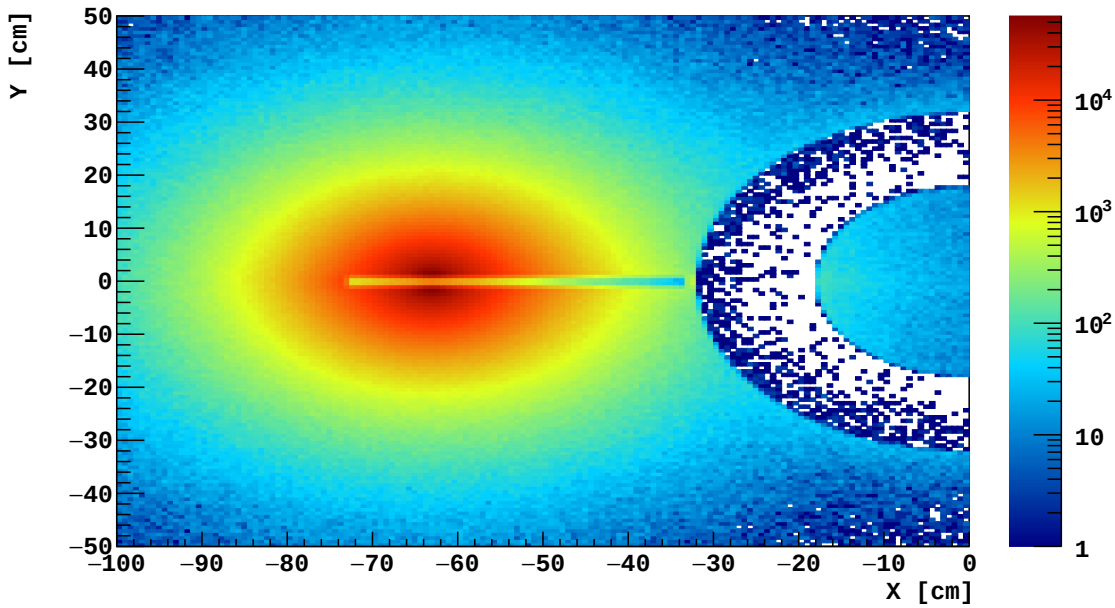

Figure 4.4: Energy depositions in x-y plane of the detector in MC. The horizontal (in the x direction) collimator is 40 cm long with a center of (-53,0,-3.65) cm in the NV. The ^{241}Am^{9}Be source is at (-63,0,-3.65) cm. Most of neutrons are captured in NV without reaching TPC (the blue semi-circle on the right side).

During this campaign, the center of the horizontal (in the x direction) collimator is fixed at (-53,0,-3.65) cm with respect to the NV coordinate system. The center of the NV is at (0,0,0) cm while that of the TPC is at (0,0,-3.65) cm in the NV coordinate system. The ^{241}Am^{9}Be source is at (-63,0,-3.65) cm. The neutron emitted from ^{241}Am^{9}Be source travels in the x direction. The fraction of the neutron emitted isotropically from the ^{241}Am^{9}Be source reaching the TPC is relatively low since the solid angle ($\sim 2.8 \times 10^{-4}$) is small based on MC calculation. As shown in Figure 4.4, most of the neutrons deposit energy or get captured in the liquid scintillator. The neutrons that travel along the collimator and then survive the $\sim$1 cm gap between the collimator and the cryostat are able to reach the TPC. In order to enhance the events seen in the TPC, it is necessary to accumulate data over a sufficiently long period of time.

Even if the neutron activity of this ^{241}Am^{9}Be source is very high (2000 n s^{-1}), the data taken within only one week were not sufficient enough for the x-y position resolution study. Figure 4.5 shows the energy depositions from the neutrons spread in the x-y plane of the TPC since the neutrons scatter on the detector components. In particular, the neutron can lose a big fraction of its energy and change its direction when scattering with carbon and fluorine isotopes in the teflon layer, which is located between the NV and TPC. When the surviving neutron enters the TPC, it is not well collimated, therefore spreads in the x-y plane. Although the energy depositions in the y-z plane are more prominent, they do not give a strong support for the x-y position algorithm.

In order to compare the signals from collimator with those from background, the sealed collimator was replaced with a pipe that is open at both ends, as shown in Figure 4.2, so that the liquid scintillator can immerse the whole pipe. Although the ^{241}Am^{9}Be was still inside the pipe, the emitted neutron is less likely to reach the TPC. Since the attenuation length of the neutron in the liquid scintillator is $\sim$20 cm, which is smaller than the distance (30 cm) from the neutron source to the TPC, there is a high probability for the neutron to be captured in the liquid scintillator before reaching the TPC. Table 4.1 compares the events generated and selected with the collimator to those from background (indicated as "without collimator"). The fraction of single NR events in the TPC without collimator is 0.07 %, which only increases slightly to 0.09 % when deploying the collimator. In Figure 4.6, there are more events resident around the center of the y axis with collimator (in the x direction) than without. The peak gives a resolution of $\sim$2 cm in the y direction as well as in the x direction, which is worse than the expectation.

Since the neutron from ^{241}Am^{9}Be source traveling through the collimator did not give a satisfying x-y resolution in the TPC, it is interesting to study the result from a neutron beam. In MC, a neutron beam with energy of 1 MeV was placed inside the

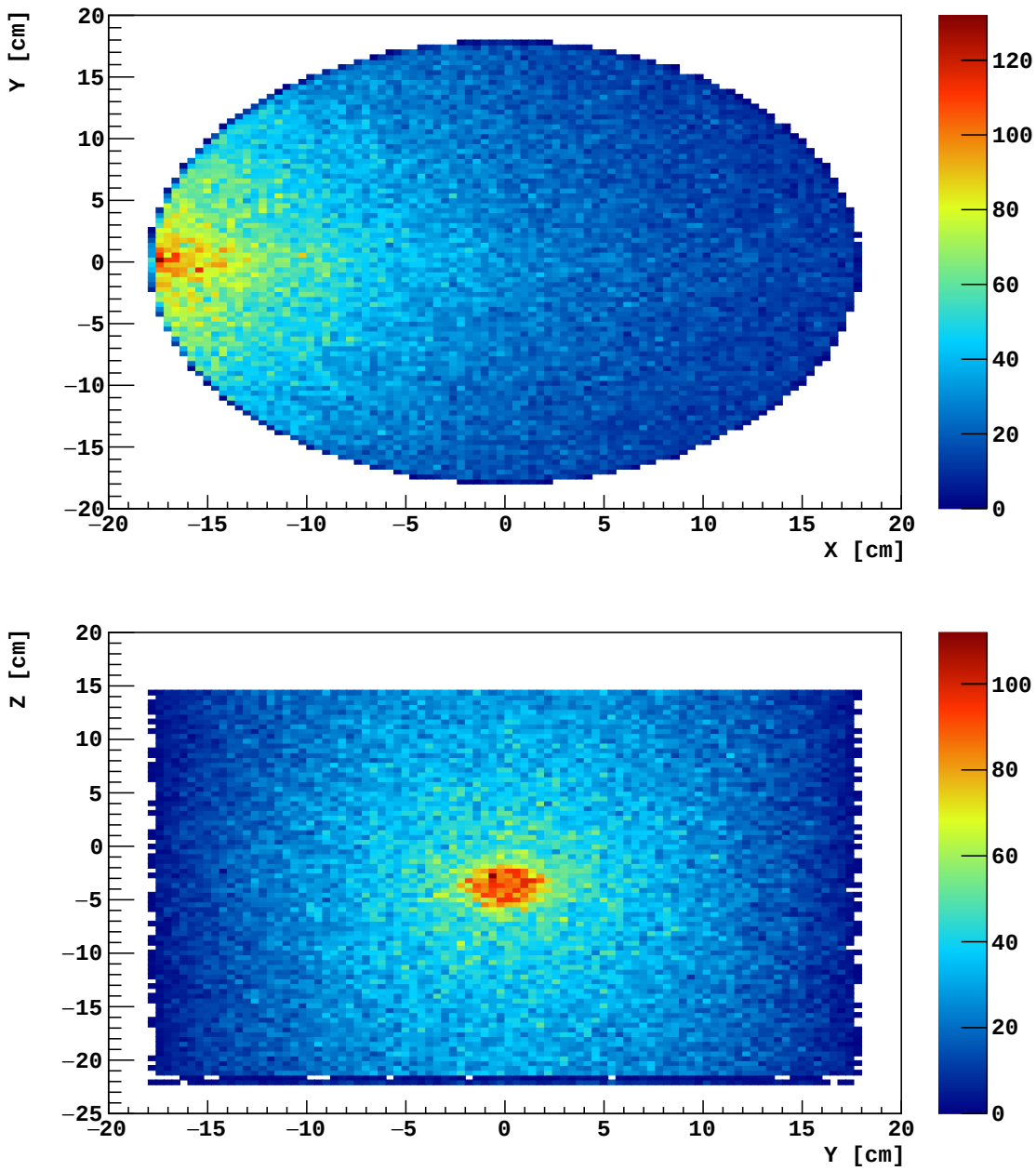

Figure 4.5: Top: Energy depositions in the x-y plane of the TPC. The collimator is in the x direction. The depositions spread in the y direction. Bottom: Energy depositions in the y-z plane of TPC. The depositions are concentrated in a circle with a radius of $\sim$2 cm.

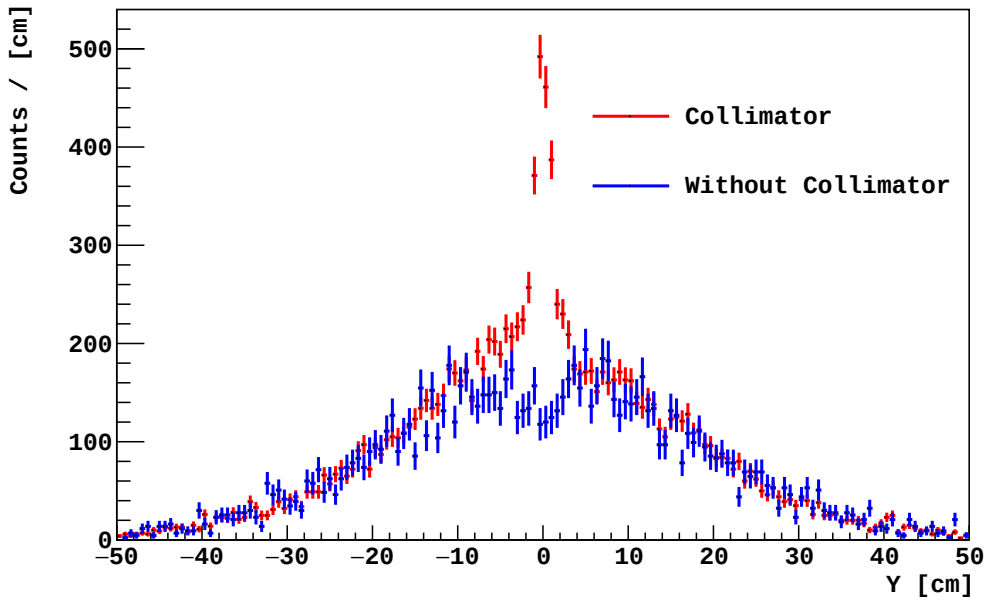

Figure 4.6: Comparison of the energy depositions in the y direction between data taken with and without collimator that lies in the x direction. Neutron traveling through the collimator gives a clear, prominent peak (red) at the center of the y axis.

Table 4.1: Number of selected events from data taken with and without collimator. The ratios shown are calculated with respect to total events.

Events Selection	**With Collimator**	**Without Collimator**
Total Events	59 991 374	29 999 435
In TPC	573 012 (1.0 %)	236 908 (0.79 %)
NR	179 873 (0.30 %)	63 488 (0.21 %)
Single Scattering	189 796 (0.32 %)	80 742 (0.27 %)
Single NR Scattering	52 734 (0.09 %)	19 698 (0.07 %)

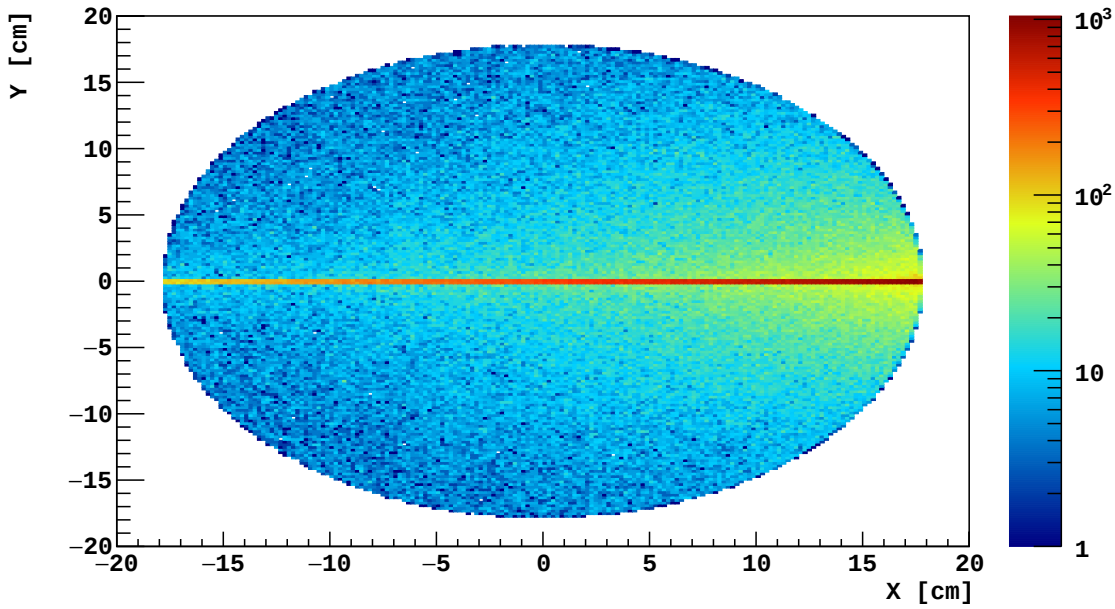

Figure 4.7: Energy depositions in x-y plane of the TPC in MC. The neutron beam (red), in the x direction, travels through the TPC with small fluctuations in y direction.

collimator. The neutron beam can travel along the collimator almost without any collision in the liquid scintillator. With the same data analysis as before, Figure 4.7 shows the neutron beam leaves a perfect straight line track in the x direction. With this design, neutron beam gives a clear and reliable x-y position resolution, which is helpful to improve the x-y position algorithm.

Since it is feasible to get a good x-y position resolution using a neutron beam, the Deuterium-Deuterium (DD) neutron generator is brought to attention. It uses Deuterium (D, ^{2}H) fusion reaction to generate neutrons by creating ionizations of deuterium and accelerating them into a hydride target loaded with deuterium:

$$\mathrm{D} + \mathrm{D} \longrightarrow n + {}^3\mathrm{He}, \quad E_n = 2.5\,\mathrm{MeV}. \tag{4.5}$$

Neutrons produced by the DD reaction are emitted relatively anisotropically from the target and slightly peaked in the forward (along the axis of the ionization beam) di-

rection. Compared with ^{241}Am^{9}Be, DD neutron generators can produce much higher neutron activity ($\sim 2 \times 10^{9}\,\mathrm{n\,s^{-1}}$). However, it requires extra power supply and the size is relatively larger than the ^{241}Am^{9}Be neutron source. In order to deploy the DD neutron generator, it is possible to install it outside the MV and hang a pipe as the collimator, inside the NV and MV, to the same height as the generator, as pioneered in LUX experiment [62].

4.1.3 Neutron Capture Signal

The second ^{241}Am^{9}Be neutron source campaign was carried out on January 22, 2015 and lasted almost one month. The calibration source with a neutron activity of $10\,\mathrm{n\,s^{-1}}$ was placed inside a source holder. A 2 mm thick layer of lead surrounding the neutron source can shield the detector from the X-rays with low intensity produced by ^{241}Am decay. The main goal of this calibration was to detect the delayed neutron capture signals especially on ^{10}B. During this campaign, data were taken at different positions in the NV in order to test the position dependence of the results. One was close to the TPC cryostat, and the other was $\sim$72 cm away from the cryostat. At that time, the TMB concentration in the NV was 5 %. However, during the campaign, the PPO concentration was increased from $0.7\,\mathrm{g\,L^{-1}}$ to $1.4\,\mathrm{g\,L^{-1}}$ in order to measure the impact of the PPO concentration on the α quenching. The scintillator has kept the higher concentration of PPO since then. Around one and half years later, a third ^{241}Am^{9}Be neutron campaign was conducted on May 31, 2016 and lasted a week. At that time, the neutron activity of the source was $160\,\mathrm{n\,s^{-1}}$. The purpose of this campaign was to check the stability of the NV and study the NR events in the TPC. The data were taken with the ^{241}Am^{9}Be source close to the TPC.

When the source was close to the TPC, the high energy γ-rays and neutrons from ^{241}Am^{9}Be are likely to collide with the atoms in the TPC. The PSD separates the ER from NR events as shown in Figure 4.8. In order to clearly select NR events, a

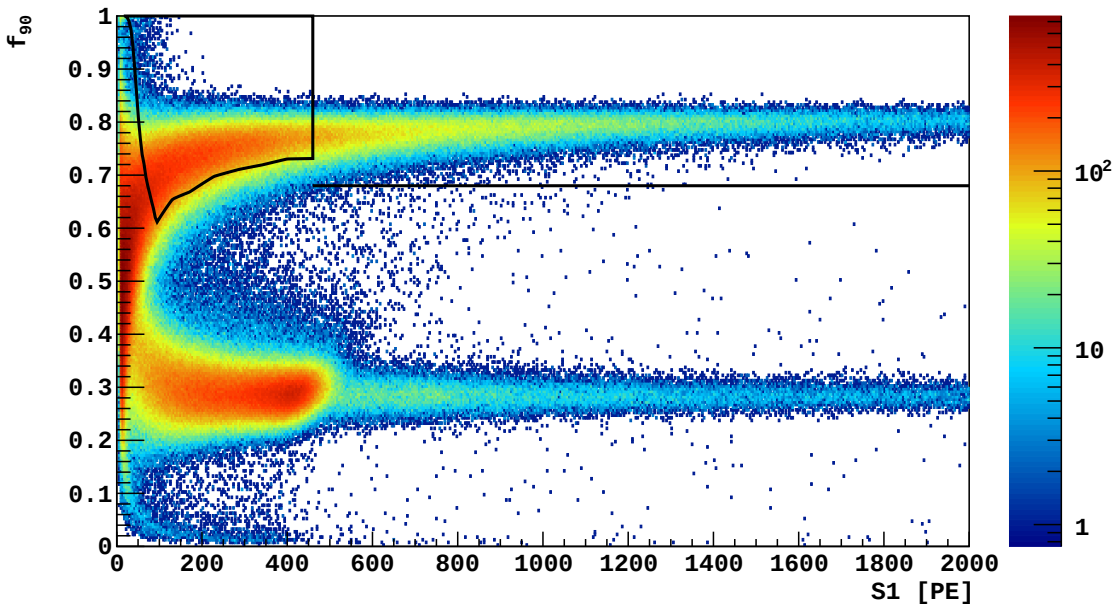

Figure 4.8: Distribution of events in the f_{90} vs S1 plane from data taken with the ^{241}Am^{9}Be neutron source. A dark matter box (black box at the top left corner) along with a region with f_{90} larger than 0.68 when S1 > 460 PE was applied to select NR events.

Table 4.2: List of selected events from the second and third ^{241}Am^{9}Be neutron calibration campaign. The neutron activity of the ^{241}Am^{9}Be source is $10\,\mathrm{n\,s^{-1}}$ in the second campaign and that is $160\,\mathrm{n\,s^{-1}}$ in the third campaign.

	second campaign	**third campaign**
Total Events	5 091 312	5 179 915
Live Time	390 929 s (4.5 d)	473 830 s (5.5 d)
NR Events	40 219	431 128
NR Fraction	0.79 %	8.32 %
NR Rate	$0.10\,\mathrm{n\,s^{-1}}$	$0.91\,\mathrm{n\,s^{-1}}$

dark matter box (the black box at the top left corner in Figure 4.8) along with an extended region of $f_{90} > 0.68$ when S1 > 460 PE is applied. Table 4.2 summarizes the selected events in two ^{241}Am^{9}Be neutron calibration campaign.

Since the neutron is not likely to lose all the energy in the TPC, it leave signals in the NV as well. Once it leaves the TPC, the energetic, fast neutron rapidly lost its energy by elastic scattering with low atomic number isotopes like ^{1}H and ^{12}C. As

the residual energy of the neutron decreases or even reaches the thermal energy, the likelihood of neutron capture increases. In the organic liquid scintillator, the neutron thermalization occurs within ∼200 ns, which is included in the prompt window as described in Section 3.2. The black curve in Figure 4.9 shows a high energy peak between 2000 PE and 3500 PE, which is from 4.4 MeV γ-ray correlated with neutron. In this case, the neutron goes into the TPC while the γ-ray scatters in the NV. It is also possible the γ-ray travels into the TPC, lost part of the energy due to collisions with argon nuclei, and then γ-ray deposits the rest energy in the NV. γ-ray in these two scenarios contributes to the broad energy peak in the prompt window. Besides the high energy peak, there are more events resident at very small energy region in the prompt window due to the neutron thermalization and after-pulses.

Table 4.3: List of capture cross sections for and energy of the most prominent capture γ-rays from neutron capture on isotopes. The ^{10}B, ^{1}H, ^{12}C, and ^{16}O are elements of the liquid scintillator while ^{56}Fe is from the TPC cryostat.

Isotope	**Cross Section** [b]	**γ-ray Energy** [keV]
^{10}B	3838	478
^{1}H	0.332	2224.6
^{12}C	3.86×10^{-3}	4947
^{16}O	189.9×10^{-6}	4144.6
^{56}Fe	2.591	7646.1

In contrast to the prompt window, there are more structures in the delayed window, as shown in Figure 4.9. The low energy part ($<$ 60 PE) are dominated by after-pulses and the highly quenched α+^{7}Li peak from ^{10}B neutron capture. The next dominant peak between 200 PE and 300 PE comes from the 478 keV γ-ray as a product of neutron capture on ^{10}B. The peak around 1000 PE is from the neutron capture on ^{1}H, which has a smaller neutron capture cross section than ^{10}B. The 2500 PE peak is from neutron capture on ^{12}C while the 4000 PE one results from neutron capture on ^{56}Fe. These neutron capture signals are the main goal of ^{241}Am^{9}Be

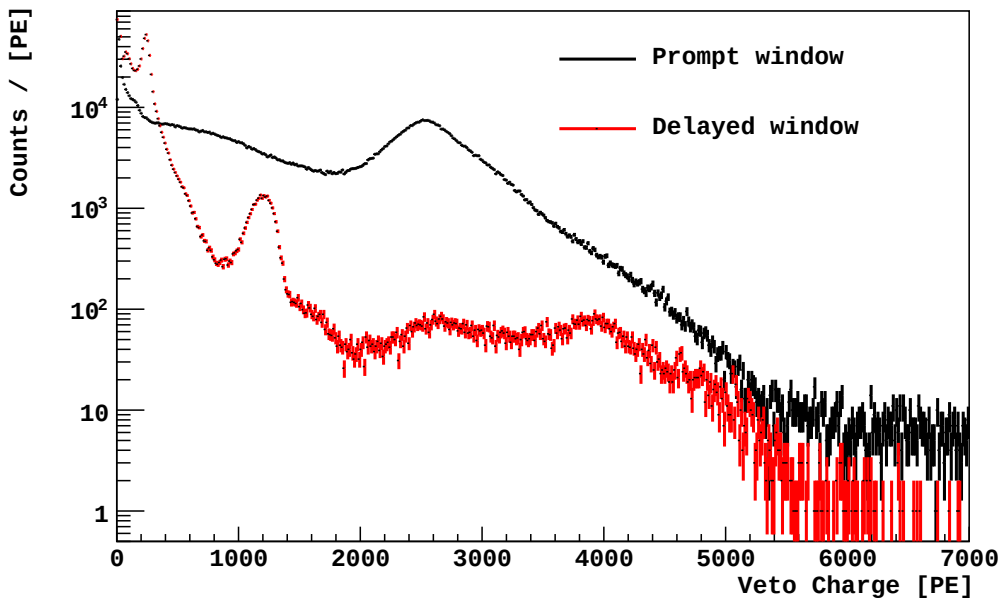

Figure 4.9: Comparison of the charge spectrum between the prompt window (black) and the delayed window (red) of the NV from ^{241}Am^{9}Be data. See text for the explanation of the structures in the spectra.

neutron calibration campaign. Table 4.3 summarizes the cross section and the energy of the resulting γ-rays from neutron capture on an isotope.

As mentioned above, the α+^{7}Li peak overlaps with the after-pulses, which are difficult to be distinguished from neutron capture signals. Since the neutron capture time is estimated to be $\sim$20 µs, only the first cluster after 20 µs is selected in order to remove after-pulses. Figure 4.10 shows the charge spectrum of these selected clusters after subtracting background. The α+^{7}Li peak from neutron capture on ^{10}B (see Equation 2.15) appears in the lower energy peak while the α+^{7}Li+γ peak contributes to the higher energy peak between 200 PE and 300 PE.

In order to measure the peaks precisely, both of the peaks are measured by fitting a gaussian distribution function. The low energy peak is at 20.90 ± 0.25 PE while the high energy peak is at 246.70 ± 0.37 PE. According to Equation 2.15, the ratio of the α+^{7}Li peak to the total of neutron capture on ^{10}B is 6.4 %. However, the result

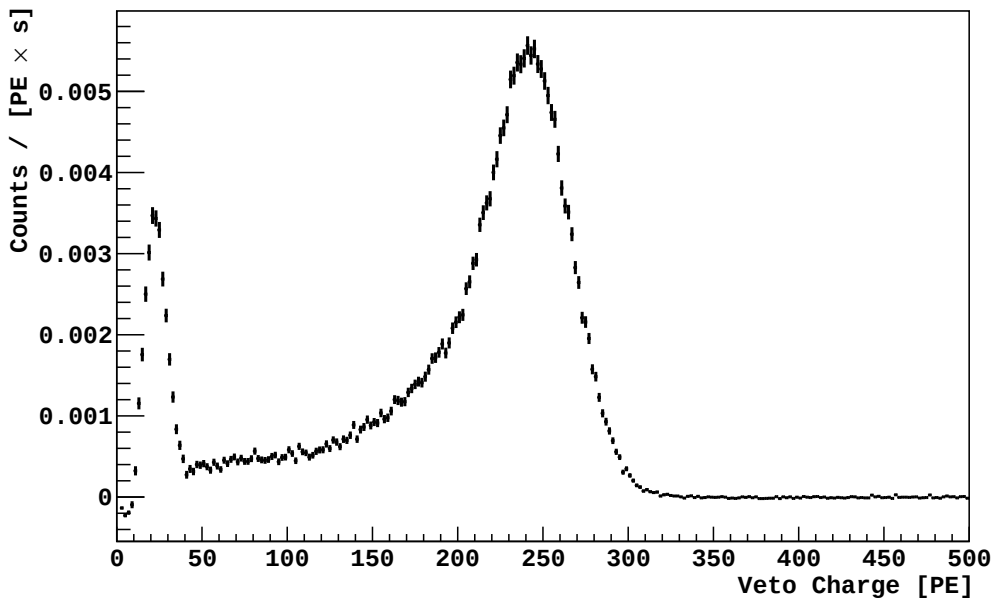

Figure 4.10: Charge distribution from neutron capture on ^{10}B with background subtracted. The data were taken when ^{241}Am^{9}Be was close to TPC. The lower peak (between 10 PE and 50 PE) is from α+^{7}Li channel while the higher peak (between 150 PE and 300 PE) is from α+^{7}Li+γ channel.

from data, taken when neutron source was close to the TPC, is $10.50 \pm 0.35\,\%$. The discrepancy of this ratio between the theory and the experiment causes doubts, so more effort was made to check the results. One way is to check the time dependence of this ratio. As shown in Figure 4.11, the events were selected with the same criteria in three time windows, for instance selecting the first cluster after 20 µs, and so on for 30 µs and 40 µs. This ratio increased by 0.77 % from 10.50 % to 11.27 % in three time windows, which is believed to be consistent due to the statistical uncertainty.

Besides that, it is also helpful to check the neutron capture time. Figure 4.12 shows the time distribution of the clusters with respect to the TPC trigger time. The neutron capture time is 21.68 ± 0.66 µs calculated by fitting an exponential function. This value is consistent with the expected neutron capture time of $\sim$22 µs.

Besides the calibration data, the ^{241}Am^{9}Be neutron source along with the source holder were simulated to help understand the discrepancy of the ratio from α + ^{7}Li

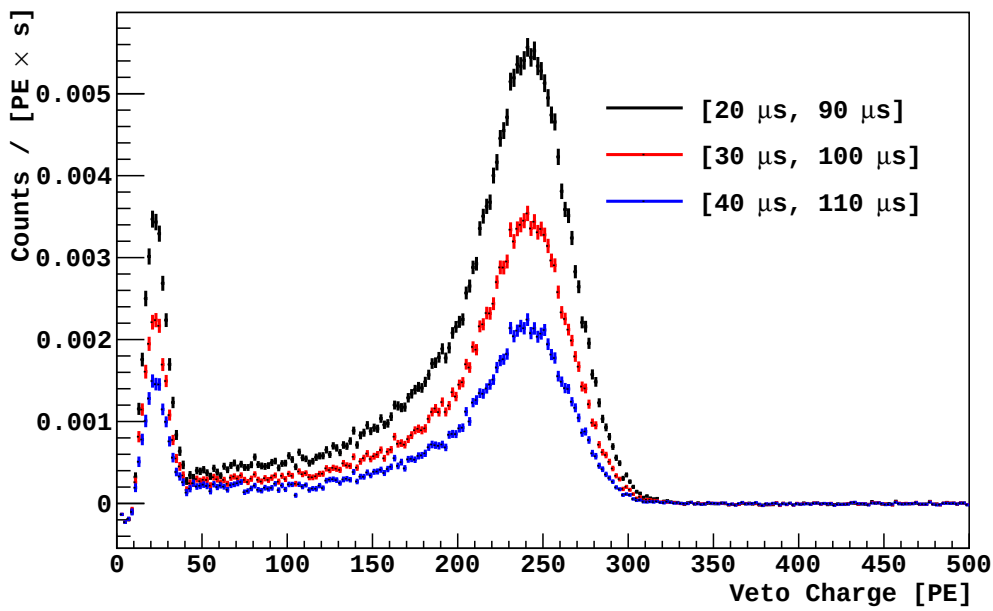

Figure 4.11: Comparisons of the background subtracted charge spectrum from neutron capture on ^{10}B among three different windows. The branch ratio of the α+^{7}Li peak and the positions of two peaks are consistent in three windows.

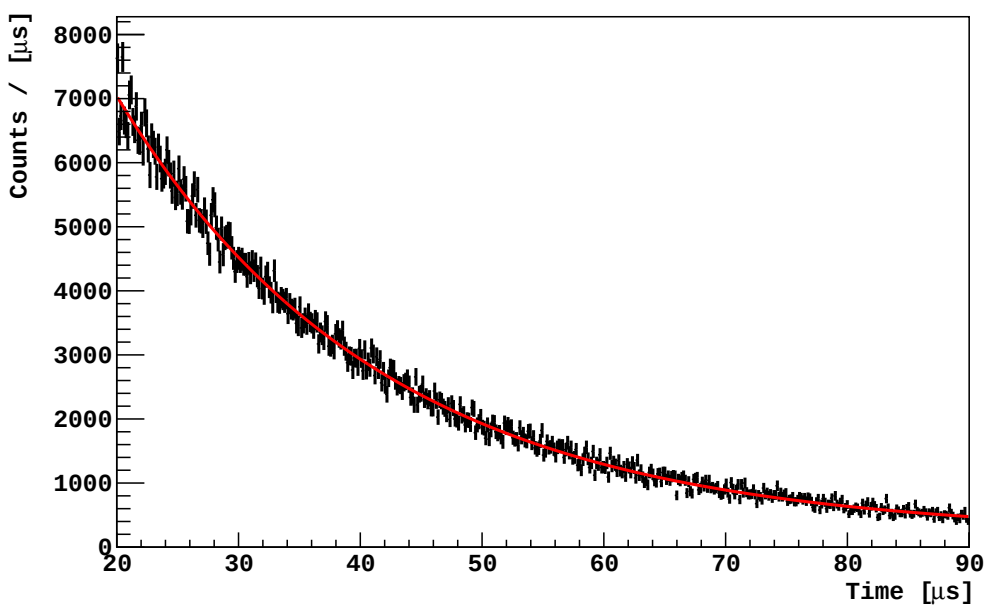

Figure 4.12: Time distribution from neutron capture on ^{10}B. The time distribution (black) is fitted by an exponential function (red), which gives the neutron capture time of $21.68 \pm 0.66\,\mu$s.

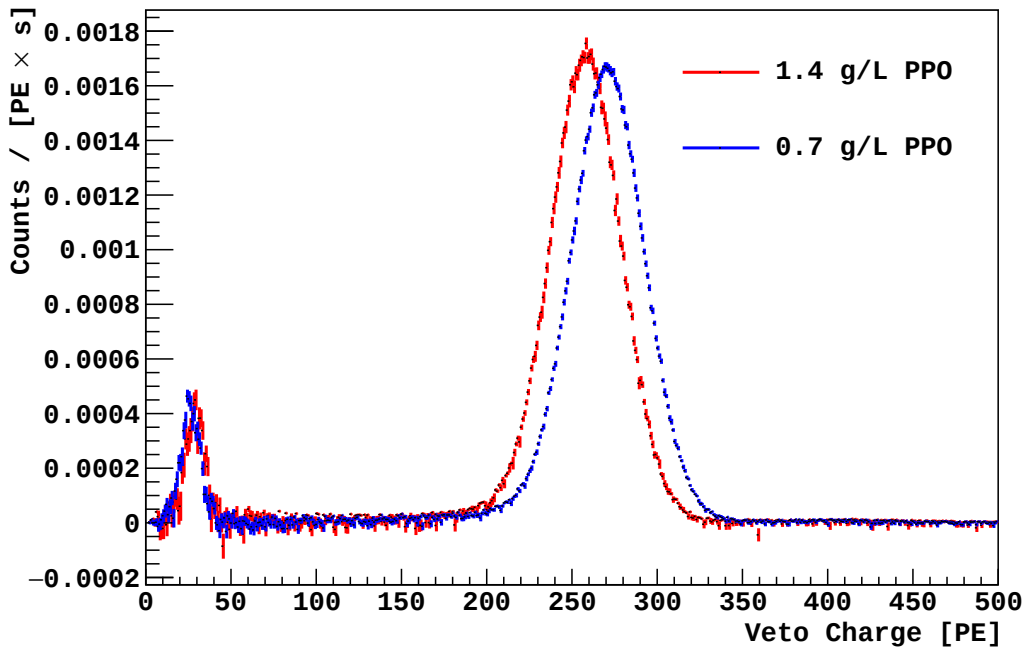

Figure 4.13: Comparison of the background subtracted charge distribution from neutron capture on ^{10}B between different concentrations of PPO. Both spectra are based on data taken when the ^{241}Am^{9}Be source was away from the TPC. After adding more PPO, the α+^{7}Li peak increases from 27.6 PE to 29.1 PE while the α+^{7}Li+γ peak decreases from 277.8 PE to 264.5 PE (see Table 4.4 for details.)

peak. The same event selections as data were also implemented in MC. It turns out that ∼8 % of the 478 keV γ-ray from the α + ^{7}Li + γ channel (that is the excited state of ^{7}Li) can escape the NV by going back into the TPC cryostat. In that case, only the 1471 keV α and the 839 keV ^{7}Li from the excited state of ^{7}Li contribute to the production of scintillation light. Due to the high quenching effect, the α and ^{7}Li are reconstructed to the lower energy peak in Figure 4.11. Since the energy of α and ^{7}Li generated from the excited state of ^{7}Li is similar to that from the ground state and the energy resolution of the detector is limited, the two components are mixed together in the lower energy peak. Therefore, the ratio of α + ^{7}Li channel measured is higher than that in theory.

Later on, the ^{241}Am^{9}Be was rotated away from the TPC in order to study the position dependence of the neutron capture signals. In that case, the neutrons and γ-rays deposit almost all the energy in the NV without reaching the TPC. The ratio of α + ^{7}Li peak decreased to $\sim$6 %, which is close to the theoretical value (6.4 %). The lower energy peak in Figure 4.10 increased by $\sim$32 % from 20.9 PE to 27.6 PE while the higher peak increased by $\sim$13 % from 246.7 PE to 277.8 PE. In addition to the neutron capture on ^{10}B, there is $\sim$8 % neutron capture on ^{1}H. This fraction is measured by integrating the number of events from each neutron capture peak in the background subtracted charge spectrum.

In the second ^{241}Am^{9}Be neutron campaign, the PPO increased from 0.7 g L^{-1} to 1.4 g L^{-1}. The addition of PPO leads to another interesting effect. When the ^{241}Am^{9}Be source was away from the TPC, the energy peak from the α+^{7}Li channel increases by 1.5 PE ($\sim$5 % increase) while that from the α+^{7}Li+γ channel decreases by 13.3 PE ($\sim$5 % decrease), as summarized in Table 4.4. Figure 4.13 clearly illustrates the changes of the energy peaks after adding more PPO.

Table 4.4: List of branching ratio, α+^{7}Li peak, and α+^{7}Li+γ peak. The data were taken when ^{241}Am^{9}Be source with a neutron rate of 10 n s^{-1} was close to and away from the TPC, with different PPO concentrations in the liquid scintillator.

	^{241}Am^{9}Be close to TPC		**^{241}Am^{9}Be away from TPC**	
	0.7 g L^{-1} PPO	1.4 g L^{-1} PPO	0.7 g L^{-1} PPO	1.4 g L^{-1} PPO
Branching Ratio [%]	10.50 ± 0.35	12.47 ± 0.43	6.15 ± 0.18	5.84 ± 0.26
α+^{7}Li Peak [PE]	20.90 ± 0.25	22.71 ± 0.27	27.60 ± 0.11	29.10 ± 0.19
α+^{7}Li+γ Peak [PE]	246.70 ± 0.37	235.77 ± 0.44	277.80 ± 0.19	264.50 ± 0.28

The results from the second ^{241}Am^{9}Be neutron calibration campaign give us a comprehensive understanding of the neutron capture features, especially the position dependence and the effect of different PPO concentrations in the scintillator. After this campaign, DarkSide-50 continued to take the regular UAr WIMP-search data. For a long-term experiment, the stability of the NV needs to be checked periodically. With that concern, the collaboration prepared a new ^{241}Am^{9}Be neutron source for

the third neutron calibration. The neutron activity of the new ^{241}Am^{9}Be source was 160 n s^{-1}. Table 4.5 summarizes the results from the two neutron calibration campaign. The neutron capture signals are consistent with each other. Because of the higher statistics, the uncertainty of the measurements is improved in the new calibration campaign, which further confirms the results achieved in the previous study. Although most of the results are similar, the light yield seems to increase by ∼2 % comparing the α+^{7}Li and α+^{7}Li+γ peaks in two campaigns. Figure 4.14 shows the slight shift of the peaks from neutron capture on ^{10}B.

Table 4.5: List of α+^{7}Li peak, α+^{7}Li+γ peak, branching ratio of α+^{7}Li peak, and neutron capture time from ^{241}Am^{9}Be data taken with 1.4 g L^{-1} PPO in the scintillator. The neutron activity of the ^{241}Am^{9}Be source is 10 n s^{-1} in the second campaign and that is 160 n s^{-1} in the third campaign.

	second campaign	**third campaign**
Branching Ratio [%]	12.47 ± 0.43	11.03 ± 0.24
α+^{7}Li Peak [PE]	22.71 ± 0.27	23.08 ± 0.09
α+^{7}Li+γ Peak [PE]	235.77 ± 0.44	240.47 ± 0.16
Neutron Capture Time [µs]	21.68 ± 0.66	21.81 ± 0.20

4.2 ^{241}Am^{13}C Source Calibration

In the previous two ^{241}Am^{9}Be neutron campaigns, we studied the neutron capture signals in the delayed window. However, due to the intrinsic feature of this ^{241}Am^{9}Be neutron source, 64 % of the generated neutron is also accompanied by at least one γ-ray, which is most likely to leave signals in the prompt window of the NV. It is extremely difficult to separate the γ-ray from neutron thermalization signals, which is another important feature of the NV. Based on the neutron thermalization signals, it is also possible to detect and reject the neutrons, which is the most important source of background in a WIMP search experiment. In order to calculate the neutron veto efficiency based on the neutron thermalization signals in the prompt window, it is

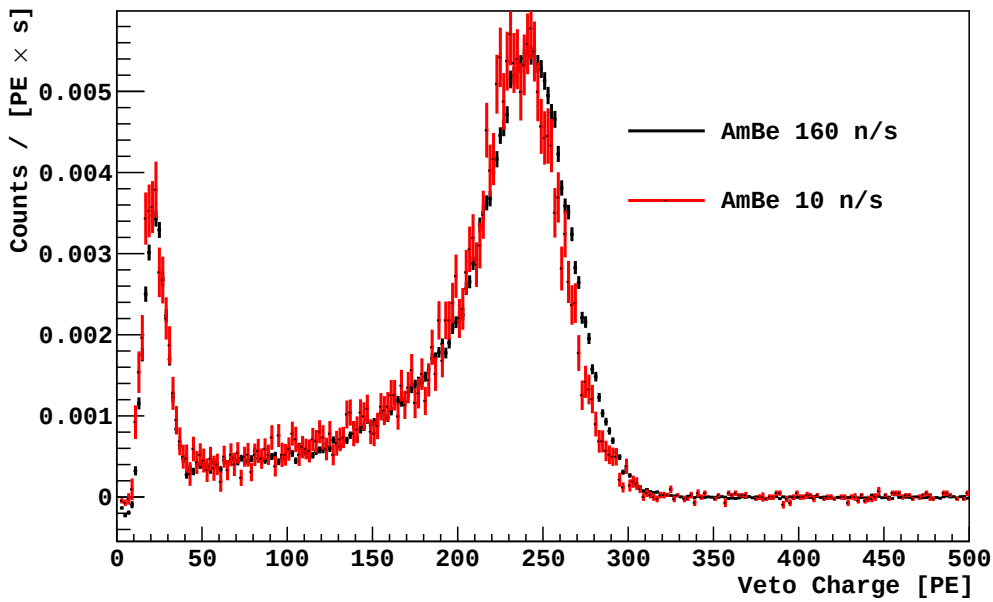

Figure 4.14: Comparison of charge distribution from neutron capture on ^{10}B between two ^{241}Am^{9}Be sources. The energy peaks measured with 160 n s^{-1} ^{241}Am^{9}Be data (black) increases by 2 % compared with the results from 10 n s^{-1} ^{241}Am^{9}Be data (red).

essential to deploy a neutron source with highly or completely suppressed coincident γ-rays. With that goal, DarkSide-50 designed a ^{241}Am^{13}C neutron source that generates much cleaner neutrons.

4.2.1 ^{241}Am^{13}C Neutron Energy

As the ^{241}Am^{9}Be source, the neutron generation in ^{241}Am^{13}C also starts with the α-decay of ^{241}Am, which is described in Section 4.1.1. The α particle with energy of $\sim$5.5 MeV from ^{241}Am decay captures on a ^{13}C nucleus then triggers the ^{13}C(α,n)^{16}O reaction. The production of the neutron depends on the final state of ^{16}O, which could end up either in the ground state, the first or the second excited state. The threshold of the incident α energy to excite the ^{16}O is 5.048 MeV. The reaction generates a ground state ^{16}O if the α energy is below the threshold. However, the probability that the α energy from ^{241}Am decay is larger than 5.388 MeV is >99.5 %. Since the

chance to get an excited ^{16}O is large, it is necessary to eliminate the correlated γ-rays coming from the excited states. The unstable first excited state of ^{16}O decays to the ground state by emitting an e^+e^- pair with a total energy of 6.049 MeV. The positron (e^+) annihilates with an electron producing two γ-rays each with energy of 511 keV. The second excited state of ^{16}O emits a 6.13 MeV γ-ray in coincidence with the neutron. However, the γ-ray can be eliminated by keeping the energy of incident α particle below 5.048 MeV [63].

A commercial ^{241}Am source contains 100 µCi of ^{241}Am embedded in a gold foil. The mixture is placed on a 0.15-0.25 mm thick silver and a 2 µm thick protective gold foil, as shown in Figure 4.15. On top of the ^{241}Am source, there is a graphite disc, wrapped in gold foil, that is composed of a powder of 99 % pure ^{13}C. The ^{13}C is mixed with a $C_4H_6O_2$ binding agent. Extra one or two layers of 1 µm thick gold foil can be added between the ^{241}Am and ^{13}C source to further moderate the α energy [63]. In order to suppress the γ-rays, the ^{241}Am^{13}C source was surrounded by a ~2 mm thick lead layer, which was placed inside a source holder.

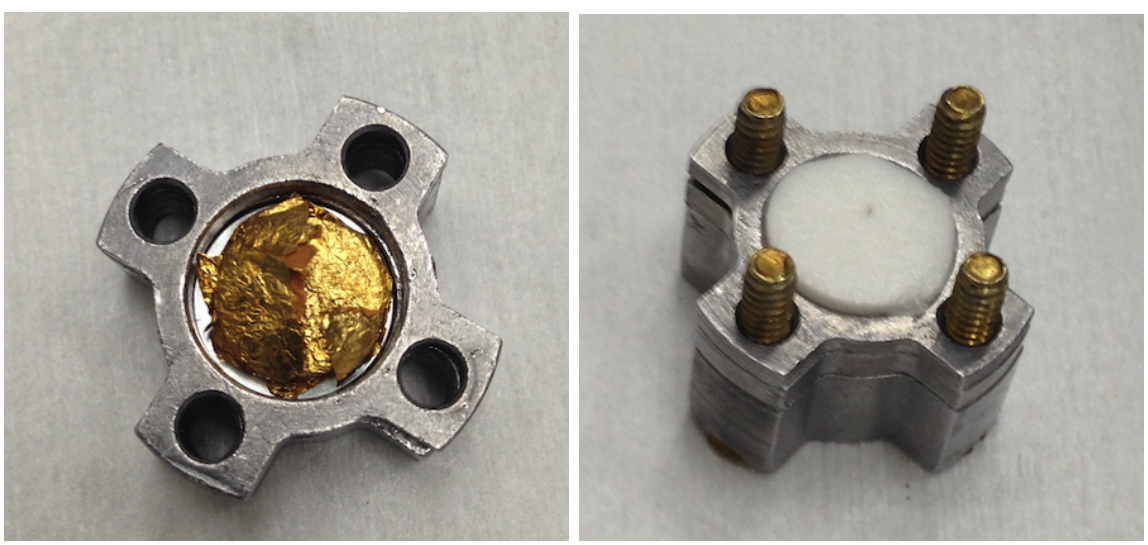

Figure 4.15: ^{241}Am^{13}C source wrapped in gold foil and the source holder.

In order to get the neutron energy spectrum from the ^{241}Am^{13}C source, the source geometry was implemented in the G4DS MC, as detailed in Shawn Westerdale's

thesis [47]. The α particle from the ^{241}Am^{13}C source scatters in the source and protective gold foil layer and eventually deposits energy in the ^{13}C with the emission of neutron. The α may travel in different directions and lose more energy in the longer path. The maximum energy deposited by α in ^{13}C turns out below 4.5 MeV, which can be even smaller with additional layers of gold foil.

Since the energy deposited in ^{13}C by α depends on the direction that α travels which is not isotropic, the energy spectrum and the outgoing angle of the neutron are correlated, as shown in Figure 4.16. The neutron energy spectrum is centered around 5 MeV and spreads between 2 and 7 MeV. The neutron is more likely to travel in the forward direction instead of backwards with respect to the normal of the gold-graphite interface in ^{241}Am^{13}C source.

4.2.2 ^{241}Am^{13}C Calibration Data Analysis

On December 16, 2015, the ^{241}Am^{13}C source was deployed into the NV and placed close to the TPC. One month later, the ^{241}Am^{13}C source was removed from the NV. During the campaign, the ^{241}Am^{13}C source was rotated away from the TPC for a short period to calculate the fraction of γ-rays leaked from the ^{241}Am^{13}C source, which was negligible. Since the focus of my research is the neutron thermalization signals in the prompt window, the results presented here are only based on the data taken when the ^{241}Am^{13}C source was close to the TPC.

When the ^{241}Am^{13}C was close to the TPC, particles from the source, mostly neutrons, scatter with the argon nuclei producing signals in the TPC. The neutron is likely to leave NR signals while the γ-rays mostly from the radioactive contamination in the detector materials produce ER signals in the TPC. Figure 4.17 shows the separation of ER and NR events in the S1 vs f_{90} distribution. Similar to the ^{241}Am^{9}Be analysis, the extended dark matter box is applied to select the NR events for further analysis. When the neutron leaves the TPC, it can elastically scatter with ^{12}C and ^{1}H

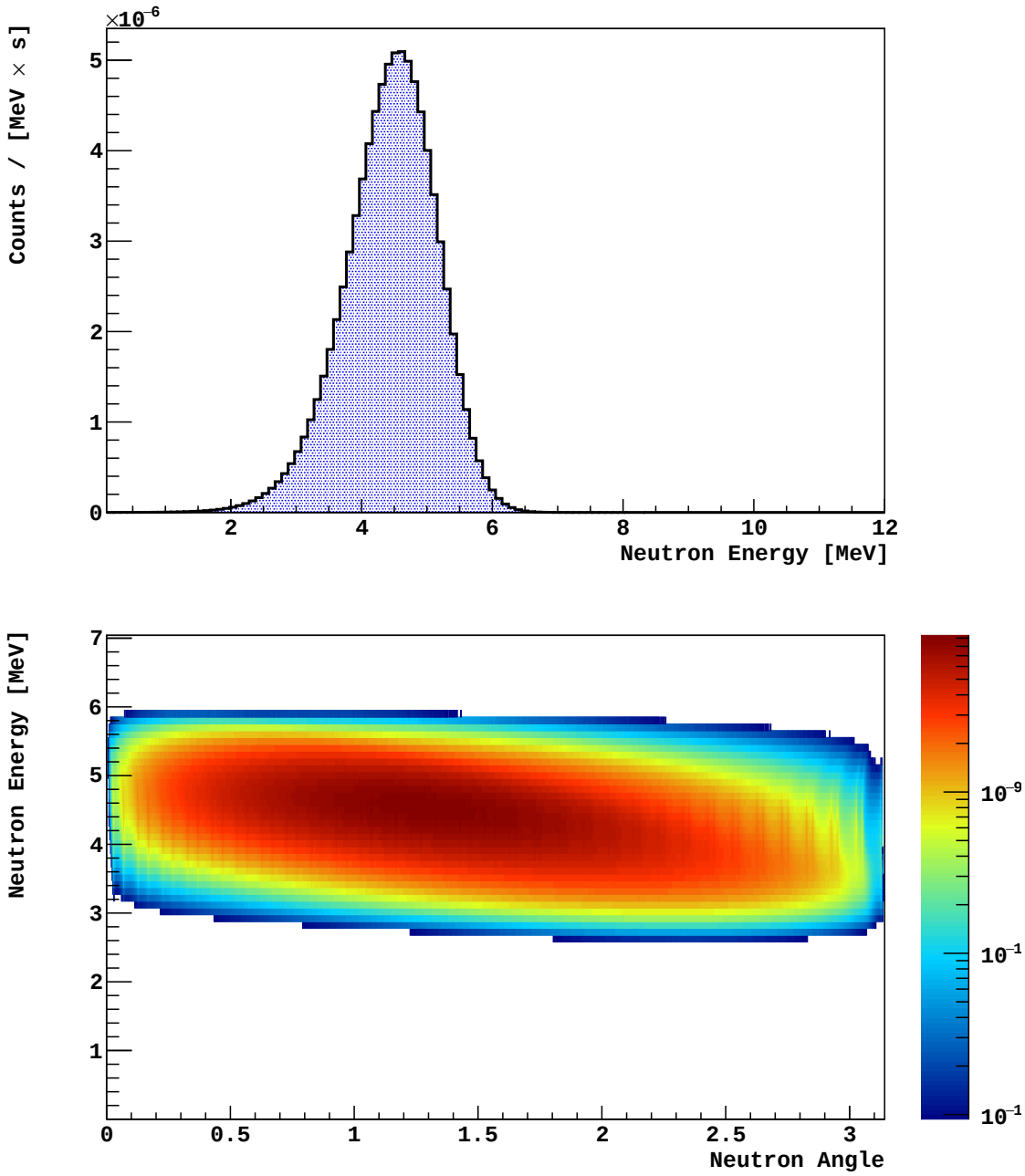

Figure 4.16: Top: Energy spectrum of the neutron from the ^{241}Am^{13}C source. Bottom: Energy vs angle distribution of the neutron from the ^{241}Am^{13}C source. The neutron is more likely to move forward instead of backward with respect to the normal of the gold-graphite interface in ^{241}Am^{13}C source.

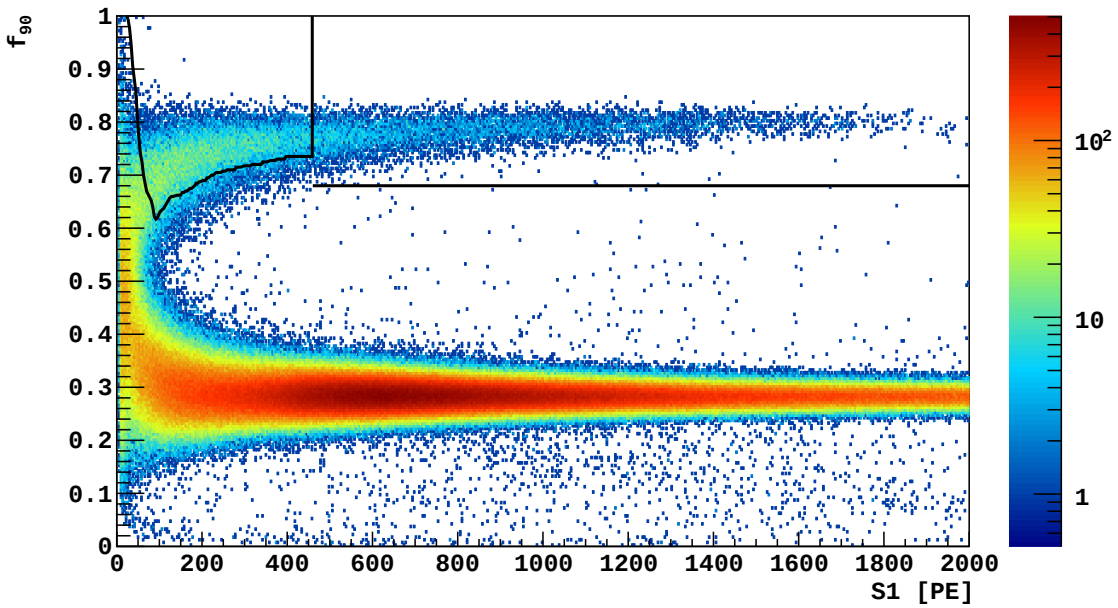

Figure 4.17: Distribution of events in the S1 vs f_{90} plane from ^{241}Am^{13}C data. The NR events appear in the upper band with f_{90} of $\sim$0.7.

isotopes in the liquid scintillator. This process occurs in a very short time meanwhile the neutron lost part of its energy to the target nuclei, which dominates the lower part (<500 PE) and the higher part (>2000 PE) of the charge spectrum from ^{241}Am^{13}C data as shown in Figure 4.18. Eventually the neutrons get captured by ^{10}B, ^{12}C and ^{1}H. Besides neutrons, γ-rays, mostly from radioactive contamination in the detector materials, are also likely to leave signals in the NV. The red curve in Figure 4.18 shows signals from ^{60}Co (between 600 PE and 800 PE) and ^{232}Th (around 1400 PE).

Since the goal of the ^{241}Am^{13}C source is to study neutron thermalization signals in the prompt window, it is necessary to distinguish them from other potential backgrounds. Initially, we expected the neutron from the ^{241}Am^{13}C source go directly into the TPC before it thermalize in the NV, which is called "late prompt". However, in the data analysis, one interesting phenomenon is that the neutron has a relatively high probability to scatter in the NV after leaving the ^{241}Am^{13}C source. After scattering in the NV, the neutron goes into the TPC and deposits energy there. The energetic

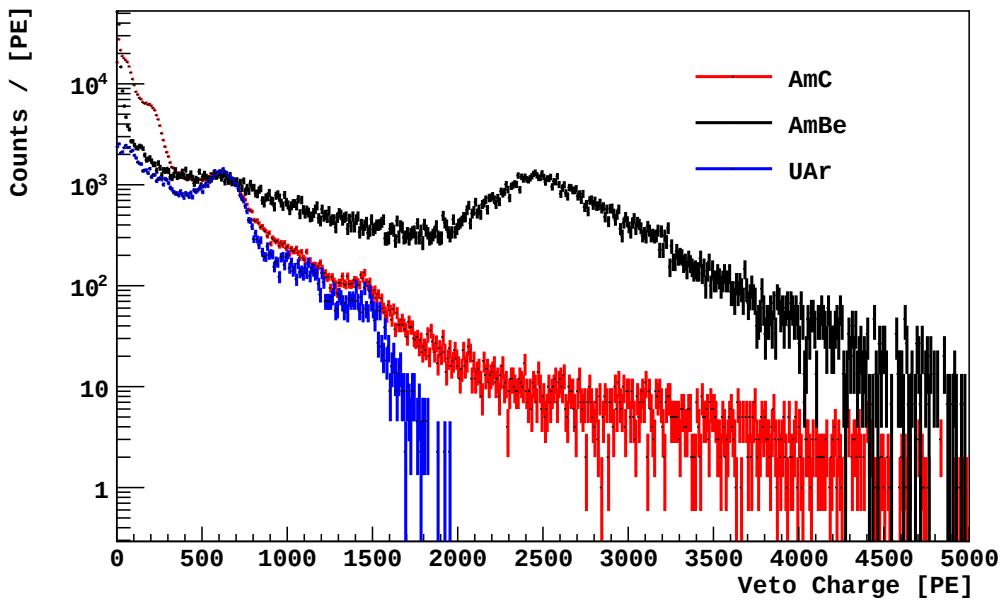

Figure 4.18: Comparison of the charge spectrum from ^{241}Am^{13}C, ^{241}Am^{9}Be and UAr data in the prompt window of the NV. All the spectra are normalized to the ^{60}Co peak at 600 PE. The charge spectrum from UAr (blue) data contains peaks from γ-rays emitted by ^{60}Co (600 PE) and ^{232}Th (1400 PE) decays. In ^{241}Am^{9}Be data, the spectrum (black) is dominated by 4.4 MeV γ-rays. By contrast, the neutron from ^{241}Am^{13}C contributes to the lower (<500 PE) and higher (>2000 PE) part of the charge spectrum (red).

neutron then leaves the TPC and interacts with particles in the NV. This process is called "early prompt". Figure 4.19 shows the cluster charge vs time distribution in the NV after requiring NR selections in TPC. The cluster that starts before -12.8 ns relative to TPC trigger time in Figure 4.19 is expected to be the early prompt while that occurs after -12.8 ns is the late prompt. The timestamp of -12.8 ns relative to TPC trigger time is determined by the time distribution of γ-rays from ^{60}Co decay. Because the two γ-rays from ^{60}Co decay appear in the TPC and NV approximately at the same time, the travel time of the γ-rays can be used to determine the time offset between the early and late prompt.

However, it is still difficult to separate the early and late prompt due to correlation. The neutron that thermalizes in the early prompt region can still leave signals in the

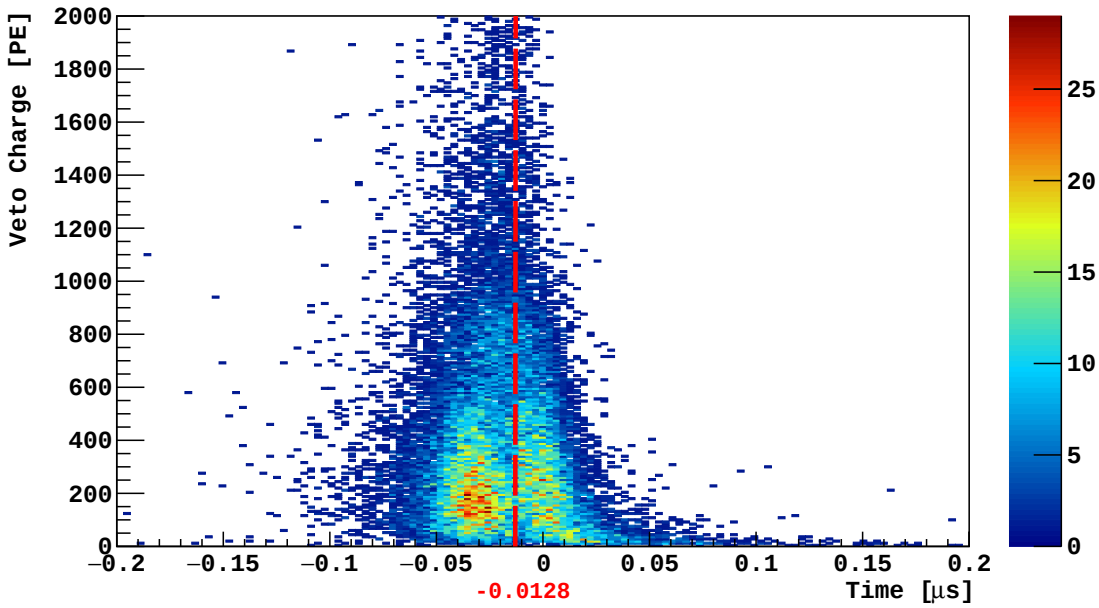

Figure 4.19: Distribution of events in the energy vs time plane in the prompt window of the NV. The selected events require NR scatterings in TPC. The time before −12.8 ns is the early prompt region while the late prompt region is afterwards.

NV after traveling through the TPC. In that case, the neutron produces signals in both the early and late prompt region. In fact, the early and late prompt signals overlap most of the time. Figure 4.20 shows the cluster charge spectrum for the early and late prompt samples. Although they look similar in most parts, there is an obvious difference in the low charge part. The spectrum is dominated by lower charge events in the late prompt samples because the neutron may have lost part of its energy in the TPC before producing signals in the NV. In contrast, the neutron in the early prompt sample has not lost any energy before scattering in the NV. In addition to the differences, there is a common peak between 700 PE and 800 PE due to the 1461 keV γ-rays from the decay of the first excited state of ^{40}Ar. The tail up to 2500 PE is mostly from other inelastic recoils in the detector materials.

In order to calculate the neutron veto efficiency based on the thermalization signals in the late prompt signals, it is necessary to separate them from the early prompt

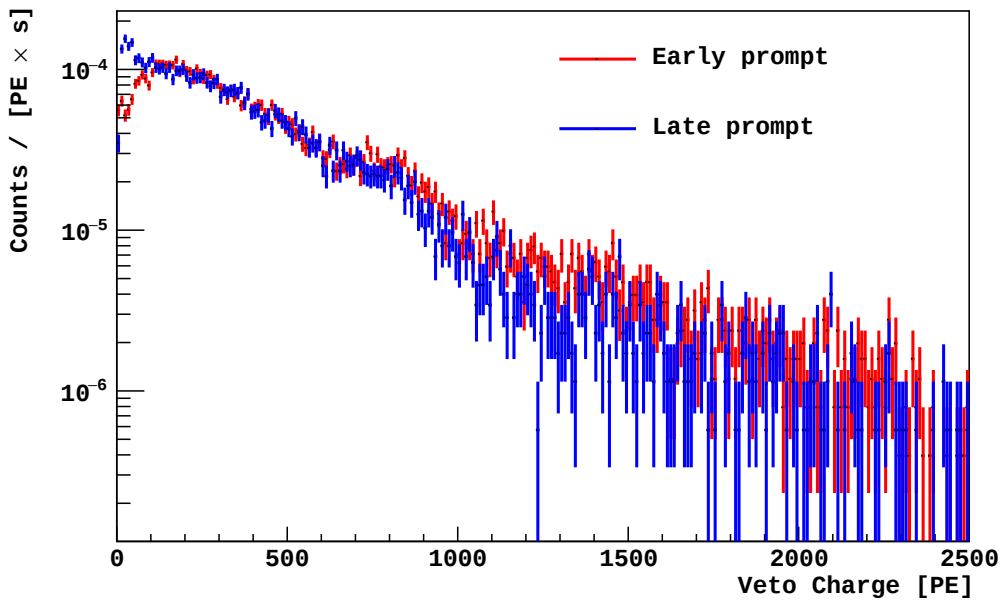

Figure 4.20: Comparison of the charge spectrum between the early and late prompt samples. The selected events require NR scatterings in TPC. The lower charge events dominate the spectrum in the late prompt samples compared with the early prompt samples.

signals. A new `ROI` variable is defined between -100 ns and 17 ns relative to the timestamp of -12.8 ns that described above. The charge distribution of this `ROI` is symmetric between -0.2 PE and 0.2 PE due to the noise or background events in the system, as shown in Figure 4.21. The charge increases to a high energy as long as other external radioactive sources, like ^{241}Am^{13}C, deposit energy in that window. The threshold was set at 0.2 PE to remove the events that have early prompt signals. The events with `ROI` charge smaller than 0.2 PE was selected as "the clean NR sample" (11749 events in total).

When the veto prompt cut was applied to the clean NR sample, 11574 out of 11749 total events were vetoed which gave a prompt veto efficiency of $98.50 \pm 0.11\,\%$ (denoted as ϵ(`ROI`, data)). In order to remove bias, a systematics study of the neutron veto efficiency using different `ROI` variables and thresholds was carried out. Besides this `ROI` variable, two more `ROI` variables were similarly defined at [-100 ns,10 ns] and

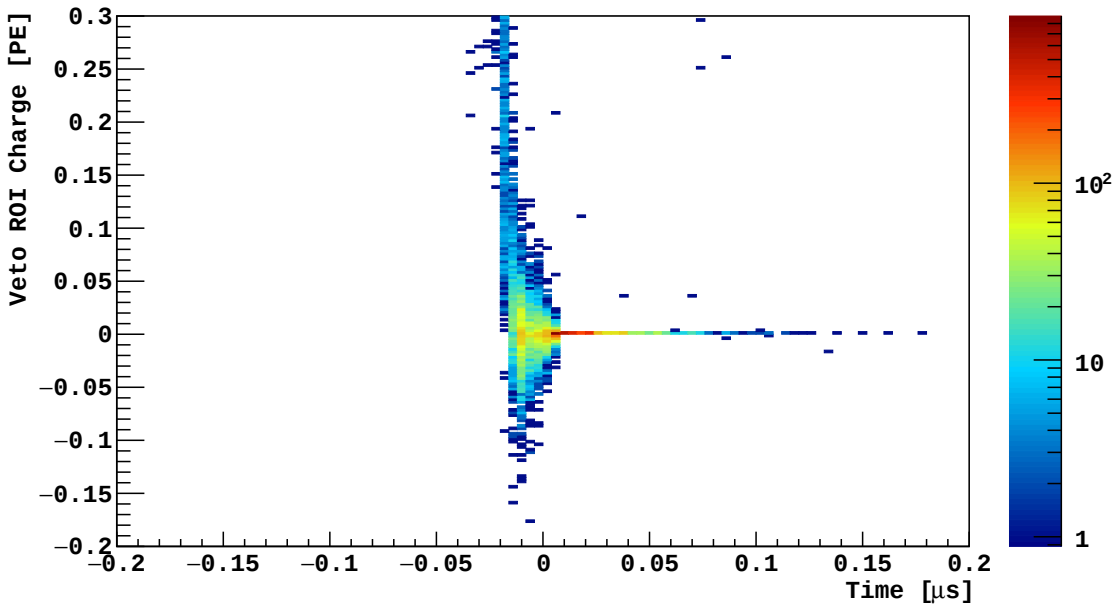

Figure 4.21: Distribution of ROI vs time from ^{241}Am^{13}C data. The ROI charge is symmetric between -0.2 PE and 0.2 PE. The ROI threshold is set at 0.2 PE to remove the events that have early prompt signals.

[-100 ns,20 ns]. The threshold of the ROI variables varied from 0.05 PE to 0.3 PE. In Figure 4.22, the prompt veto efficiency was consistent within 0.6 %.

In order to confirm the results of the 70-days analysis [37], the veto pre-prompt and delayed cuts along with the veto prompt cut were applied to the clean NR sample. Then 11663 out of 11749 total events were vetoed in ^{241}Am^{13}C data, which gave a total veto efficiency of 99.27 ± 0.08 %. Using the same ROIs as in the prompt cut for the systematics study, the total veto efficiency from the combination of all three veto cuts agree within 0.3 %, as shown in Figure 4.23.

4.2.3 Monte Carlo Tuning

After the ^{241}Am^{13}C calibration data analysis, this neutron source along with the source holder was implemented in MC to tune the simulation package used in DarkSide-50. Neutron events were simulated based on the angle and energy

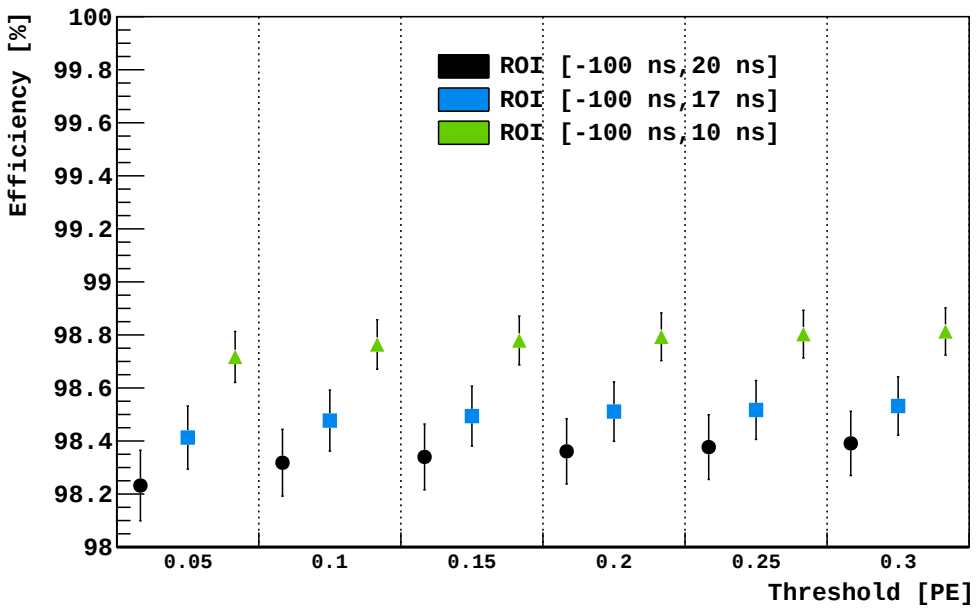

Figure 4.22: Systematics of the prompt veto efficiency from ^{241}Am^{13}C data. The efficiency is calculated based on each ROI threshold.

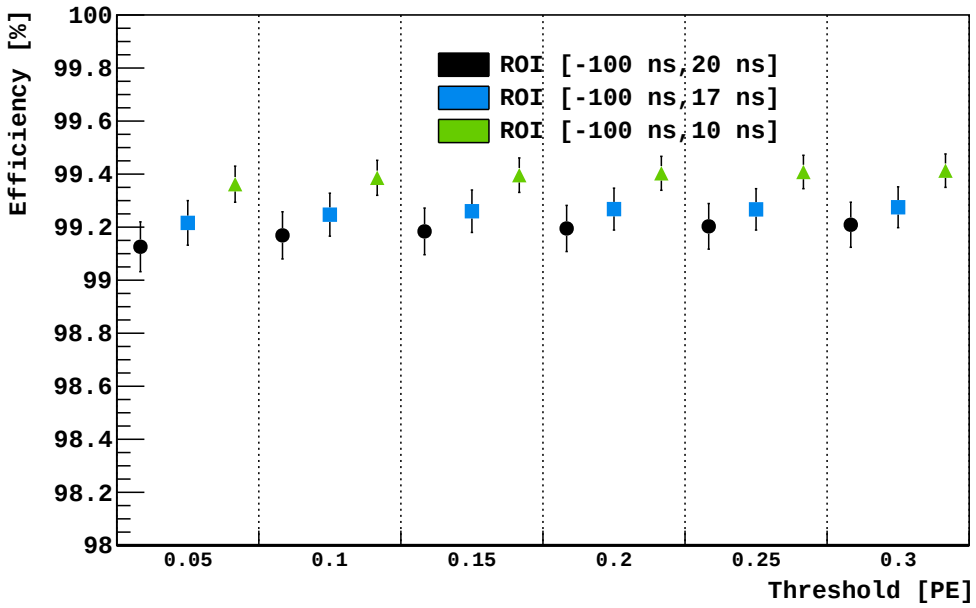

Figure 4.23: Systematics of the total veto efficiency from ^{241}Am^{13}C data. The efficiency is calculated based on each ROI threshold.

distribution of the ^{241}Am^{13}C neutron source in Figure 4.16. In order to mimic the event selections used in calibration data analysis, the variables in MC had to be corrected.

In TPC, the quenching factor for S1 is computed as the following equation:

$$\mathrm{QF(S1)} = Q_{\mathrm{nucl}} \times Q_{\mathrm{S1}}(E), \tag{4.6}$$

where Q_{nucl} is the Lindhard factor, which equals to 1 for the ER and 0.25 for the NR [64]. E is the energy of incident particle. $Q_{\mathrm{S1}}(E)$ is the equivalent quenching factor due to the splitting between excitions and ionization pairs along with the recombination probability [65]. The number of the photons generated for the S1 signals are:

$$N_{\mathrm{photons}} = \frac{N_q}{1+\alpha} \cdot (\alpha + \mathrm{Reco}(E)), \tag{4.7}$$

where N_q is the number of quanta obtained from E/W ($W = 19.5\,\mathrm{eV}$) [66]. Reco(E) is the recombination probability and α is the ratio of excition to ionization, which is 0.21 for ER and 1 for NR [66]. After dividing N_{photons} by N_q, the $Q_{\mathrm{S1}}(E)$ parameter becomes:

$$Q_{\mathrm{S1}}(E) = \frac{\alpha + \mathrm{Reco}(E)}{1+\alpha}, \tag{4.8}$$

The Reco(E) is extracted by fitting the DarkSide-10 data and the ^{39}Ar spectrum in DarkSide-50 [37]. The Reco(E) equation is:

$$\mathrm{Reco}(E) = p_0 \cdot (1 - p_1 \cdot e^{p_2 \cdot E}) \cdot e^{p_3 \cdot E^{p_4}} + p_5, \tag{4.9}$$

with E is in unit of keV, p_0=0.292, p_1=1.378, p_2=-0.155, p_3=-0.0147, p_4=0.9168 and p_5=0.6212 [65]. The multiplication of QF(S1) and the energy (E) is the corrected deposited energy, which can later be translated to the number of photoelectrons by multiplying a Poisson smearing and light yield of $7.91\,\mathrm{PE\,keV^{-1}}$ in liquid argon [37].

In the NV, the quenching factor of the liquid scintillator is usually characterized by the Birk's Law as described in Equation 2.12. However, it is not effective in describing the response of the scintillator. In particular, the α+^{7}Li peak in the neutron capture signal is heavily suppressed in the Birk's Model. In order to make up the effect, a quadratic term [67] is introduced as:

$$\frac{dL}{dx} = S \cdot \frac{\frac{dE}{dx}}{1 + kB \cdot \frac{dE}{dx} + C \cdot (\frac{dE}{dx})^2}. \tag{4.10}$$

where S is the scintillation efficiency, the Birk's constant (kB) is $8.56 \times 10^{-3}\,\mathrm{cm\,MeV^{-1}}$ and C is $3.5 \times 10^{-5}\,\mathrm{cm^2\,MeV^{-2}}$ based on the fit as shown in Figure 4.24. dE/dx is the energy loss of the incident particle per path length, which is computed based on the MC data. The quadratic model takes the energy deposition per step from MC as dE/dx. This quadratic model effectively reproduces the peaks from neutron capture signals from ^{10}B with χ^2/NDF of 1.36 as shown in Figure 4.24. The light yield is $0.5139 \pm 0.0012\,\mathrm{PE\,keV^{-1}}$ calculated by fitting the delayed neutron capture signals, as shown in Figure 4.24.

With the fitting parameters and quadratic model developed in the delayed neutron capture signals as shown in Figure 4.24, this model was then applied to the energy spectrum in the prompt window. However, the low energy peak around ~100 PE in the late prompt window, as shown in Figure 4.20, was missing in the Geant4 database. The γ-ray with energy of 197.143 keV from the second excited state of ^{19}F, in theory, should decay with a half-life of 89.3 ns. In Geant4, however, this γ-ray was generated instantaneously. In order to correct the decay time, the physics processes induced by neutron scattering off ^{19}F were identified. Then a random time offset from an exponential distribution with a constant of 89.3 ns was added to the deposition time of the electrons and γ-rays from the second excited state of ^{19}F.

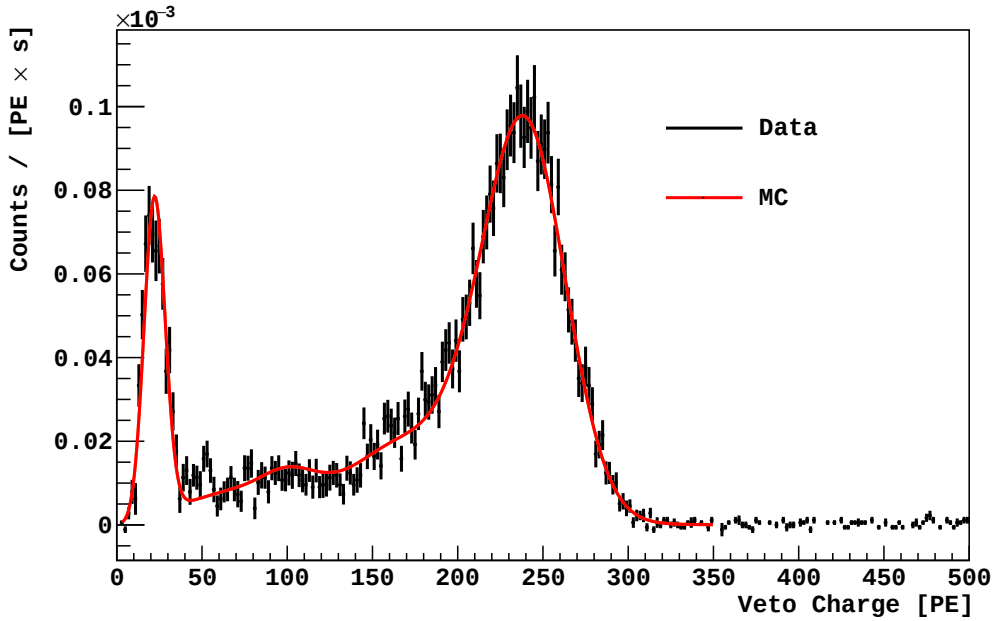

Figure 4.24: Comparison of the charge spectrum from neutron capture on ^{10}B between ^{241}Am^{13}C data and MC. The black curve is the background subtracted ^{10}B neutron capture spectrum from ^{241}Am^{13}C data. The red curve is the MC quadratic model fit to the data.

With the corrections, the simulated energy spectrum in the prompt window was used to fit the charge spectrum from the ^{241}Am^{13}C calibration data, which gave χ^2/NDF of 1.7 in Figure 4.25. Similarly, the simulated energy spectrum in the early and late prompt were also used to fit the corresponding charge spectrum in the ^{241}Am^{13}C data. The fit in early and late prompt window gave a respectively good χ^2/NDF of 1.67 in Figure 4.26 and 1.53 in Figure 4.27.

In addition to the tuning of the energy in MC, it is also necessary to correct the time distribution. Because only the time when a particle deposits energy in the detector is recorded in the simulation package. After the scintillation process, the photons travel through the detector and reflect on the surface of the materials, which is normally considered as Time of Flight (TOF) of the photons. The TOF was not included in MC but in the calibration data. In order to correct the time in MC, photons with energy of 50 eV were simulated uniformly in the liquid scintillator. The

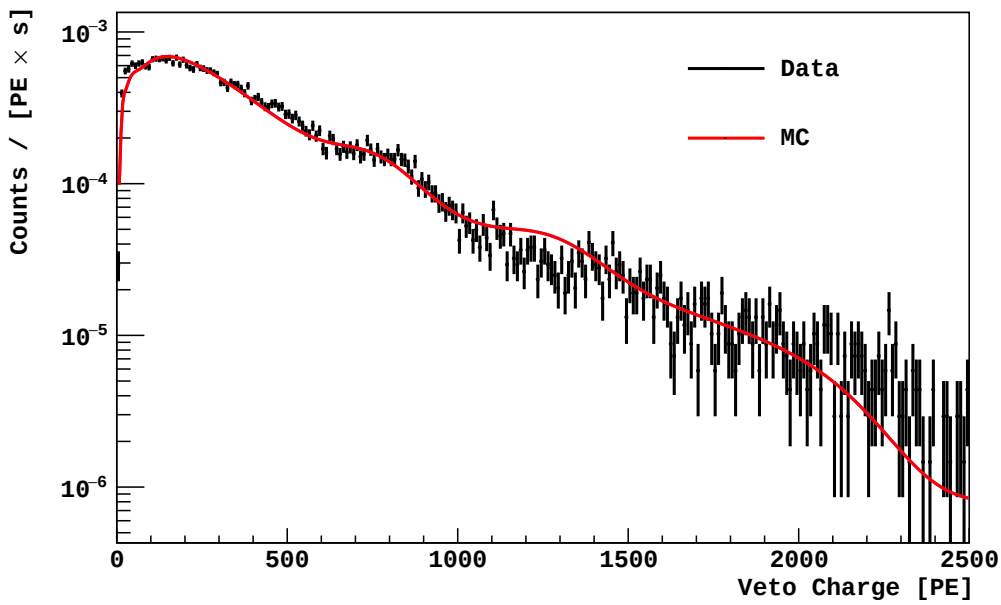

Figure 4.25: Comparison of the charge spectrum in the prompt window between ^{241}Am^{13}C data and MC. The black curve is the charge spectrum in the prompt window from ^{241}Am^{13}C data. The red curve is the MC quadratic model fit to the data.

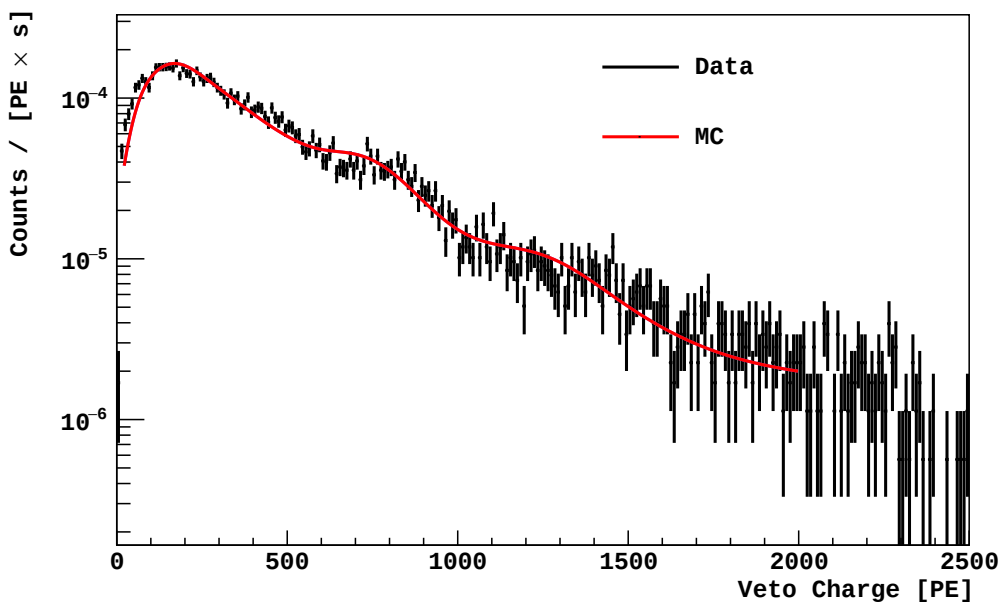

Figure 4.26: Comparison of the charge spectrum in the early prompt region between ^{241}Am^{13}C data and MC. The black curve is the charge spectrum in the early prompt region from ^{241}Am^{13}C data. The red curve is the MC quadratic model fit to the data.

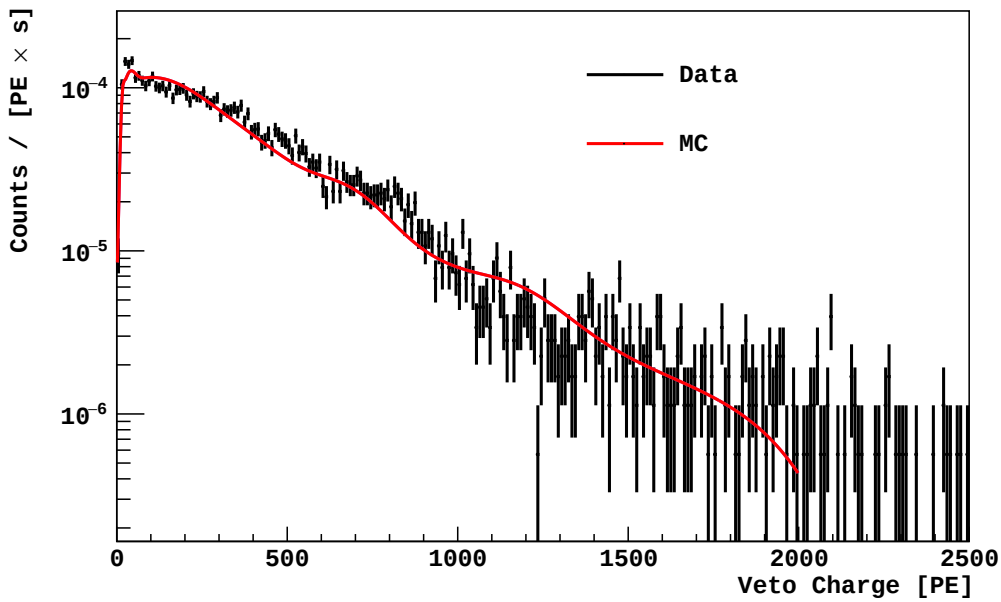

Figure 4.27: Comparison of the charge spectrum in the late prompt region between ^{241}Am^{13}C data and MC. The black curve is the charge spectrum in the late prompt region from ^{241}Am^{13}C data. The red curve is the MC quadratic model fit to the data.

TOF of the first photon detected by a PMT was recorded along with the start position of the photon. The TOF was later added to the deposition time of the particles based on the position.

Geant4 tracks the energy depositions in each step until the energy drops below a threshold. However, the steps may be too small to be distinguishable due to the limited resolution of the detector. It is necessary to merge the energy depositions in MC based on the resolution of the detector. If the position of the energy depositions in TPC are within 0.4 cm in z direction, they are merged into one cluster in MC. Due to the lack of position information in the NV data, the energy depositions can be merged together only when their time difference is less than 0.3 µs. The cluster start time is defined as the time of the first deposition in the cluster. The energy of the cluster is the sum of the quenched energy of the depositions. The cluster can be mixed with energy depositions from ER and NR. In the TPC, the fraction of the

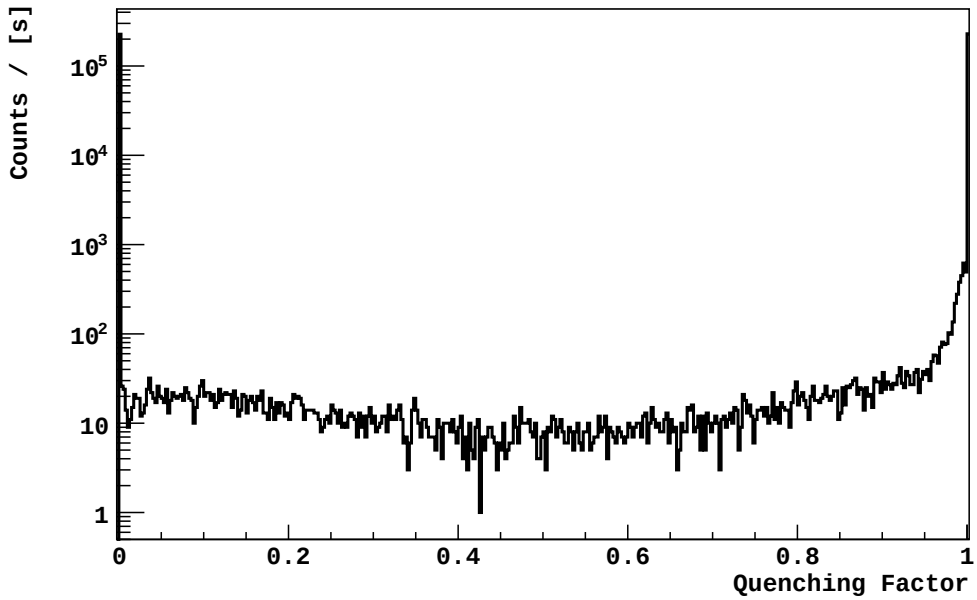

Figure 4.28: Distribution of the quenching factor in the TPC. The quenching factor that mimics the PSD in the TPC represents the fraction of energy depositions from NR in a cluster. The quenching factor of ER sits in the lower region while that of NR is in the higher region. The quenching factor of 0.8 is set to distinguish the NR from the ER in MC.

energy depositions that come from NR in a cluster is used to separate the neutron-like clusters from electron-like clusters. The fraction called as "quenching factor" mimics the PSD in the TPC calibration data analysis. The quenching factor larger than 0.8 is set to select a NR event in MC as shown in Figure 4.28.

The ^{60}Co was simulated in the TPC cryostat to determine the actual veto prompt time. The γ-rays from ^{60}Co travel through the detector and leave signals in both the TPC and NV almost simultaneously. In MC, the average time of γ-rays from ^{60}Co traveling from the cryostat through the TPC to the NV is 13.96 ns. In MC, the veto cluster time is then shifted by that amount. Figure 4.29 shows the agreement of the time distribution in the prompt window after correction between ^{241}Am^{13}C data and MC.

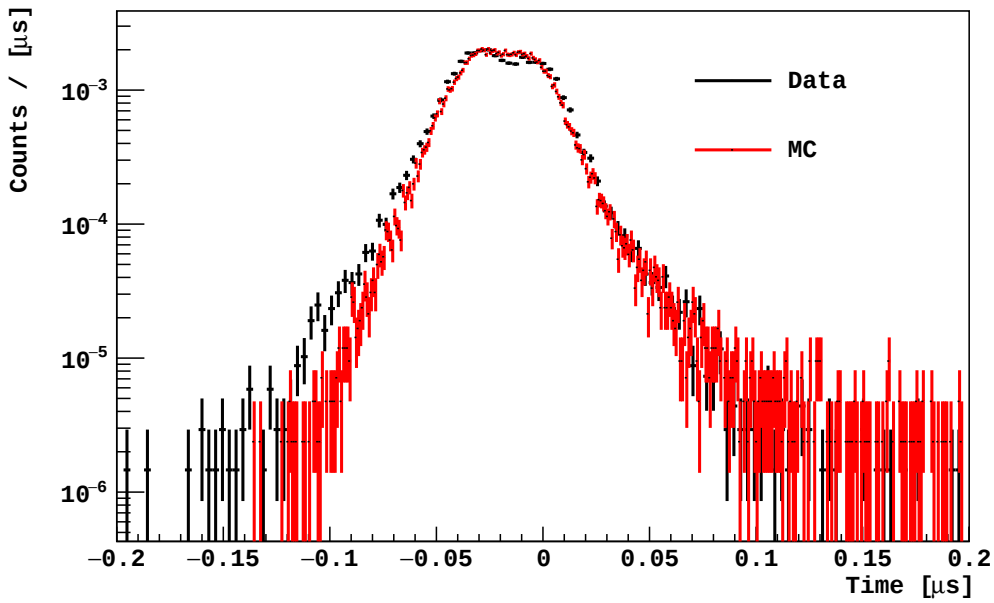

Figure 4.29: The time distribution in the prompt window from ^{241}Am^{13}C data and MC.

4.2.4 Veto Efficiency

With the energy and time corrections in MC complete, it is possible to get the prompt veto efficiency from the ^{241}Am^{13}C MC. The `ROI` variables were implemented as those used in the ^{241}Am^{13}C calibration data. Applying the same energy threshold of `ROI` as used in data, a fraction of events that had early prompt signals were removed so that the rest were considered as the clean NR sample. The veto prompt cut was then applied to the clean NR sample in order to calculate the prompt veto efficiency in ^{241}Am^{13}C MC, as shown in Figure 4.30. There is also a systematic effect in the efficiency due to the application of different `ROI` variables and thresholds.

With the position and time information of the depositions in MC, it is relatively easy to separate the early and late prompt signals without the `ROI` variables. The prompt veto efficiency in MC without `ROI` variables is $99.309 \pm 0.042\,\%$, which is denoted as ϵ(MC). The prompt veto efficiency based on `ROI` variables in ^{241}Am^{13}C data (Figure 4.22) is ϵ(`ROI`, data) while that from ^{241}Am^{13}C MC in Figure 4.30 is

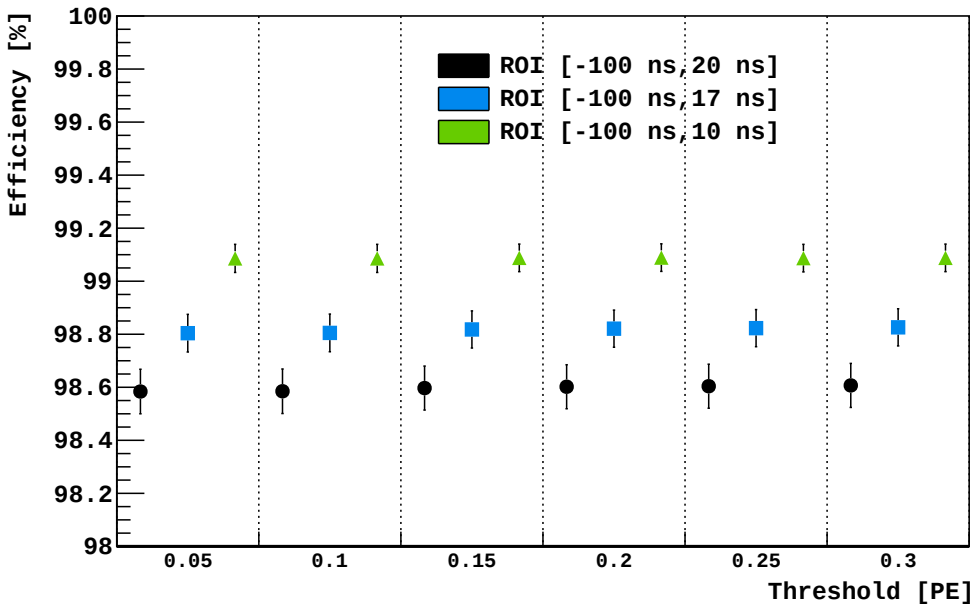

Figure 4.30: Systematics of the prompt veto efficiency from ^{241}Am^{13}C MC. The efficiency is calculated based on each ROI threshold.

ϵ(ROI, MC). The corrected prompt veto efficiency for data (ϵ(data)) becomes:

$$\epsilon(\text{data}) = \epsilon(\text{MC}) \cdot \frac{\epsilon(\texttt{ROI}, \text{data})}{\epsilon(\texttt{ROI}, \text{MC})}, \tag{4.11}$$

while the uncertainty of ϵ(data) can be derived as:

$$\left(\frac{\delta\epsilon(\text{data})}{\epsilon(\text{data})}\right)^2 = \left(\frac{\delta\epsilon(\text{MC})}{\epsilon(\text{MC})}\right)^2 + \left(\frac{\delta\epsilon(\texttt{ROI}, \text{data})}{\epsilon(\texttt{ROI}, \text{data})}\right)^2 + \left(\frac{\delta\epsilon(\texttt{ROI}, \text{MC})}{\epsilon(\texttt{ROI}, \text{MC})}\right)^2. \tag{4.12}$$

The corrected prompt veto efficiency for ^{241}Am^{13}C data is 98.92% ± 0.14%(stat) ± 0.04%(sys).

4.3 Radiogenic Neutron Background

Neutron can leave WIMP-like signals in the TPC by scattering with argon nuclei. It becomes difficult to separate the neutron from WIMP events. In addition, neutron

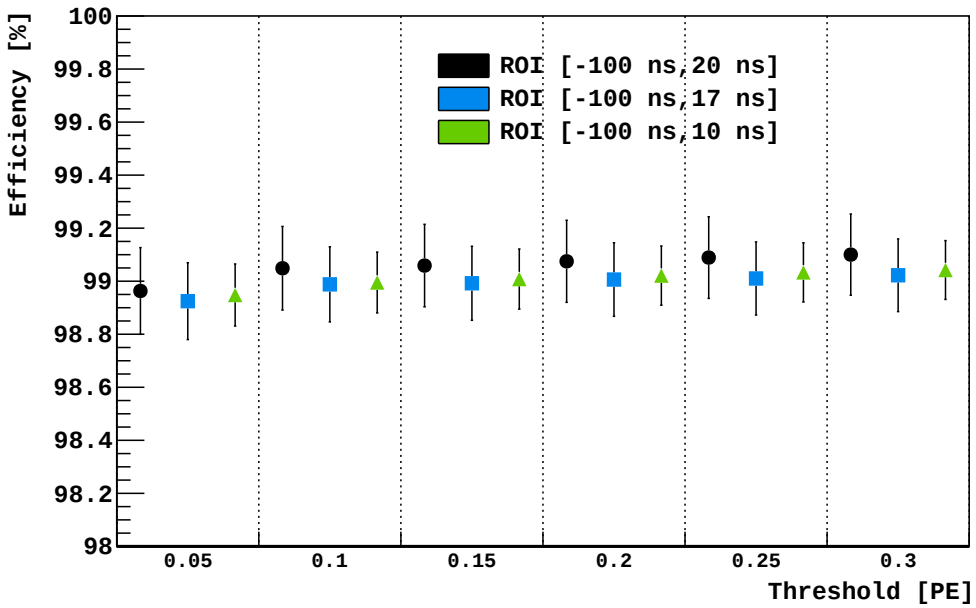

Figure 4.31: Systematics of the corrected prompt veto efficiency from ^{241}Am^{13}C data. The efficiency is calculated based on each `ROI` threshold.

has higher cross section than the WIMPs so that even a small fraction of neutrons can disguise a potential WIMP signal. Neutron emitted by the detector materials that are close to the sensitive volume of the TPC can pose a serious background for a dark matter experiment. It is essential to figure out the sources, the activity, and the methods to suppress or eliminate the neutron background.

There are three primary neutron sources: cosmogenic, fission, and (α,n) reactions. In this dissertation, my work focuses on the (α,n) neutron background. Radiogenic neutrons are the products of (α,n) reaction typically in a decay chain that emits α particles. In DarkSide-50, the ^{232}Th, ^{235}U, and ^{238}U chains are the main sources of the radiogenic neutrons. The neutron yield of this reaction is usually in the magnitude of 10^{-6} per α decay. The number of neutrons expected from a material depends on the activity of the radioactive sources and the energy of α particles emitted.

4.3.1 Radiogenic Neutron Rate

Although there are some standard packages to calculate the (α,n) yield, they are limited in application because the α energy in those tools is only up to 6.5 MeV. One big part of Shawn Westerdale's dissertation [47] is the implementation of a new (α,n) yield calculator called NeuCBOT (Neutron Calculator Based On TALYS) [68], which includes the α energy up to 10 MeV. This tool is based on TALYS package [69] which uses the TENDL database to combine nuclear models with data from Japanese Evaluated Nuclear Data Library (JENDL) [70] and the Evaluated Nuclear Data File (ENDF/B-VII.1) [71]. In my dissertation, I use this calculator to study the radiogenic neutron background and calculate the neutron veto efficiency of DarkSide-50.

The radioactive sources with non-negligible activities in the DarkSide-50 detector are the ^{232}Th, ^{235}U, and ^{238}U decay chains including the lower and upper decay chain of ^{238}U. In order to determine the (α,n) neutron rate expected in the experiment, the neutron yield of these sources are computed by NeucBOT, which accounts for the mass of the isotopes in the material, the cross section of (α,n) reaction, and the mass stopping power of the α in the target. For a material that contains multiple isotopes, the (α,n) yield is scaled by the mass fraction of the isotopes in the compound material. Table 4.6 lists the measured source activity of the radioactive source from different materials in the detector. Apparently, there are three dominant materials that produce radiogenic neutron background, which are the cryostat flange mainly due to the Viton o-ring, the ceramic in PMTs, and the borosilicate glass stems in the PMTs. The high (α,n) yield of fluorine in the Viton o-ring contributes to the neutron background. The aluminum and oxygen account for most of the mass of PMT creamic. The main contamination in the borosilicate glass comes from boron. In addition, the PMT hardware, cryostat walls, MultiLayer Insulation (MLI) also give sub-dominant neutron activities. At last, the neutron rate from each material is scaled by the mass

or the number of PMTs and summed over from different radioactive sources. In this study, the neutron rate is estimated from these materials.

Even though the source activity listed in Table 4.6 based on material counting results are comprehensive, the value for the TPC materials used in my calculation of the radiogenic neutron rate is actually calculated by fitting the γ-rays in the energy spectrum from TPC in Table 4.7 [72]. The γ-rays from the radioactive isotopes were generated at different positions in the detector. With the optical tuning and quenching model, the γ-ray spectrum in MC is then converted into the distribution of photoelectron. After applying the geometrical effects and the light yield in TPC, the γ-ray spectrum in MC is used to match the energy spectrum in TPC from UAr data via χ^2 minimization with details in Paolo Agnes's dissertation [73].

4.3.2 Event Reconstruction

Besides the neutron rate, it is necessary to calculate the probability that neutron survive certain cuts in order to predict the number of neutron events in the detector and give the neutron veto efficiency. For a neutron to pass all the TPC cuts, it has to reach the TPC active volume and within the TPC fiducial volume, leave single NR scattering signals in the TPC. In addition, once the neutron survives all the TPC cuts, it has to pass the veto prompt, preprompt and delayed cuts in order to contribute to the counting of radiogenic neutron background. In order to simulate these cuts, the MC simulation package is inherited from the one tuned based on the results from ^{241}Am^{13}C data. The correction of the energy and time in MC was described in Section 4.2.3.

In MC, the TPC active volume is a cylinder with a radius of 17.77 cm and z position from -21.44 cm to 14.31 cm in the NV coordinate system. It is defined to remove the potential events from the surface background due to α particles. Furthermore, the TPC fiducial volume is a smaller cylinder with a radius of 10 cm and z position

Table 4.6: Measured activity (with unit of Bq/kg or Bq/PMT) of radiogenic neutron source from different materials of the detector (Table from Ref. [47])

Component	**^{238}U upper**	**^{238}U lower**	**^{235}U**	**^{232}Th**	**^{210}Pb**
Cryostat	$(2.47\pm1.24)\times10^{-3}$	$(4.00\pm2.00)\times10^{-4}$	$(1.02\pm0.51)\times10^{-4}$	$(8.00\pm3.00)\times10^{-4}$	
Flange	$(1.20\pm1.20)\times10^{-2}$	$(1.20\pm1.20)\times10^{-2}$	$(5.10\pm5.10)\times10^{-4}$	$(8.00\pm4.00)\times10^{-4}$	
Bolts	0.050 ± 0.012	0.002 ± 0.001	0.002 ± 0.001	0.017 ± 0.001	
Nuts	0.037 ± 0.012	0.037 ± 0.012	0.002 ± 0.001	0.033 ± 0.004	
Washers	0.012 ± 0.012	0.004 ± 0.002	0.001 ± 0.001	0.0174 ± 0.0017	
Tubes	0.1 ± 0.0	0.002 ± 0.001	0.005 ± 0.000	0.003 ± 0.000	
O-ring	0.206 ± 0.012	0.206 ± 0.012	0.010 ± 0.001	0.044 ± 0.003	
Grid	$(1.23\pm0.00)\times10^{-3}$	$(1.23\pm0.00)\times10^{-3}$	$(5.10\pm0.00)\times10^{-5}$	$(1.600\pm0.407)\times10^{-3}$	$(7.00\pm1.00)\times10^{-6}$
Grid Support Ring	$(2.47\pm1.24)\times10^{-3}$	$(4.00\pm2.00)\times10^{-4}$	$(1.020\pm0.510)\times10^{-5}$	$(8.00\pm3.00)\times10^{-4}$	
Reflector	$(2.84\pm0.00)\times10^{-5}$	$(2.84\pm0.00)\times10^{-5}$	$(1.17\pm0.00)\times10^{-6}$	$(4.88\pm0.00)\times10^{-6}$	
mounts	$(7.29\pm0.00)\times10^{-5}$	$(7.29\pm0.00)\times10^{-5}$	$(3.01\pm0.00)\times10^{-6}$	$(4.07\pm0.00)\times10^{-6}$	
Cathode+Diving Bell	$(5.20\pm0.00)\times10^{-5}$	$(5.20\pm0.00)\times10^{-5}$	$(2.10\pm0.00)\times10^{-6}$	$(1.06\pm0.00)\times10^{-5}$	
Field Cage	$(1.15\pm0.00)\times10^{-3}$	$(1.15\pm0.00)\times10^{-3}$	$(5.00\pm0.00)\times10^{-5}$	$(4.00\pm0.00)\times10^{-4}$	
Resistors	$(2.20\pm0.70)\times10^{-5}$	$(1.64\pm0.14)\times10^{-5}$	$(1.30\pm0.50)\times10^{-6}$	$(8.000\pm0.943)\times10^{-6}$	$(2.10\pm0.30)\times10^{-4}$
PMT stem	0.151 ± 0.022	0.018 ± 0.001	0.007 ± 0.001	0.006 ± 0.001	
Kovar	$(1.23\pm0.00)\times10^{-4}$	$(1.23\pm0.00)\times10^{-4}$	$(5.70\pm0.00)\times10^{-6}$	$(4.10\pm0.00)\times10^{-5}$	
PMT screws	$(1.20\pm0.00)\times10^{-6}$	$(1.20\pm0.00)\times10^{-6}$	$(5.10\pm0.00)\times10^{-8}$	$(4.00\pm0.00)\times10^{-7}$	
PMT Resistors	5.3 ± 0.6	0.27 ± 0.04	0.19 ± 0.03	0.12 ± 0.00	14 ± 1
PMT Ceramic	7.0 ± 4.0	4.0 ± 2.0	0.08 ± 0.04	0.8 ± 0.1	1 ± 0
PMT PCB	$(1.60\pm0.00)\times10^{-4}$	$(3.44\pm0.46)\times10^{-5}$	$(1.00\pm0.00)\times10^{-5}$	$(1.10\pm0.00)\times10^{-5}$	
PMT Barrel Conn	$(6.17\pm0.00)\times10^{-4}$	$(6.17\pm0.00)\times10^{-4}$	$(2.55\pm0.00)\times10^{-5}$	$(2.04\pm0.00)\times10^{-4}$	
PMT Solder	$(1.24\pm0.00)\times10^{-2}$	$(1.24\pm0.00)\times10^{-2}$	$(5.10\pm0.00)\times10^{-4}$	$(4.01\pm0.00)\times10^{-3}$	
Cold Amp Circuitry	$(1.80\pm0.90)\times10^{-1}$	$(3.00\pm0.22)\times10^{-1}$	$(3.30\pm0.70)\times10^{-2}$	$(1.13\pm0.09)\times10^{-1}$	14 ± 1
Cold Amp MCX Male	$(1.80\pm0.90)\times10^{-1}$	$(4.60\pm0.80)\times10^{-2}$	$(1.20\pm0.00)\times10^{-2}$	$(1.80\pm0.70)\times10^{-3}$	11 ± 1
Cold Amp PCB	$(1.60\pm0.00)\times10^{-4}$	$(3.44\pm0.46)\times10^{-5}$	$(1.00\pm0.00)\times10^{-5}$	$(1.10\pm0.00)\times10^{-5}$	
Cold Amp MCX Female	$(3.91\pm1.09)\times10^{-1}$	$(1.10\pm0.50)\times10^{-2}$	$(1.80\pm0.50)\times10^{-2}$	$(1.50\pm0.00)\times10^{-2}$	8 ± 1
MLI Bulk	$(9.26\pm2.78)\times10^{-2}$	$(9.26\pm2.78)\times10^{-2}$	$(3.82\pm1.15)\times10^{-3}$	$(3.61\pm1.08)\times10^{-3}$	
MLI Aluminum Layer	$(6.17\pm1.85)\times10^{-2}$	$(6.17\pm1.85)\times10^{-2}$	$(2.55\pm0.76)\times10^{-3}$	$(2.41\pm0.00)\times10^{-2}$	
MLI Netting	$(8.03\pm2.41)\times10^{-4}$	$(8.03\pm2.41)\times10^{-4}$	$(3.31\pm0.99)\times10^{-5}$	$(1.08\pm0.32)\times10^{-4}$	

Table 4.7: Source activity from the γ-ray spectrum fitting in TPC. Total is the sum of the source activity of each isotope. The materials include PMT ceramic, PMT stem, and Kovar.

Source	**Total** [Bq/PMT]	**PMT Ceramic** [Bq/PMT]	**PMT Stem** [Bq/PMT]	**Kovar** [Bq/PMT]
^{232}Th	0.291	0.0873	0.2037	0
^{60}Co	0.171	0	0	0.171
^{40}K	2.833	0.5666	2.2664	0
^{238}U lower	0.85	0.425	0.425	0
^{238}U upper	3.419	2.7352	0.6838	0
^{235}U	0.159	0.1272	0.0318	0

from -17.81 cm to 10.68 cm. The quenching factor that mimics the PSD in the TPC, as described in Section 4.2.3 is used to distinguish the NR from the ER. For a NR event, the quenching factor has to be larger than 0.8 in MC as shown in Figure 4.28, which is the NR cut. The x axis on the top and bottom in Figure 4.32 shows the NR energy and the corresponding S1. The conversion from NR energy to S1 is based on the results from SCENE experiment. In order to simulate the WIMP search region, the NR acceptance based on f_{90} as shown in Figure 4.32, is applied to the MC events. A MC event is taken only if a random value from a uniform distribution is less than corresponding f_{90} NR acceptance at the same S1. When the S1 is smaller than 40 PE, the PSD cut has 0 % NR acceptance. As the S1 increases from 40 PE to 95 PE, the acceptance increases almost linearly from 0 % to 90 %. Above 95 PE, the acceptance is approximately constant at 90 %. Within the WIMP search region, the S1 only extends to 460 PE so that all events above that threshold are rejected. All TPC cuts are the combination of the TPC active volume cut, the TPC fiducial volume cut, single recoil cut, the NR cut, S1 energy region, and the f_{90} NR acceptance. The number of events that survive all TPC cuts is recorded as the counting of the radiogenic neutron background residual in the WIMP search region.

While in the NV, the energy and time distribution are tuned as we did in ^{241}Am^{13}C MC study with details in Section 4.2.3. The veto cuts used in data analysis as

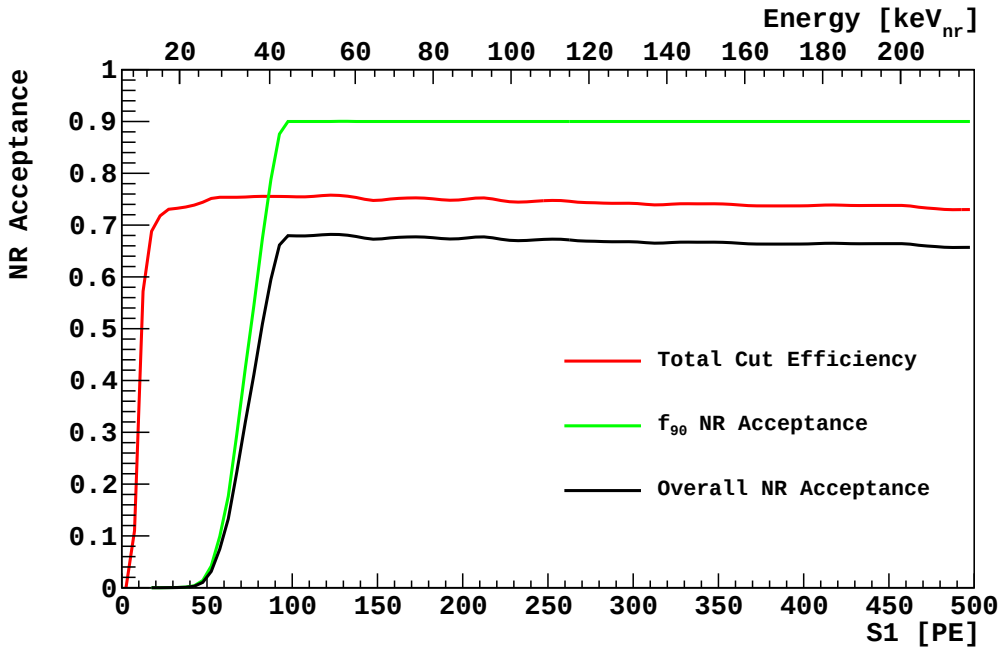

Figure 4.32: Combined acceptance of all TPC and veto cuts (red), acceptance of the f_{90} cut (green) and the final cumulative NR acceptance in UAr data (black) (Plot from Ref. [30]). The f_{90} NR acceptance along with S1 from 0 PE to 460 PE is used to simulate the WIMP search region.

described in Section 3.3 are simulated in order to reject events in coincidence with the TPC. In addition, individual veto cut is applied to the events that survive all TPC cuts in order to calculate the corresponding veto efficiency.

4.3.3 Neutron Surviving Probability

The neutrons with energies from 0 MeV to 10 MeV, which covers almost the entire radiogenic neutron energy range, are simulated uniformly and separately at the PMT stem, PMT ceramic, cryostat walls that exclude the flanges, and inner and outer flange. The PMT hardware shares the neutron surviving probability distribution with the PMT stems since they are at the same position. This is also applicable to the MLI, which is located at the cryostat walls. The event reconstruction and the cuts described above were applied to the simulated neutron events in order to get the probability of surviving neutron.

In Figure 4.33, the plot on the top is the probability of neutrons generated in PMT stems after passing certain cut. The total number of the simulated neutron events (that is All in Figure 4.33) is normalized to 1. The probability of the neutrons passing a cut is the ratio of the number of the surviving neutron events to the total number of simulated neutron events. In Figure 4.33, "all neutrons", "pass TPC active volume", "pass TPC fiducial volume", "pass NR cut", "pass SNR cut", and "pass all TPC cuts" are applied accumulatively. The veto cut in Figure 4.33 is applied to the events pass all TPC cuts. "pass veto prompt cut" and "pass veto delayed cut" is applied separately while "pass all veto cuts" include the veto preprompt, prompt, and delayed cut.

As shown in Figure 4.33, all TPC cuts significantly reduces the surviving probability for neutron with energy below 1000 keV. While at higher energy, the probability is approximately on the order of 10^{-2}, which decreases even more as the energy increases. The higher energy neutrons are more likely to excite the nuclei of the target, which may produce γ-rays that can mix ER and NR in an event. The rejection power of all TPC cuts varies as the material that the neutron generated from. It is on the level of 10^2 at PMT stem while it is $\sim$10 times higher at outer flange. The neutron from PMT stem that is close to the TPC is more likely to leave signals in the TPC. Compared with PMT stem, outer flange is further away from the TPC so that neutron needs to travel a long distance before reaching the TPC. The TPC active volume cut is powerful to reject the neutron generated from outer flange.

Furthermore, even if some neutrons survived all TPC cuts, the veto prompt cut can highly suppress these events by a factor of $\sim$100. With all TPC cuts and veto prompt cut, the surviving probability is reduced to the level between 10^{-5} and 10^{-4}. The rejection power of the veto prompt cut varies as the neutron energy. In particular, the rejection power decreases when the neutron energy is between 1 MeV and 3 MeV due to the threshold of the prompt cut, which is a fixed value of 1PE. The energy

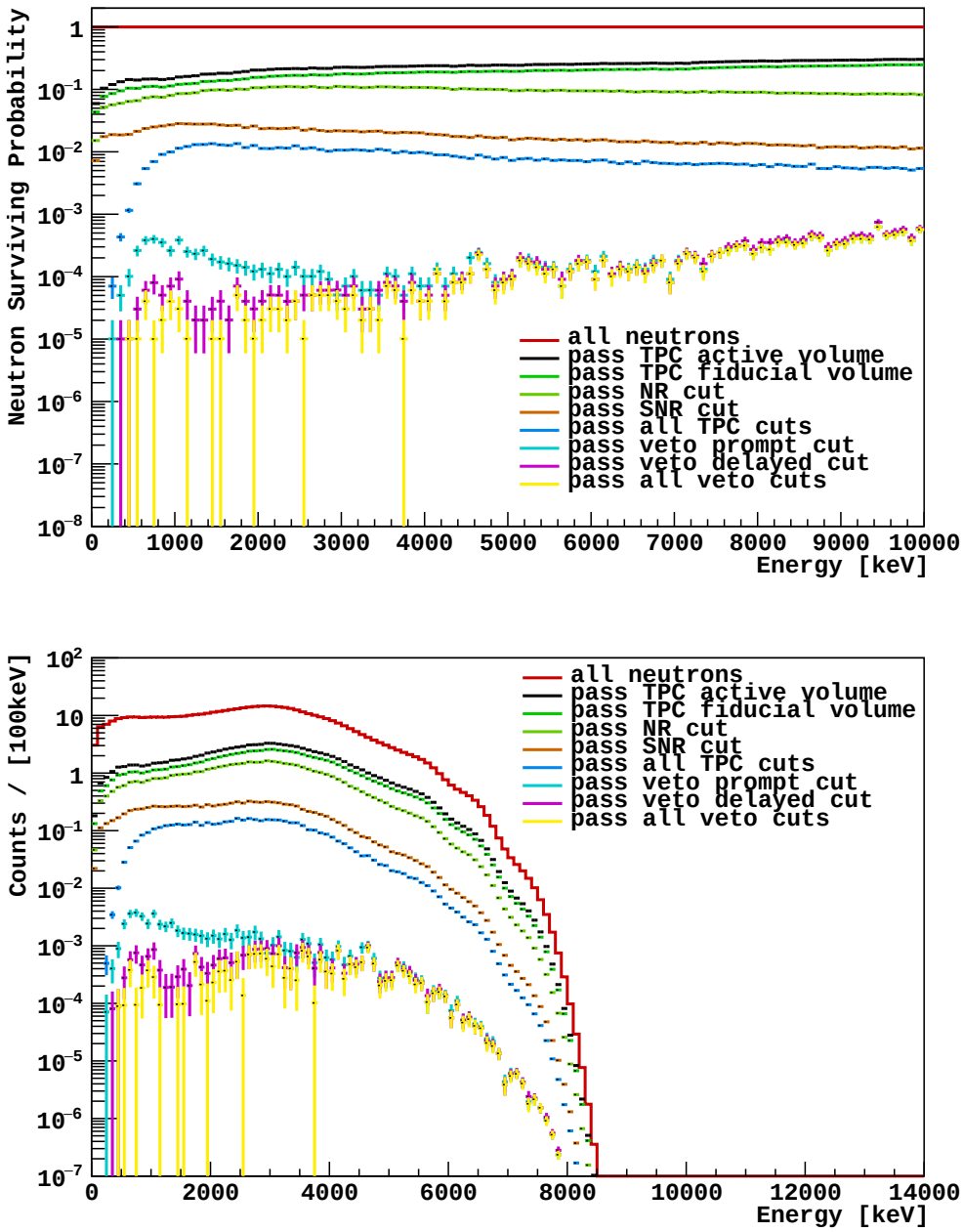

Figure 4.33: Neutrons from PMT stem. The cut is applied accumulatively. See text for the interpretation and discussion. Top: Probability of neutron passing the TPC and NV cuts. Bottom: Expected number of neutrons in one year passing the TPC and NV cuts.

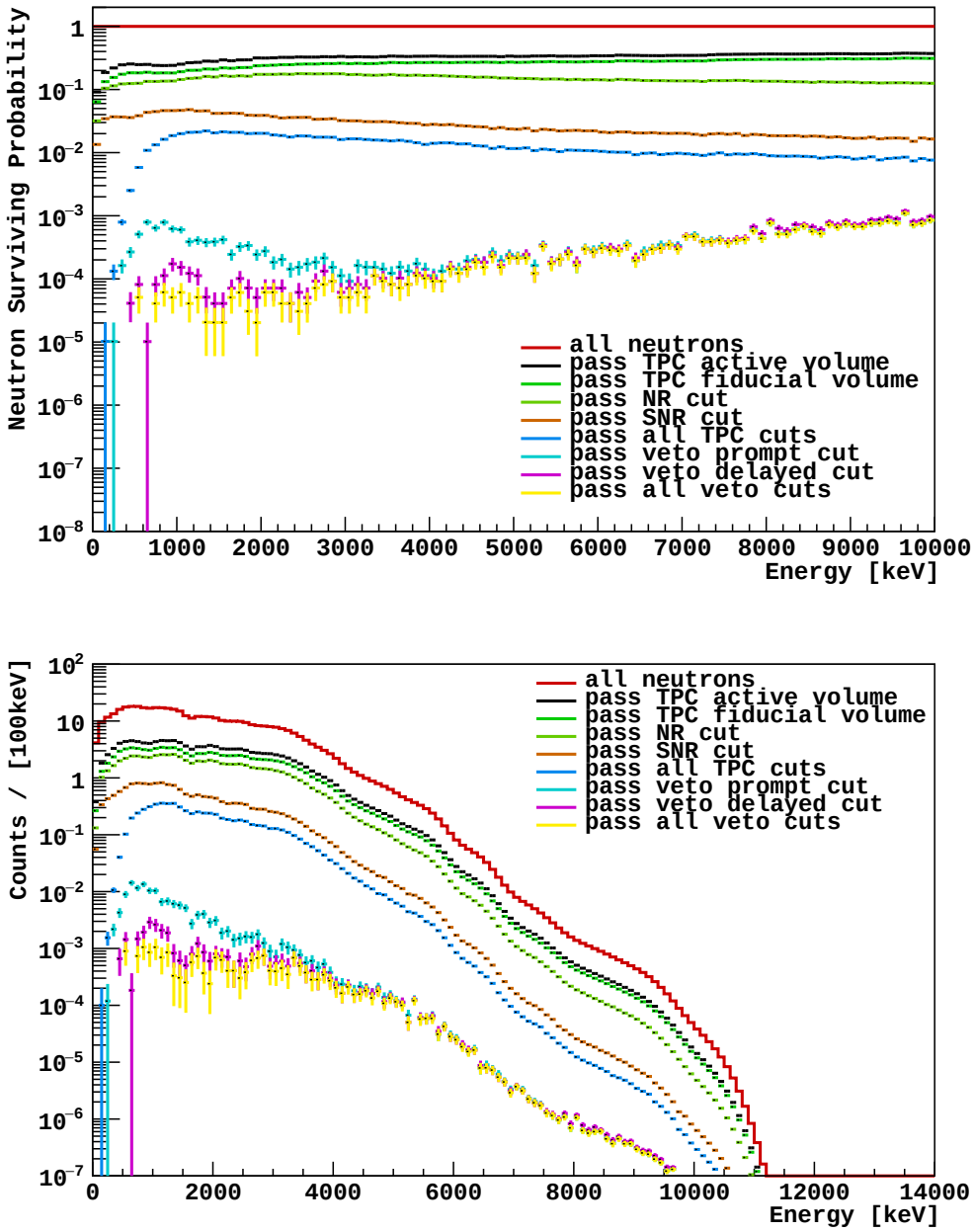

Figure 4.34: Neutrons from PMT ceramic. The cut is applied accumulatively. See text for the interpretation and discussion. Top: Probability of neutron passing the TPC and NV cuts. Bottom: Expected number of neutrons in one year passing the TPC and NV cuts.

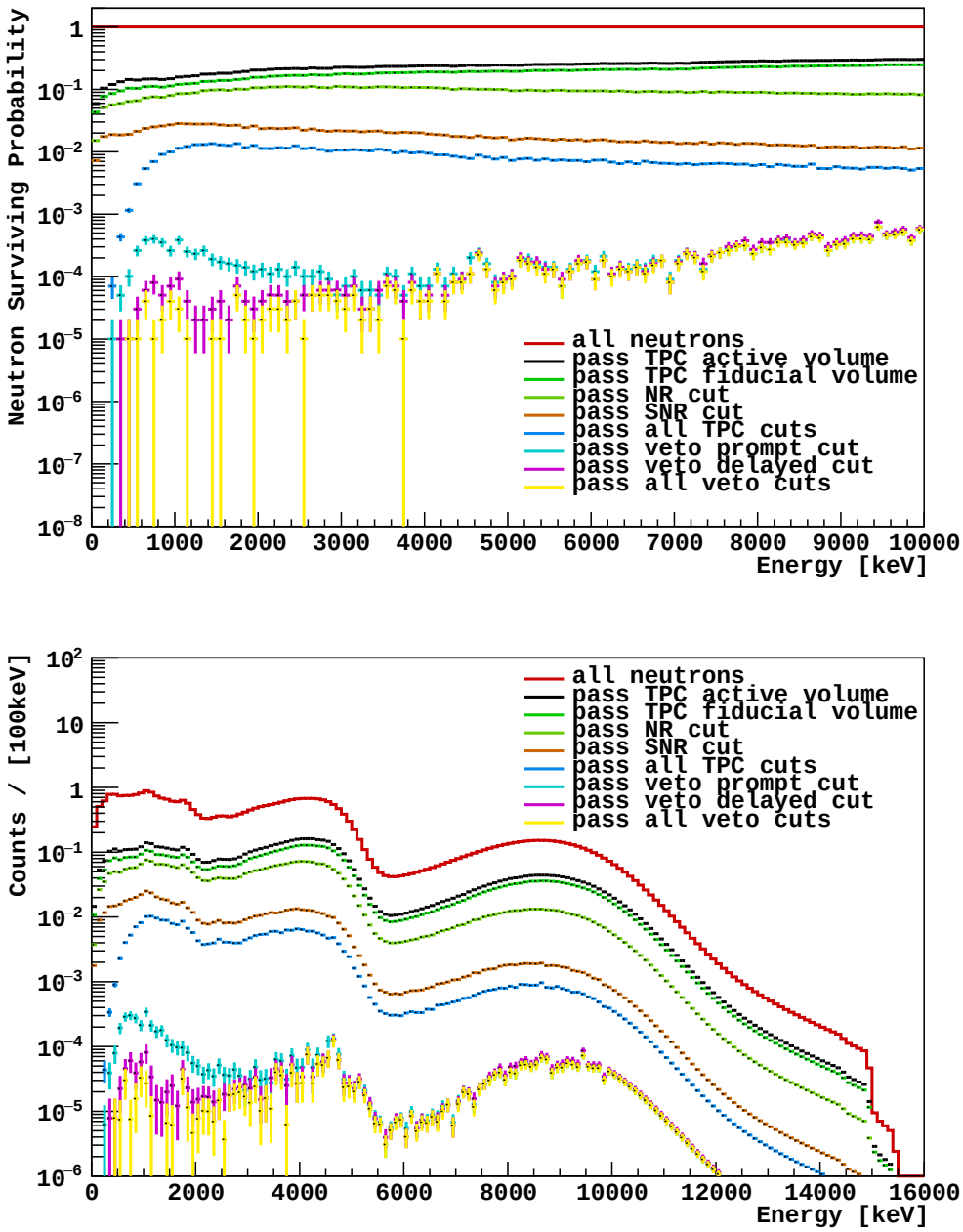

Figure 4.35: Neutrons from PMT hardware. The cut is applied accumulatively. See text for the interpretation and discussion. Top: Probability of neutron passing the TPC and NV cuts. Bottom: Expected number of neutrons in one year passing the TPC and NV cuts.

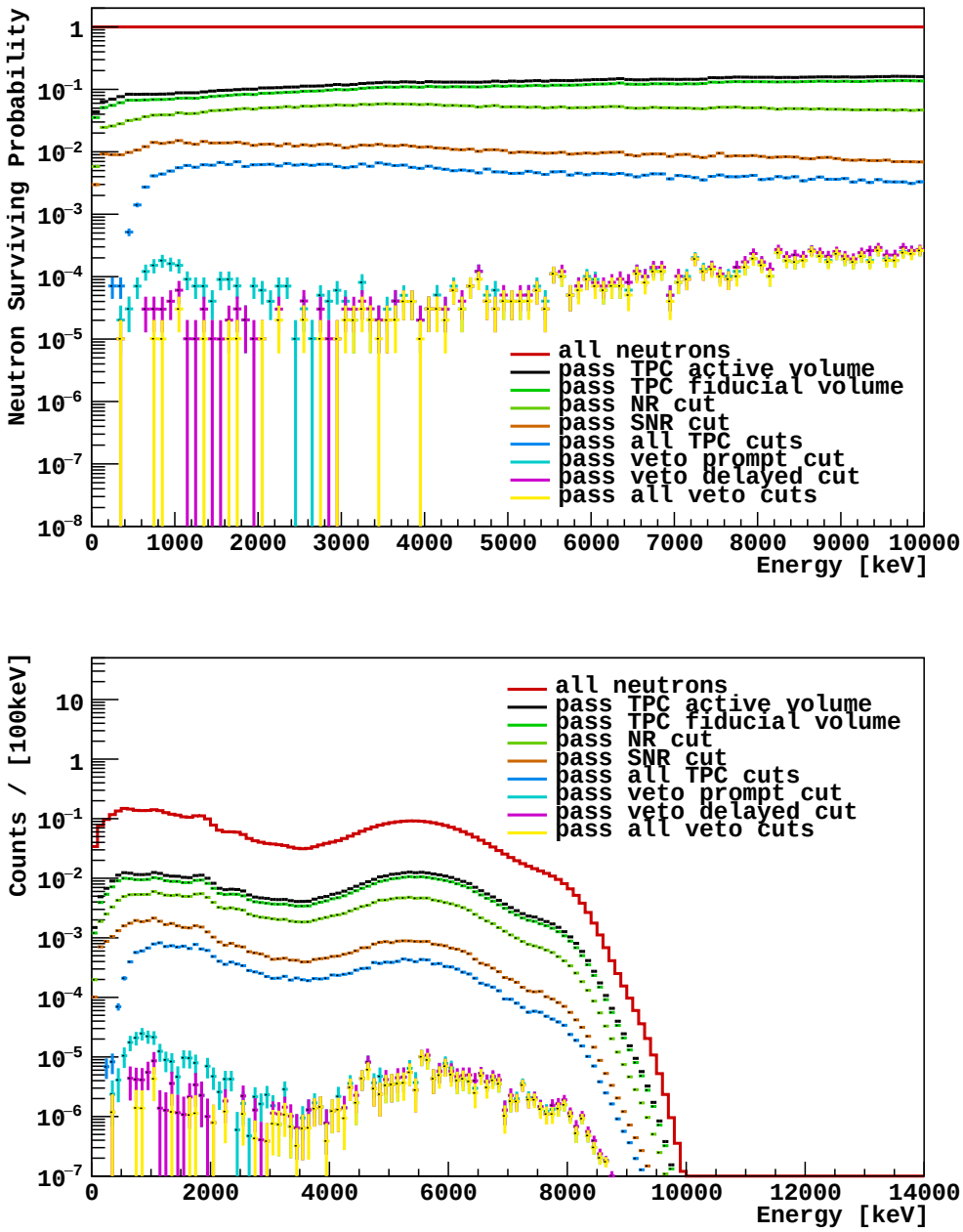

Figure 4.36: Neutrons from multilayer insulator. The cut is applied accumulatively. See text for the interpretation and discussion. Top: Probability of neutron passing the TPC and NV cuts. Bottom: Expected number of neutrons in one year passing the TPC and NV cuts.

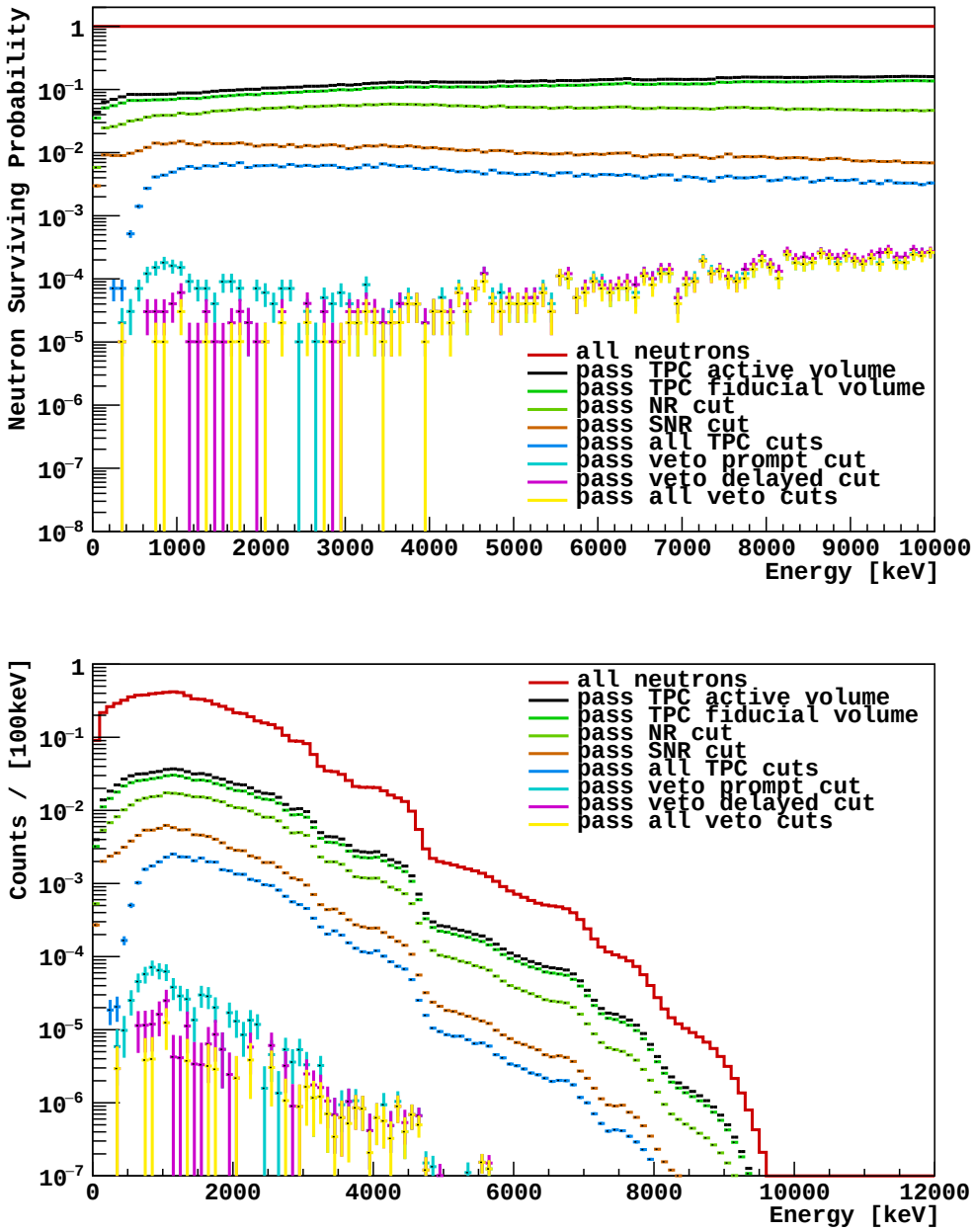

Figure 4.37: Neutrons from cryostat walls. The cut is applied accumulatively. See text for the interpretation and discussion. Top: Probability of neutron passing the TPC and NV cuts. Bottom: Expected number of neutrons in one year passing the TPC and NV cuts.

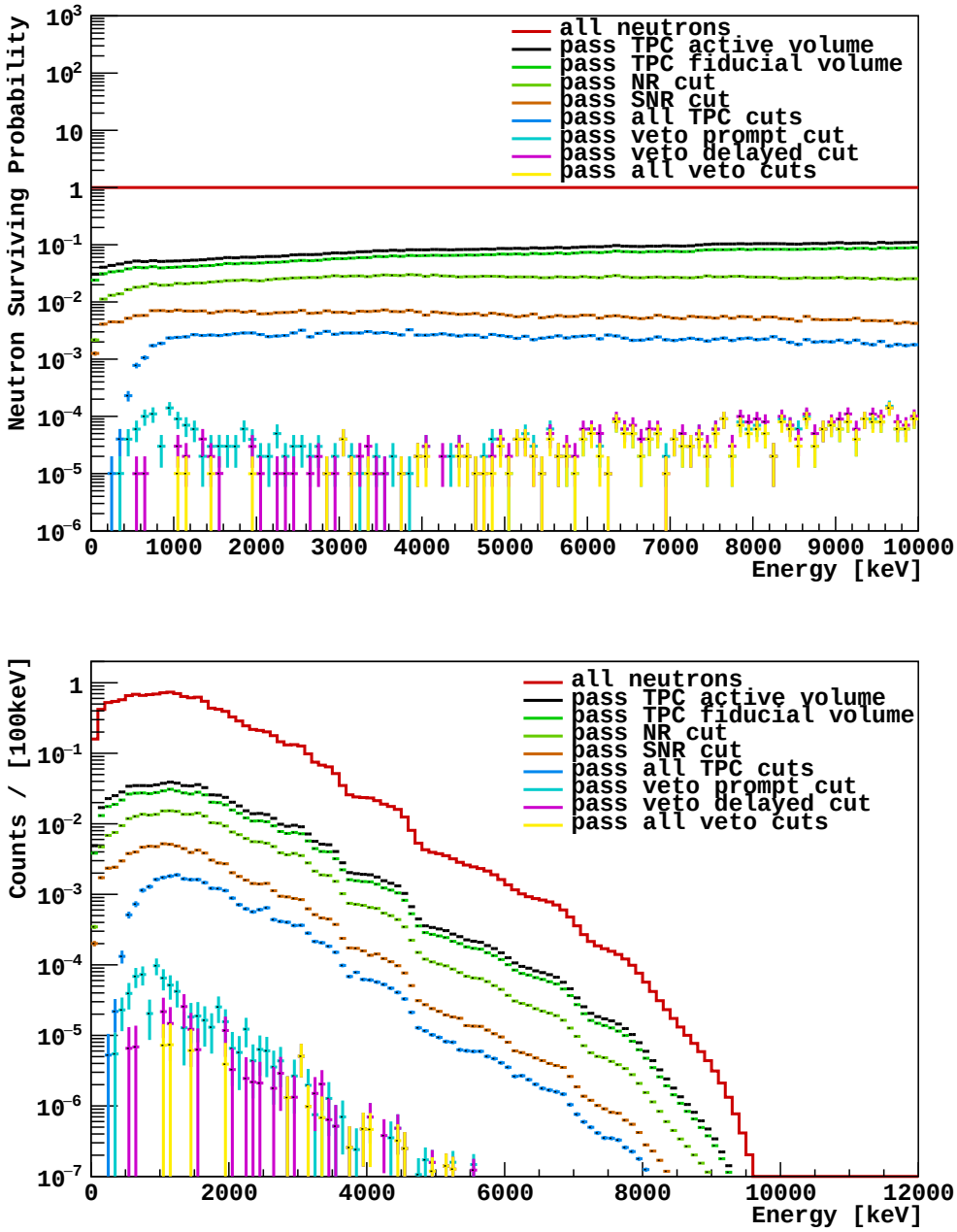

Figure 4.38: Neutrons from inner flange. The cut is applied accumulatively. See text for the interpretation and discussion. Top: Probability of neutron passing the TPC and NV cuts. Bottom: Expected number of neutrons in one year passing the TPC and NV cuts.

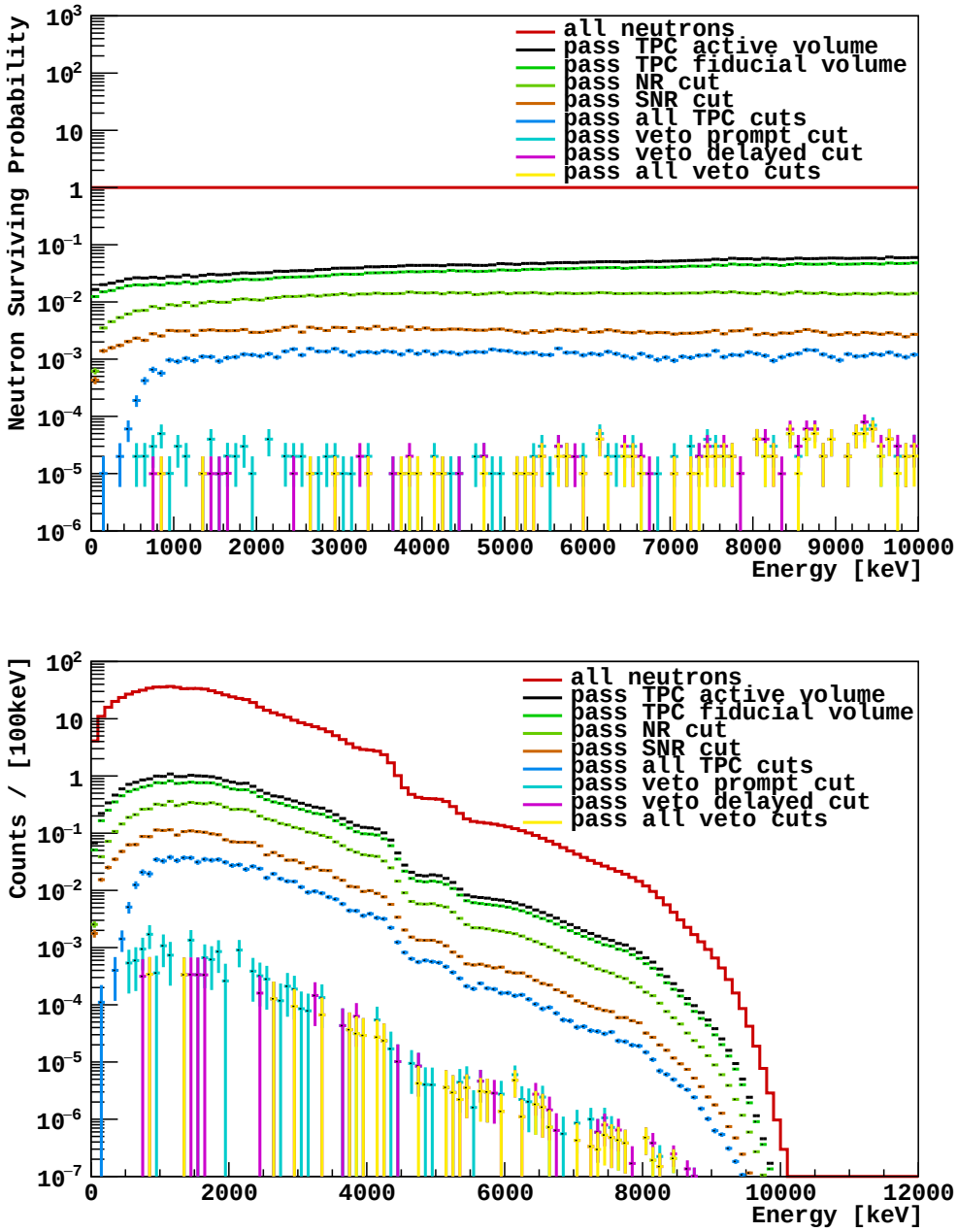

Figure 4.39: Neutrons from outer flange. The cut is applied accumulatively. See text for the interpretation and discussion. Top: Probability of neutron passing the TPC and NV cuts. Bottom: Expected number of neutrons in one year passing the TPC and NV cuts.

that neutron lost during the thermalization process in the prompt window depends on the neutron energy. The more energetic neutron deposits more energy in the prompt window of the NV. With a fixed threshold in the prompt cut, the neutron with lower energy is more likely to survive the prompt cut so that the rejection power decreases. As the neutron energy increases above ~3 MeV, the rejection power keeps decreasing. Similarly, the pattern, less obvious, is also seen in the veto delayed cut. The probability of neutron surviving the veto delayed cut is slightly smaller than that in the veto prompt cut.

The number of expected radiogenic neutron background is the multiplication of the neutron rate with the neutron surviving probability. In order to simplify the computation, the histograms of the neutron surviving probability and the neutron rate are binned with a width of 100 keV. The expected number of neutrons after certain cuts is N:

$$N = \sum_{i}^{\text{Mat}} \sum_{j}^{\text{Ene}} R(X_i, E_j) \times \Phi(X_i, E_j), \tag{4.13}$$

where $R(X_i, E_j)$ is the neutron rate and $\Phi(X_i, E_j)$ is the neutron surviving probability for neutron generated from material (such as PMT stem) X_i with energy E_j. The neutron energy is larger than 10 MeV at some materials, for instance PMT hardware and stem. For instance, the ^{9}Be(α,n)^{12}C reaction as Be-Cu alloy in the PMT hardware produces higher energy neutrons. In this study, however, the neutron with energy larger than 10 MeV shares the surviving probability with the neutron of 10 MeV since the distribution of the neutron surviving probability is relatively flat and the neutron rate is very small at higher energy.

In Figure 4.33, the plot at the bottom is the expected neutron events surviving certain cuts. The dominant radiogenic neutron background comes from PMT ceramic. The radiogenic neutron from PMT stem is slightly less than that from PMT ceramic. In PMT stem, there is a high level of the upper ^{238}U decay chain present in borosilicate glass and a relatively high (α,n) yield of the boron. The third dominant neutron

background source is the outer flange since the fluorine in the Viton o-ring has a high (α,n) yield and the o-ring itself is a high activity α generator. However, neutrons generated from this material is highly suppressed since the distance from outer flange to the TPC is relatively large. The PMT hardware is another leading neutron source following the outer flange. Even if the neutron rate from PMT hardware is small, the position close to the TPC increases the chance for neutrons to leave signals. The rest materials like cryostat walls, MLI, and inner flange are relatively clean so that the radiogenic neutrons generated from those materials are unlikely to pose a significant background threat to the experiment. Although the veto preprompt cut is not powerful to reject the WIMP-like neutrons, the veto prompt cut along with the veto delayed cut are capable of highly suppressing the radiogenic neutron background to a low level, as shown in Table 4.8. Overall, there are $\sim$13 radiogenic neutrons in the WIMP search region after all TPC cuts. With all the veto cuts, the expected radiogenic neutron background in one year is 0.04.

4.3.4 Neutron Veto Efficiency

Since the NV of DarkSide-50 is designed to reject the neutrons from different materials, the efficiency of each veto cut is one of the most interesting parameters that demonstrates the capability of the NV. In particular, the expected radiogenic neutron backgrounds and the veto prompt, delayed and total efficiency are the main goals in my study. To calculate those values, some notations are defined as:

T: neutrons pass all TPC cuts

P: neutrons pass all TPC and veto prompt cuts

D: neutrons pass all TPC and veto delayed cuts

A: neutrons pass all TPC and veto cuts

Table 4.8: Expected number of radiogenic neutrons in one year in DarkSide-50. The radiogenic neutrons are simulated from different materials of the detector. The number for each veto cut is based on the radiogenic neutrons surviving all TPC cuts. The number in the columns of the veto preprompt, prompt, and delayed cut is calculated individually from the radiogenic neutrons surviving all TPC cuts. "All Cuts" includes all TPC cuts and three veto cuts. The "Total" row is the sum of numbers in the column.

Material	**All**	**All TPC Cuts**	**Pre-Prompt Cut**	**Prompt Cut**	**Delayed Cut**	**All Cuts**
PMT Stem	503.021	4.91 ± 0.02	4.018 ± 0.003	0.069 ± 0.002	0.028 ± 0.001	0.019 ± 0.001
PMT Cerami	444.754	6.85 ± 0.03	5.603 ± 0.005	0.147 ± 0.004	0.035 ± 0.002	0.021 ± 0.001
PMT hardware	33.84	0.293 ± 0.001	0.2370 ± 0.0002	$(6.1 \pm 0.1) \times 10^{-3}$	$(3.4 \pm 0.1) \times 10^{-3}$	$(2.75 \pm 0.09) \times 10^{-3}$
Cryostat Walls	8.48	$(3.99 \pm 0.03) \times 10^{-2}$	$(3.48 \pm 0.06) \times 10^{-2}$	$(6.0 \pm 0.4) \times 10^{-4}$	$(1.6 \pm 0.2) \times 10^{-4}$	$(5 \pm 1) \times 10^{-5}$
MLI	5.34	0.0249 ± 0.0001	0.0183 ± 0.0002	$(3.8 \pm 0.1) \times 10^{-4}$	$(2.2 \pm 0.1) \times 10^{-4}$	$(1.6 \pm 0.1) \times 10^{-4}$
Inner Flange	14.27	0.0286 ± 0.0003	0.0198 ± 0.0009	$(6.7 \pm 0.6) \times 10^{-4}$	$(1.4 \pm 0.2) \times 10^{-4}$	$(3 \pm 1) \times 10^{-5}$
Outer Flange	794.15	0.74 ± 0.01	0.493 ± 0.002	0.014 ± 0.002	$(2.9 \pm 0.8) \times 10^{-3}$	$(1.1 \pm 0.5) \times 10^{-3}$
Total	1803.855	12.89 ± 0.04	10.424 ± 0.007	0.238 ± 0.005	0.069 ± 0.003	0.044 ± 0.002

In general, label k represents different cuts ($k \in \{T, P, D, A\}$). The total number of neutrons generated from material (X_i) with energy E_j is $W(X_i, E_j)$ and the number of neutrons surviving cut k is $W_k(X_i, E_j)$. According to the convention, the neutron surviving probability becomes:

$$\Phi_k(X_i, E_j) = \frac{W_k(X_i, E_j)}{W(X_i, E_j)}, \tag{4.14}$$

The expected number of the neutrons surviving cut k (N_k) is:

$$N_k = \sum_i^{\text{Mat}} \sum_j^{\text{Ene}} R(X_i, E_j) \times \Phi_k(X_i, E_j) = \sum_i^{\text{Mat}} \sum_j^{\text{Ene}} R(X_i, E_j) \times \frac{W_k(X_i, E_j)}{W(X_i, E_j)}, \tag{4.15}$$

The uncertainty of $\Phi_k(X_i, E_j)$ and N_k can be propagated as:

$$\delta\Phi_k(X_i, E_j) = \frac{\sqrt{W_k(X_i, E_j) \cdot \left(1 - \frac{W_k(X_i, E_j)}{W(X_i, E_j)}\right)}}{W(X_i, E_j)}, \tag{4.16}$$

$$\delta N_k = \sqrt{\sum_i^{\text{Mat}} \sum_j^{\text{Ene}} (R(X_i, E_j) \cdot \delta\Phi_k(X_i, E_j))^2}, \tag{4.17}$$

Since $W(X_i, E_j)$ is the total number of neutrons generated from material X_i with energy E_j, each neutron event follows a Bernoulli distribution to pass certain cut. Then $W_k(X_i, E_j)$ and $W(X_i, E_j)$ becomes:

$$W_k(X_i, E_j) = \sum_h^W F_k^h(X_i, E_j), \tag{4.18}$$

Hereby, $F_k^h(X_i, E_j)$ is a random variable that follows Bernoulli distribution and h is the index of neutron event. Therefore, $W_k(X_i, E_j)$ follows a Binomal distribution with total trials of $W(X_i, E_j)$ and a probability to pass each trial of $\Phi_k(X_i, E_j)$ as the unbiased estimator of the Bernoulli distribution. The prompt veto efficiency (ϵ_P), the probability of neutron that survives all TPC cuts but fails the veto prompt cut,

is derived as the ratio of:

$$\epsilon_P = \frac{N_{\bar{P}}}{N_T} = 1 - \frac{N_P}{N_T}, \tag{4.19}$$

Here $N_{\bar{P}}$, the number of neutrons rejected by the veto prompt cut, is the difference between N_T and N_P. The prompt veto efficiency (ϵ_P) demonstrates the capability of the NV to veto the neutron events by only selecting events that have prompt coincidence, which are mostly from the neutron thermalization and γ-rays from neutron inelastic scatterings.

The uncertainty of ϵ_P from MC is propagated as:

$$\begin{aligned}(\delta\epsilon_P)^2 = \sum_i^{\text{Mat}} \sum_j^{\text{Ene}} \Big(\Big(\frac{R(X_i, E_j) \cdot \delta\Phi_P(X_i, E_j)}{N_T} \Big)^2 + \Big(\frac{N_P \cdot R(X_i, E_j) \cdot \delta\Phi_T(X_i, E_j)}{N_T^2} \Big)^2 \\ - 2 \cdot \frac{N_P \cdot R^2(X_i, E_j)}{N_T^3} \cdot \text{cov}(\Phi_P(X_i, E_j), \Phi_T(X_i, E_j)) \Big),\end{aligned} \tag{4.20}$$

The uncertainty of $\Phi_P(X_i, E_j)$ and $\Phi_T(X_i, E_j)$ are calculated as Equation 4.16. The difficult part is to get the covariance between these two variables. As explained in Equation 4.18, both $F_T(X_i, E_j)$ and $F_P(X_i, E_j)$ follow Bernoulli distribution but with different probabilities, it is also easy to prove that there is a Binomial distribution between $F_T(X_i, E_j)$ and $F_P(X_i, E_j)$ that is $F_P(X_i, E_j) \sim \text{B}(F_T(X_i, E_j),\ q(X_i, E_j))$. Here $q(X_i, E_j)$ is:

$$q(X_i, E_j) = \frac{\Phi_P(X_i, E_j)}{\Phi_T(X_i, E_j)}, \tag{4.21}$$

The covariance between $F_T(X_i, E_j)$ and $F_P(X_i, E_j)$ can be calculated as:

$$\begin{aligned}
\mathrm{cov}(F_P, F_T) &= E[(F_P - E(F_P))][(F_T - E(F_T))] = E[F_P F_T] - E[F_P] \cdot E[F_T] \\
&= E[E[F_T F_P | F_T]] - \Phi_P \cdot \Phi_T = E[F_T \cdot E[F_P | F_T]] - \Phi_P \cdot \Phi_T \\
&= E[F_T \cdot F_T \cdot q] - \Phi_P \cdot \Phi_T = q \cdot E[F_T \cdot F_T] - \Phi_P \cdot \Phi_T \\
&= q \cdot (\sigma^2(F_T) + E^2[F_T]) - \Phi_P \cdot \Phi_T \\
&= q \cdot \Phi_T - \Phi_P \cdot \Phi_T \\
&= \Phi_p \cdot (1 - \Phi_T),
\end{aligned} \tag{4.22}$$

where the label of (X_i, E_j) is ingored just to simplify the notation. Since $W(X_i, E_j)$ is just a fixed number as total number of neutrons generated in MC and the covariance only exists in the same event, so:

$$\begin{aligned}
\mathrm{cov}(\Phi_P, \Phi_T) &= \mathrm{cov}\Big(\frac{W_P}{W}, \frac{W_T}{W}\Big) = \frac{1}{W^2} \cdot \mathrm{cov}(W_P, W_T) \\
&= \frac{1}{W^2} \cdot \mathrm{cov}\Big(\sum_h^W F_P^h, \sum_l^W F_T^l\Big) = \frac{1}{W^2} \cdot \sum_h^W \mathrm{cov}(F_P^h, F_T^h) \\
&= \frac{\Phi_p \cdot (1 - \Phi_T)}{W},
\end{aligned} \tag{4.23}$$

Then the covariance between $\Phi_P(X_i, E_j)$ and $\Phi_T(X_i, E_j)$ can be inserted back into the equation 4.20 in order to propagate the uncertainty of the prompt veto efficiency. In Table 4.8, N_T and N_P are computed by summing the neutrons generated from different materials. N_T is 12.889 and N_P is 0.238. Then the prompt veto efficiency ϵ_P is $98.15 \pm 0.04\,\%$.

Similarly, the delayed veto efficiency can be derived as the ratio of total neutrons passing all TPC cuts but failing the veto delayed cut ($N_{\bar{D}}$) to the neutrons passing all the TPC cuts (N_T). $N_{\bar{D}}$ is 12.820 as the difference between N_T (12.889) and N_D (0.069). Then the delayed veto efficiency (ϵ_D) is $99.46 \pm 0.02\,\%$. The veto delayed

cut is designed to reject the neutrons by targeting the neutron capture signals mainly from ^{10}B, ^{12}C, and ^{1}H.

Last but not least, there are ∼13 radiogenic neutrons, as listed in Table 4.8, expected in the WIMP search region (as used in Ref. [37]) per year. With all the veto cuts, the total radiogenic neutron background in one year (N_A) listed in Table 4.8 is 0.044 ± 0.002. Then the total veto efficiency of the NV is projected to be $99.66 \pm 0.01\,\%$.

Table 4.9: Summary of neutron veto efficiency based on radiogenic neutron in MC.

prompt veto efficiency	**delayed veto efficiency**	**total veto efficiency**
$98.15 \pm 0.04\,\%$	$99.46 \pm 0.02\,\%$	$99.66 \pm 0.01\,\%$

Recently, the DarkSide-50 collaboration published a new paper with 532 live-days UAr data. In DarkSide-50 UAr data, the events that fail the veto prompt cut are taken as the "Veto Prompt Tag" (VPT) sample. In order to calculate the neutron events, it is necessary to apply the veto delayed cut that detects the neutron capture signals on the VPT sample. However, the veto delayed cut is modified in the analysis of UAr data. As described in Section 3.2, the prompt window overlaps with the delayed window in a small region. In the UAr data, there is a big fraction of after-pulses induced by γ-rays that reside in the delayed window from radioactive sources in the detector materials. The after-pulses disguise neutron capture signals. To suppress or avoid these effects, the modified veto delayed cut rejects event that occurs at least 200 ns after the prompt window with cluster charge larger than 100 PE. The efficiency of the modified veto delayed cut depends on the higher energy part of neutron capture signals on ^{10}B, while the lower energy part from α+^{7}Li peak is lost. With the modified veto delayed cut, the radiogenic neutron background is reported to be < 0.005 with a 100 % statistical error [34], which is smaller than the 0.044 ± 0.002 radiogenic neutron estimated by the G4DS MC.

This discrepancy is partly due to the different veto delayed cuts used in MC and UAr data analysis. To tackle the discrepancy, the simulation procedures are composed and cross-checked. First, the NeuCBOT only accounts for the neutrons generated from the radioactive sources while γ-rays that may correlate with the neutrons as products of the decays are not included in the calculation [68]. As γ-rays scatter in the TPC, they are rejected by the PSD and so are the correlated neutron events, which decrease the neutron surviving probability. A rough simulation suggests that the expected radiogenic neutron background could drop by up to $\sim$40 % if γ-rays are considered. Second, the (α, n) yield in the NeuCBOT is reported to be $\sim$30 % higher than the results from other tools [68]. The higher (α, n) yield increases the radiogenic neutron rate, which is base value for the calculation of expected radiogenic neutron background. Third, the TPC cuts in G4DS MC are the simplified models of the cuts used in UAr data analysis. For instance, the S1 and time information are not calculated by performing an optical simulation due to limited computation resources. There are still discrepancies on neutron captures signals and time distribution between MC and data. In addition to the reasons discussed above, there might be other sources of the discrepancy. It is important to devise a program to fully resolve this discrepancy, in order to reach the best prediction of background for future detectors of the DarkSide family.

Chapter 5

Conclusions

Theoretical physicists have proposed several models and candidates for dark matter. One of the most promising dark matter candidate is the WIMP, which has extremely low interaction cross section. In order to detect dark matter, experiments must reduce background while maintaining sensitivity to a potential dark matter signal. There are four primary sources of background: γ-rays, Cherenkov radiation, β's from ^{39}Ar and neutrons. The powerful PSD and f_{90} model are proven to distinguish the electron recoils from nuclear recoils, which makes argon a promising target to explore the signals from dark matter particles. Selection of the materials in the detector along with the high efficiency of the LSV can highly reduce the background which may pose a risk for the WIMP search region.

The UAr WIMP search data in DarkSide-50 are dominated by γ-rays generated by radioactive isotopes. The source activity measured by material counting and spectrum fits are helpful for us to validate the background model. Since some of the γ-rays with high energy can travel through both the TPC and outer detectors, they provide a method to calibrate the detectors. By periodically checking the important variables in the data set, it is possible to monitor the performance and stability of the detector. In order to separate background events from WIMP signals, some event

selection criteria were developed and tuned so that the acceptance loss and efficiency of the veto cuts are optimized.

Besides γ-rays, the neutron background is particularly important since it leaves nuclear recoils signals in the TPC indistinguishable for WIMPs. It is important to measure the response of the detector to nuclear recoils events. The boron-loaded organic scintillator in the LSV can detect both the neutron thermalization signals in the prompt window and the neutron capture signals in the delayed window. In order to quantify the performance of the detector, multiple neutron calibration sources were deployed in the LSV.

With a ^{241}Am^{9}Be neutron source, the neutron capture signals in the veto, on ^{10}B in particular, were measured. The dominant peak at (246.70 ± 0.16) PE with $0.7\,\mathrm{g\,L^{-1}}$ is the 478 keV γ-ray as a product of neutron capture on ^{10}B, which has a neutron capture cross section of 3836 b. The lower peak at (23.08 ± 0.09) PE is from highly quenched α and ^{7}Li particles. The neutron capture time is calculated to be (21.68 ± 0.66) µs by fitting an exponential function to the time distribution. The neutron source shows that 8% of the 478 keV γ-rays are lost and leave the veto with no neutron capture signal detected, which increases the ratio of the higher energy peak to the lower one from the 6.4% model prediction to 10.5% in practice.

One interesting phenomenon from the ^{241}Am^{9}Be neutron calibration is the effect on α-only and $\alpha + \gamma +$ ^{7}Li peak due to the addition of more PPO to the liquid scintillator. The former peak increases by $\sim$11% while the latter decreases by $\sim$5%. The increment of the α-only peak helps improve the neutron veto efficiency since more neutron capture events can reach beyond the event selection threshold.

However, the ^{241}Am^{9}Be source has a large fraction of coincident γ-rays emitted along with the neutrons, which makes it hard to select clean neutron thermalization signals in the prompt window. In order to reduce these γ-rays, a different neutron source, ^{241}Am^{13}C, was designed to get the neutron veto efficiency from the prompt

window in the LSV. Based on that data, the neutron veto efficiency of prompt is determined to be 98.92%±0.14%(stat)±0.04%(sys) after MC correction.

With the MC tuning based on ^{241}Am^{13}C data, a further study of the radiogenic neutron background was conducted to determine the annual neutron background and total neutron veto efficiency. With the radiogenic neutrons simulated at different positions of the detector with non-negligible source activity, the expected radiogenic neutron background is 0.044 ± 0.002 in one year. The total neutron veto efficiency is projected to be 99.66%±0.01%.

The background calculated via G4DS MC, 0.044 ± 0.002 in one year, is significantly larger than what extrapolated from data, < 0.005 in one year. The difference is due to the different veto delayed cuts used in G4DS MC and data analysis, the lack of γ-rays simulated in the NeuCBOT, the high (α, n) yield in the NeuCBOT, and the simplified TPC cuts implemented in the G4DS MC. It is important to develop a program to fully understand and resolve the discrepancy, which will help with the prediction of the radiogenic neutron background for future detectors of the DarkSide family.

Bibliography

[1] Baudis, L. WIMP dark matter direct-detection searches in noble gases. *Phys. of the Dark Universe* **4**, 50 – 59 (2014). DARK TAUP2013.

[2] Rees, M. J. Dark matter: Introduction. *Phil. Trans. Roy. Soc. Lond. A* **361**, 2427–2434 (2003).

[3] Begeman, K. G., Broeils, A. H., and Sanders, R. H. Extended rotation curves of spiral galaxies - Dark haloes and modified dynamics. *Mon. Not. of the Roy. Astron. Soc.* **249**, 523–537, Apr (1991).

[4] Weijmans, A. M. and Krajnovi, D. The shape of the dark matter halo in the early-type galaxy NGC 2974. *Mon. Not. of the Roy. Astron. Soc.* **383**(4), 1343–1358 (2008).

[5] Massey, R., Kitching, T., and Richard, J. The dark matter of gravitational lensing. *Rept. Prog. Phys.* **73**, 086901 (2010).

[6] Brownstein, J. R. and Moffat, J. W. The Bullet Cluster 1E0657-558 evidence shows Modified Gravity in the absence of Dark Matter. *Mon. Not. of the Roy. Astron. Soc.* **382**, 29–47 (2007).

[7] Penzias, A. and Wilson, R. A Measurement of Excess Antenna Temperature at 4080 Mc/s. *Astrophys. Phys. J.* **142**, 419–421, Jul (1965).

[8] Clements, D. L. An Introduction to the Planck Mission. *Contemp. Phys.* **58**(4), 331–348 (2017).

[9] Ade, P. et al. Planck 2013 results. I. Overview of products and scientific results. *Astron. Astrophys.* **571**, A1 (2014).

[10] Spergel, D. N. et al. First year Wilkinson Microwave Anisotropy Probe (WMAP) observations: Determination of cosmological parameters. *Astrophys. J. Suppl.* **148**, 175–194 (2003).

[11] Hinshaw, G. et al. Nine-year Wilkinson Microwave Anisotropy Probe (WMAP) Observations: Cosmological Parameter Results. *Astrophys. J.* **208**, 19, Oct (2013).

[12] Muoz, J. B. et al. Heating of Baryons due to Scattering with Dark Matter During the Dark Ages. *Phys. Rev. D* **92**(8), 083528 (2015).

[13] Goetz, M. and Sommer-Larsen, J. Galaxy formation: warm dark matter, missing satellites, and the angular momentum problem. *Astrophys. Space Sci.* **284**, 341–344 (2003).

[14] Drukier, A. K., Freese, K., and Spergel, D. N. Detecting cold dark-matter candidates. *Phys. Rev. D* **33**, 3495–3508, Jun (1986).

[15] Bilal, A. Introduction to supersymmetry. (2001).

[16] Peccei, R. D. and Quinn, H. R. CP Conservation in the Presence of Pseudoparticles. *Phys. Rev. Lett.* **38**, 1440–1443, Jun (1977).

[17] Olive, K. and Group, P. D. Review of Particle Physics. *Chinese Physics C* **38**(9), 090001 (2014).

[18] Vafa, C. and Witten, E. Parity Conservation in Quantum Chromodynamics. *Phys. Rev. Lett.* **53**, 535–536, Aug (1984).

[19] Green, A. M. Astrophysical uncertainties on direct detection experiments. *Mod. Phys. Lett. A* **27**, 1230004 (2012).

[20] Drewes, M. et al. A White Paper on keV Sterile Neutrino Dark Matter. *JCAP* **1701**(01), 025 (2017).

[21] Dobrescu, B. A. and Mocioiu, I. Spin-dependent macroscopic forces from new particle exchange. *JHEP* **11**, 005 (2006).

[22] Cooper, F., Khare, A., and Sukhatme, U. Supersymmetry and quantum mechanics. *Phys. Rept.* **251**, 267–385 (1995).

[23] Cheng, T. et al. Supersymmetry with a Heavy Lightest Supersymmetric Particle. *J. Phys. G* **42**(6), 065004 (2015).

[24] Steigman, G., Dasgupta, B., and Beacom, J. F. Precise relic WIMP abundance and its impact on searches for dark matter annihilation. *Phys. Rev. D* **86**, 023506, Jul (2012).

[25] Steigman, G. CMB Constraints On The Thermal WIMP Mass And Annihilation Cross Section. *Phys. Rev. D* **91**(8), 083538 (2015).

[26] Cerdeno, D. G. and Green, A. M. Direct detection of WIMPs. *arXiv* , 347–369 (2010).

[27] Marrodn Undagoitia, T. and Rauch, L. Dark matter direct-detection experiments. *J. Phys. G* **43**(1), 013001 (2016).

[28] Xu, J. *Study of Argon from Underground Sources for Direct Dark Matter Detection.* PhD thesis, Princeton University, (2013).

[29] Albert, J. B. et al. Improved measurement of the $2\nu\beta\beta$ half-life of ^{136}Xe with the EXO-200 detector. *Phys. Rev. C* **89**, 015502, Jan (2014).

[30] Agnes, P. et al. Results from the first use of low radioactivity argon in a dark matter search. *Phys. Rev. D* **93**(8), 081101 (2016).

[31] Aprile, E. et al. Physics reach of the XENON1T dark matter experiment. *JCAP* **1604**(04), 027 (2016).

[32] Akerib, D. S. et al. Results from a search for dark matter in the complete LUX exposure. *Phys. Rev. Lett.* **118**(2), 021303 (2017).

[33] Aprile, E. et al. First Dark Matter Search Results from the XENON1T Experiment. *Phys. Rev. Lett.* **119**(18), 181301 (2017).

[34] Agnes, P. et al. DarkSide-50 532-day Dark Matter Search with Low-Radioactivity Argon. (2018).

[35] Amaudruz, P. A. et al. Design and Construction of the DEAP-3600 Dark Matter Detector. *Astropart. Phys.* (2017).

[36] Amaudruz, P. A. et al. First results from the DEAP-3600 dark matter search with argon at SNOLAB. (2017).

[37] Agnes, P. et al. First Results from the DarkSide-50 Dark Matter Experiment at Laboratori Nazionali del Gran Sasso. *Phys. Lett. B* **743**, 456–466 (2015).

[38] Kubota, S., Hishida, M., and Raun, J. Evidence for a triplet state of the self-trapped exciton states in liquid argon, krypton and xenon. *J. of Phys. C: Solid State Physics* **11**(12), 2645 (1978).

[39] Gastler, D. et al. Measurement of scintillation efficiency for nuclear recoils in liquid argon. *Phys. Rev. C* **85**, 065811, Jun (2012).

[40] Lippincott, W. H. et al. Scintillation time dependence and pulse shape discrimination in liquid argon. *Phys. Rev. C* **78**, 035801, Sep (2008).

[41] Li, Y. et al. Measurement of Longitudinal Electron Diffusion in Liquid Argon. *Nucl. Instrum. Meth. A* **816**, 160–170 (2016).

[42] Alexander, T. et al. Observation of the dependence on drift field of scintillation from nuclear recoils in liquid argon. *Phys. Rev. D* **88**, 092006, Nov (2013).

[43] Cao, H. et al. Measurement of scintillation and ionization yield and scintillation pulse shape from nuclear recoils in liquid argon. *Phys. Rev. D* **91**, 092007, May (2015).

[44] Benetti, P. et al. Measurement of the specific activity of ar-39 in natural argon. *Nucl. Instrum. Meth. A* **574**, 83–88 (2007).

[45] Hong, J., Craig, W. W., Graham, P., Hailey, C. J., et al. The scintillation efficiency of carbon and hydrogen recoils in an organic liquid scintillator for dark matter searches. *Astrophys. J.* **16**, 333–338, Jan (2002).

[46] Andronic, A. et al. Drift velocity and gain in argon- and xenon-based mixtures. *Nucl. Instrum. Meth.* **523**, 302–308, May (2004).

[47] Westerdale, S. S. *A Study of Nuclear Recoil Backgrounds in Dark Matter Detectors.* PhD thesis, Princeton University, (2016).

[48] Wright, A., Mosteiro, P., Loer, B., and Calaprice, F. A Highly Efficient Neutron Veto for Dark Matter Experiments. *Nucl. Instrum. Meth. A* **644**, 18–26 (2011).

[49] Alimonti, G. et al. Measurement of the ^{14}C abundance in a low-background liquid scintillator. *Phys. Lett. B* **422**, 349–358, Mar (1998).

[50] Salas Redondo, C. et al. Interplay of Fluorescence and Phosphorescence in Organic Biluminescent Emitters. *arXiv* , Apr (2017).

[51] Agnes., P. et al. The veto system of the DarkSide-50 experiment. *J. of Instrum.* **11**(03), P03016 (2016).

[52] Birks, J. The Theory and Practice of Scintillation Counting. *Pergamon* , 3 (1964).

[53] Swiderski, L. and Moszynski, M. Further Study of Boron-10 Loaded Liquid Scintillators for Detection of Fast and Thermal Neutrons. *IEEE Transactions on Nuclear Science* **57**, 375–380, Feb (2010).

[54] Schreck, M. Vacuum Cherenkov radiation for Lorentz-violating fermions. *Phys. Rev. D* **96**(9), 095026 (2017).

[55] Afanasiev, G. N., Kartavenko, V. G., and Stepanovsky, Yu. P. On Tamm's problem in the Vavilov-Cerenkov radiation theory. *J. Phys. D* **32**, 2029 (1999).

[56] Green, C., Kowalkowski, J., Paterno, M., Fischler, M., Garren, L., and Lu, Q. The art framework. *J. Phys. Conf. Ser.* **396**(2), 022020 (2012).

[57] Hubbell, J. and Seltzer, S. Cross section data for electronpositron pair production by photons: a status report. *Nucl. Instrum. Meth.* **213**, 1 – 9 (2004).

[58] Baurov, Y. et al. Experimental investigations of changes in beta decay rate of Co-60 and Cs-137. *Mod. Phys. Lett. A* **16**, 2089–2102 (2001).

[59] Rupak, G., Fernando, L., and Vaghani, A. Radiative Neutron Capture on Carbon-14 in Effective Field Theory. *Phys. Rev. C* **86**, 044608 (2012).

[60] Fry, C. and Thoennessen, M. Discovery of Isotopes of the Transuranium Elements with 93 < Z < 98. *Atom. Data Nucl. Data Tabl.* **99**, 96–114 (2013).

[61] Vijaya, A. and Kumar, A. The neutron spectrum of AmBe neutron sources. *Nucl. Instrum. Meth.* **111**(3), 435 – 440 (1973).

[62] Akerib, D. S. et al. Low-energy (0.7-74 keV) nuclear recoil calibration of the LUX dark matter experiment using D-D neutron scattering kinematics. (2016).

[63] Liu, J. et al. Neutron Calibration Sources in the Daya Bay Experiment. *Nucl. Instrum. Meth. A* **797**, 260–264 (2015).

[64] Lindhard, J., Nielsen, V., Scharff, M., and Thomsen, P. Integral Equations Governing Radiation Effects. *Kgl. Danske Videnskab., Selskab. Mat. Fys. Medd.* **33**(1) (1963).

[65] Agnes, P. et al. Simulation of argon response and light detection in the DarkSide-50 dual phase TPC. *J. of Instrum.* **12**(10), P10015 (2017).

[66] Doke, T., Crawford, H. J., Hitachi, A., Kikuchi, J., Lindstrom, P. J., Masuda, K., Shibamura, E., and Takahashi, T. Let dependence of scintillation yields in liquid argon. *Nucl. Instrum. Meth.* **269**(1), 291 – 296 (1988).

[67] Craun, R. L. and Smith, D. L. Analysis of response data for several organic scintillators. *Nucl. Instrum. Meth.* **80**, 239–244 (1970).

[68] Westerdale, S. and Meyers, P. D. Radiogenic Neutron Yield Calculations for Low-Background Experiments. *Nucl. Instrum. Meth. A* **875**, 57–64 (2017).

[69] Koning, A. et al. Talys-1.6. *Nuclear Reaction Program* (2013).

[70] Shibata, K. et al. Japanese evaluated nuclear data library. *J. of Nuc. Science and Technology* **39, 1125** (2002).

[71] Chardwick, M. et al. ENDF/B-VII.1 Nuclear Data for Science and Technology: Cross Sections, Covariances, Fission Product Yields and Decay Data. *Nucl. Data Sheets, 112, 2887* (2011).

[72] Guangyong, K. *A dark matter search with DarkSide-50.* PhD thesis, Princeton University, (2018).

[73] Agnes, P. et al. Direct Search for Dark Matter with DarkSide. *J. Phys. Conf. Ser.* **650**(1), 012006 (2015).